

Ph.D. Dissertation

Study of the Effects of Dust in the Martian
Meteorology Using a General Circulation Model

Applied for Ph.D. (Science) in June 2006

Department of Earth and Planetary Science,
University of Tokyo

Takeshi Kuroda

Abstract

The work presents the investigations of radiative and dynamical processes of the Martian atmosphere using a General Circulation Model (GCM). The model is based on the CCSR/NIES terrestrial AGCM, and was converted by including physical processes specific for the Martian atmosphere. In particular, the radiative effects of dust are important in determining the atmospheric temperature fields. A series of numerical experiments was performed to study the sensitivity of the simulated temperature to the variations of the dust parameters (particle size distribution, refractive indices). While this sensitivity is small for the ‘weak-dust’ case (visible dust opacity ~ 0.2), it becomes significant during a planet-encircling dust storm (visible dust opacity ~ 2.2). The particle size distribution affects the vertical distribution of heating rates, and the refractive index affects the strength of heating rates. The resulting temperature fields influence the structure of baroclinic waves observed in autumn and winter in the northern midlatitudes. This prompted the investigation of the baroclinic waves during different seasons and for different dust opacities employing the Martian GCM. In the ‘weak-dust’ case, qualitatively consistent seasonal changes of wave properties and atmospheric fields with the MGS-TES observations are reproduced in the model. A very strong wave with ~ 6.6 Sols period and the zonal wavenumber 1 occurs in the winter, while a wave with ~ 3.1 Sols period and the wavenumber 2 is dominant in the autumn. Employing the linear instability analysis, this change can be qualitatively explained through changes in the vertical wind shear and atmospheric stability. In winter, the region with negative potential vorticity gradient at $\sim 70^\circ$ N becomes larger, indicating stronger baroclinic wave generation. This also shows that the distribution of the zonal mean wind and temperature in winter subdue the northward wave propagation. A planet-encircling dust storm causes a significant reduction of the baroclinic wave activity in winter. It is demonstrated that the wave amplitude decreases, and the wavenumbers of the dominant harmonics increase to 2-4 during strong-dust winters in the model, which is consistent with the Viking Lander 2 observations. This occurs due to the significant decrease of the vertical wind shear near the surface, which apparently is due to the very strong north polar warming caused by dynamical effects. The waves with larger zonal wavenumbers, especially with

those greater than 3, are less likely to propagate upward. Therefore, the baroclinic waves practically disappear at altitudes higher than ~ 0.5 mb. During a strong-dust autumn, such reduction of the waves does not occur either in the model, or in the observations. This is due to the strong dust heating in the south of $\sim 40^\circ$ N that maintains the meridional temperature gradient in northern midlatitude. The mechanisms, which lead to the wave structures in the Martian atmosphere during different seasons and dust conditions, are analyzed in this work.

Contents

Chapter 1	Introduction	1
1.1	Main features of the Martian atmosphere.....	1
1.2	Evaluation of the properties and radiative effects of Martian dust.....	2
1.2.1	Importance of dust for the Martian meteorology.....	2
1.2.2	Particle size distribution.....	3
1.2.3	Refractive indices.....	3
1.2.4	Calculation of the radiative fluxes.....	4
1.2.5	Vertical distribution.....	5
1.3	Impact of the global dust storm on the atmospheric temperature.....	8
1.4	Baroclinic waves in the Martian atmosphere.....	8
1.5	Importance of this work.....	16
Chapter 2	Outline of the CCSR/NIES Martian GCM	18
2.1	Basic features.....	18
2.2	Dynamics.....	18
2.3	Surface parameters.....	21
2.4	CO ₂ condensation/sublimation processes.....	21
2.5	Radiation.....	22
2.5.1	CO ₂ gas.....	22
2.5.2	Dust.....	25
2.6	Atmospheric dust distribution.....	25

Chapter 3 Sensitivity of the model results to the radiative parameters 32

3.1 Basic features of the model results in the ‘weak-dust’ case.....32

3.1.1 Daytime temperature and heating/cooling effects.....32

3.1.2 Nighttime temperature and heating/cooling effects.....33

3.1.3 Sensitivity to the CO₂ infrared band.....34

3.2 Basic features of the model results in the ‘strong-dust’ case.....38

3.2.1 Daytime temperature and heating/cooling effects.....38

3.2.2 Nighttime temperature and heating/cooling effects.....38

3.2.3 Sensitivity to the CO₂ infrared band.....38

3.3 Sensitivity to the dust parameters.....42

3.3.1 Sensitivity to the particle size distribution.....42

3.3.2 Sensitivity to the refractive indices.....43

3.4 Summary and the accuracy of the simulated temperature for different dust opacities.....46

Chapter 4 Baroclinic waves in the Martian atmosphere for different seasons and dust conditions 54

4.1 Basic features of the simulated waves in ‘autumn’ for the ‘weak-dust’ scenario.....54

4.1.1 Comparison with the Viking Lander 2 observations.....54

4.1.2 Linear estimation of baroclinic growth rates.....55

4.1.3 Vertical structures.....56

4.2 Seasonal changes of the wave properties in the ‘weak-dust’ case.....60

4.2.1 Vertical structure of the waves in ‘winter’.....60

4.2.2 Seasonal change of the atmospheric fields.....62

4.2.3 Note: Surface temperature and EP-flux.....63

4.3 Changes of the wave properties due to the global dust storm....70

4.3.1 In ‘autumn’.....70

4.3.2 In ‘winter’.....72

Chapter 5 Conclusions 83

Appendix A	Calculation of the radiative effects of dust in Martian atmosphere	86
A.1	Single scattering.....	86
A.2	Multiple scattering.....	91
A.3	Evaluation of the optical depth.....	92
Appendix B	History of the Martian GCMs	94
B.1	Since 1969: Early developments.....	94
B.2	In 1990s: Four major Martian GCMs.....	94
B.3	In the 21st century: New attempts and new groups.....	95
Appendix C	Dust radiation scheme in the GCM	97
C.1	Radiative transfer equation of the solar radiation.....	97
C.2	δ -Eddington approximation of the phase function (Joseph et al., 1976).....	100
C.3	Calculation of the reflectivity, transmissivity and radiative source functions of the layer (two-stream DOM method, Nakajima and Tanaka, 1986; Nakajima et al., 2000).....	104
C.4	Infrared radiation.....	106
C.5	Calculation of fluxes (adding method).....	109
C.6	Calculation of the heating/cooling rates of atmosphere.....	112
Appendix D	Why the experiment without CO₂ 15μm radiation shows higher temperature?	113
Appendix E	Simulated zonal-mean circulation near the surface	118

References	121
Acknowledgements	131

Chapter 1

Introduction

1.1 Main features of the Martian atmosphere

Atmospheric conditions on Mars are very different from those on Earth. The dominant atmospheric component is CO₂ (95.3% of the atmosphere) and there is virtually no water except the subtropics in the northern summer and polar regions. The atmospheric temperature near the surface varies between ~200 K (~-73 °C) and ~260 K (~-13 °C) at the summer subtropics, according to the Mars Pathfinder observations [Schofield *et al.*, 1997]. Because Martian atmosphere is less dense than on Earth, the difference of temperature between day and night is significantly larger. The averaged surface pressure on Mars is about 6.1 mb, and it varies annually within the range of 25% of the averaged pressure, because the atmospheric component of CO₂ condenses at the polar regions [e.g. James *et al.*, 1992]. In addition, there is a peculiar feature in the Martian atmosphere, which is the existence of planetary-scaled dust storms.

Atmospheric dust is continuously supplied from the Martian surface, possibly because of two kinds of physical processes, one is the near-surface wind stress and the other is the small-scale convective vortices named ‘dust devils’ [e.g. Greeley and Iversen, 1985]. Especially in the southern spring and summer the dust storm activity becomes strong every Martian year, because the eccentricity of Mars is large (0.0934) and the perihelion of Mars is near the southern summer solstice (aerocentric longitude $L_s=250^\circ$ at perihelion, where $L_s=90^\circ$ and $L_s=270^\circ$ correspond to northern and southern summer solstices, respectively). The amount of insolation at the southern spring and summer is about 1.3 times larger, and therefore the atmospheric convection becomes stronger than that in the

northern spring and summer. The scale of dust storms that occur in this period differs for each year (from regional to planet-encircling), and hence atmospheric temperature has strong year-to-year variability according to the dust opacity. In the southern spring and summer, the observed maximum dust opacity for each year varies between 0.25 and 1.4 at the equator, according to the scales of occurred dust storms [Liu *et al.*, 2003].

In contrast, in the northern spring and summer the dust opacity and air temperature are lower and exhibit high year-to-year repeatability. Observed zonal-mean infrared ($9\mu\text{m}$) dust opacity at the equator, using a modified version of the retrieval scheme by *Martin* [1986], is around 0.05 in northern spring and summer at each year observed by Mariner 9 Infrared Interferometer Spectrometer (IRIS), Viking Infrared Thermal Mapper (IRTM) and the Thermal Emission Spectrometer (TES) on board Mars Global Surveyor (MGS).

1.2 Evaluation of the properties and radiative effects of Martian dust

1.2.1 Importance of dust for the Martian meteorology

The radiative effects of dust greatly influence the atmospheric temperature and structure, along with those of CO_2 . *Gierasch and Goody* [1972] first indicated using the vertical one-dimensional radiative-convective model that the observed vertical temperature profile could not be reproduced without the consideration of the solar absorption by dust. In addition, the following theoretical studies introducing the more realistic Martian dust parameters [*Moriyama*, 1974, 1975; *Zurek*, 1978] showed that the radiative effects of dust are important even when the dust layer is optically thin.

To calculate the radiative effects (absorption and scattering) of the Martian dust in the atmospheric model, the information on dust particle parameters (particle size distribution, shape distribution and wavelength-dependent refractive indices) is required. However, the direct measurements of these parameters were never made on Mars. The subsections to follow will provide an overview of how we evaluate them at present, and how we consider the radiative effects of dust in numerical models.

1.2.2 Particle size distribution

Presently, the determinations of the particle size distribution and shape distribution are done using the modified gamma function (or possibly log-normal function) and assuming spherical particles. Several measurements of the dust particle distribution have been made by Mariner 9 IRIS [Toon *et al.*, 1977], Viking Lander cameras [Pollack *et al.*, 1977, 1979, 1995], Phobos spacecraft [Drossart *et al.*, 1991; Korablev *et al.*, 1993] and the Imager for Mars Pathfinder (IMP) [Tomasko *et al.*, 1999; Markiewicz *et al.*, 1999]. Most of these measurements determine the average diameter of atmospheric dust as $\sim 2 \mu\text{m}$. As the most recent data up to now, Tomasko *et al.* [1999] proposed a particle size distribution $n(r)$ using the following modified gamma function:

$$n(r) = cr^{\frac{1-3v_{eff}}{v_{eff}}} \exp\left(-\frac{r}{r_{eff}v_{eff}}\right) \quad (1)$$

where r_{eff} and v_{eff} are the effective radius and effective variance, which are set to $1.6 \mu\text{m}$ and $0.2 \mu\text{m}$, respectively. A profile of the distribution is shown in Figure 1.

From the Mie theory, the particle size affects the scattering pattern. Larger size of particle produces stronger forward scattering, i.e. weaker extinction by scattering. [e.g. Shibata, 1999]. This tendency is larger for the wave with shorter wavelengths, so the ratio of opacity between for solar wavelengths and infrared wavelengths, which affects the temperature balance, highly depends on the particle size and its distribution.

1.2.3 Refractive indices

Concerning the refractive indices, most Martian atmospheric models at present use the refractive indices profiles by Ockert-Bell *et al.* [1997] (at the wavelengths shorter than $5 \mu\text{m}$), Toon *et al.* [1977] (between 5 and $17 \mu\text{m}$) and Forget [1998] (longer than $17 \mu\text{m}$). In solar wavelengths, Ockert-Bell *et al.* [1997] extracted the refractive indices at 4 wavelengths in the visible (0.5 - $0.86 \mu\text{m}$) from the particle size distribution, shape and single-scattering properties obtained by Pollack *et al.* [1995] using the doubling/adding radiative transfer model including Hapke theory [Hapke, 1981, 1986]. They also

extended the refractive indices to cover all the solar wavelengths (0.2-4.2 μm) using the spectra of OAO/WEP data [Wallace *et al.*, 1972; Owen and Sagan, 1972] at 0.2-0.4 μm , ground-based telescopic data by Bell *et al.* [1990] at 0.4-0.77 μm , Phobos-2 ISM data [Bibring *et al.*, 1989; Mustard *et al.*, 1993] at 0.77-2.9 μm , and ground-based telescopic data by Roush *et al.* [1992] at 2.9~4.2 μm . The calibration of all the data to the reflectance is based on the method of ISM data calibration [Mustard and Bell, 1994]. In infrared wavelengths, Toon *et al.* [1977] compared the Mariner 9 IRIS spectra at the wavelengths of 5-50 μm with the terrestrial mineralogical samples, and found that for the spectra shorter than 15 μm band, montmorillonite 219b, a clay mineral sample with at least 60 % of SiO_2 , have the best fit. In the wavelengths longer than the 15 μm band, Forget [1998] introduced the ‘synthetic’ model made to match the Mariner 9 IRIS spectra.

Meanwhile, Wolff and Clancy [2003] suggested another refractive indices profile between the wavelengths of 0.2 and 135 μm from the combination of previous work, as described below, and iterative adjustment using a variety of the MGS-TES observations. This profile is based on a Hawaiian palagonite sample [Roush *et al.*, 1991; Clancy *et al.*, 1995], with some following exceptions. The information from G. Hansen [2001, personal communication] and K. Snock [2001, personal communication] are adopted in 7.7-10.5 μm and 20-35 μm , respectively. In the wavelengths longer than 35 μm , a power-law extrapolation is adopted due to the lack of laboratory data. In 0.3-2.9 μm , the profile is made to fit the estimations from the observations by IMP [Tomasko *et al.*, 1999].

Figure 2 shows the comparison of the refractive indices profiles between by Ockert-Bell *et al.* [1997], Toon *et al.* [1977] and Forget [1998] (hereafter ‘Refractive A’) and Wolff and Clancy [2003] (hereafter ‘Refractive B’). Imaginary part of the refractive index represents the effects of absorption by dust, and we can see that it is larger in ‘Refractive A’ than ‘Refractive B’ in ultraviolet and visible wavelengths (0.2-0.5 μm). This shows that the dust with ‘Refractive A’ is expected to absorb more solar radiation in daytime, which is expected to produce higher temperature fields.

1.2.4 Calculation of the radiative fluxes

If a spherical particle is assumed and the refractive indices profile is known, the wavelength-dependent extinction, absorption and scattering efficiencies and the phase

function of the dust particle for single scattering can be calculated using the Mie theory. From these data and from the size distribution of dust particles, the extinction, absorption and scattering coefficients and the phase function for multiple scattering are obtained [e.g. *Liou, 2002*]. The optical depth of dust can be calculated from them and the spatial mixing ratio. Detailed calculations are described in Appendix A.

In the atmospheric model, the atmosphere is divided vertically to several layers. The optical depth in each layer is calculated, and the upward and downward radiative fluxes to derive the heating/cooling rate of atmosphere in each layer are computed for each wavelength using the optical depth, single-scattering albedo and scattering phase function. In most cases, the fluxes are calculated using the two-stream approximation [e.g. *Meador and Weaver, 1980; Toon et al., 1989*].

The radiative fluxes due to the dust are calculated separately in several spectral bands including both solar and infrared intervals. Most atmospheric models calculate the fluxes with one or two spectral bands in solar wavelengths and two or three spectral bands in infrared wavelengths, dividing inside and outside the CO₂ 15μm band [e.g. *Forget et al., 1999*]. In all bands outside the CO₂ 15μm band, the absorption, scattering and the infrared emission (in infrared wavelengths) by dust and the solar insolation (in solar wavelengths) are taken into account. In the determination of the phase function for the scattering effects by dust, the δ -Eddington approximation [*Joseph et al., 1976*] is used. Inside the CO₂ 15μm band, the scattering is ignored, and the absorption by dust is added to the absorption by CO₂. Some models ignore the radiative effects of dust inside the CO₂ 15μm band [*Wilson and Hamilton, 1996; Moudden and McConnell, 2005*].

1.2.5 Vertical distribution

A vertical distribution of dust is required to calculate radiative effects of dust at each altitude, although there are no its direct observations. For use in the atmospheric model, *Conrath [1975]* assumed a theoretical formula of the dust mixing ratio q_d as a function of the height z , from the vertical mixing in terms of an effective diffusivity and gravitational settling:

$$q_d(z) = q_{0d} \exp\left\{v \left[1 - \exp\left(\frac{z}{H}\right)\right]\right\} \quad (2)$$

where q_{0d} is the value of q_d at $z=0$, H is the scale height and v is the ratio of the characteristic diffusion time to the gravitational settling time which determines the dust cut-off altitude. This formula can be rewritten using p , the pressure at the height z , and p_0 , the pressure at the surface.

$$q_d(z) = q_{0d} \exp\left\{v \left[1 - \left(\frac{p_0}{p}\right)\right]\right\} \quad (3)$$

Conrath [1975] also estimated that $v=0.007$ is appropriate during the global dust storm from Mariner 9 television pictures of the limb [*Leovy et al.*, 1972]. However, *Pollack et al.* [1990] and *Wilson and Hamilton* [1996] adopted $v=0.03$ and $v=0.01$, respectively, in their Martian General Circulation Models (GCMs) to be the dust cut-off altitude lower. They used a horizontally uniform distribution of dust in their GCM runs. In reality, however, the vertical distribution of dust strongly varies in space and time. The dust altitude is always higher in the equatorial zone than in high latitudes of both hemispheres, and the decay of the dust is stronger towards the poles in both hemispheres, as follows from the limb observations by the camera on board Mariner 9 [*Anderson and Leovy*, 1978] and Viking Orbiter [*Jaquin et al.*, 1986]. For this reason, *Forget et al.* [1999] adopted the modified version of equation (3) in their Martian GCM:

$$q_d(z) = q_{0d} \exp\left\{0.007 \left[1 - \left(\frac{p_0}{p}\right)^{\frac{70}{z_{\max}}}\right]\right\} \quad (4)$$

where z_{\max} is the altitude (km) of the top of the dust layer and varies with latitude and season.

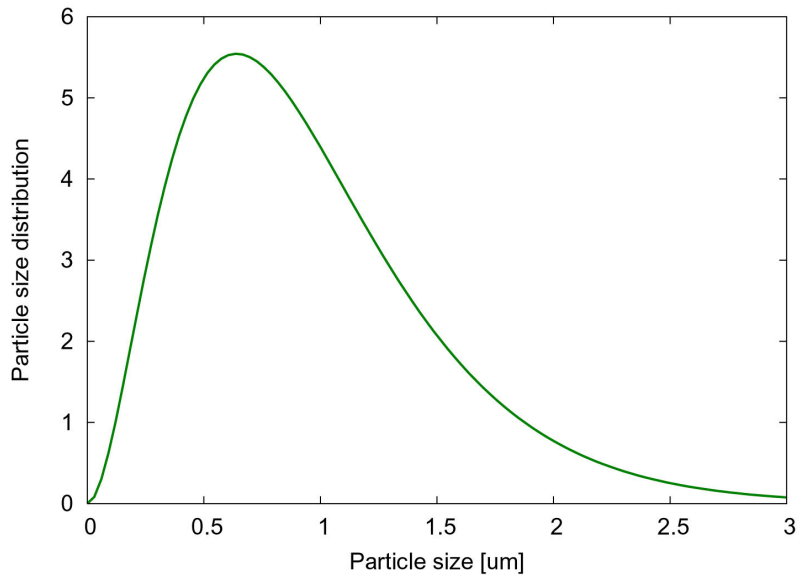


Figure 1: Particle size distribution of Martian dust proposed by *Tomasko et al.* [1999]. In this figure, the constant c in equation (1) is set to 100.

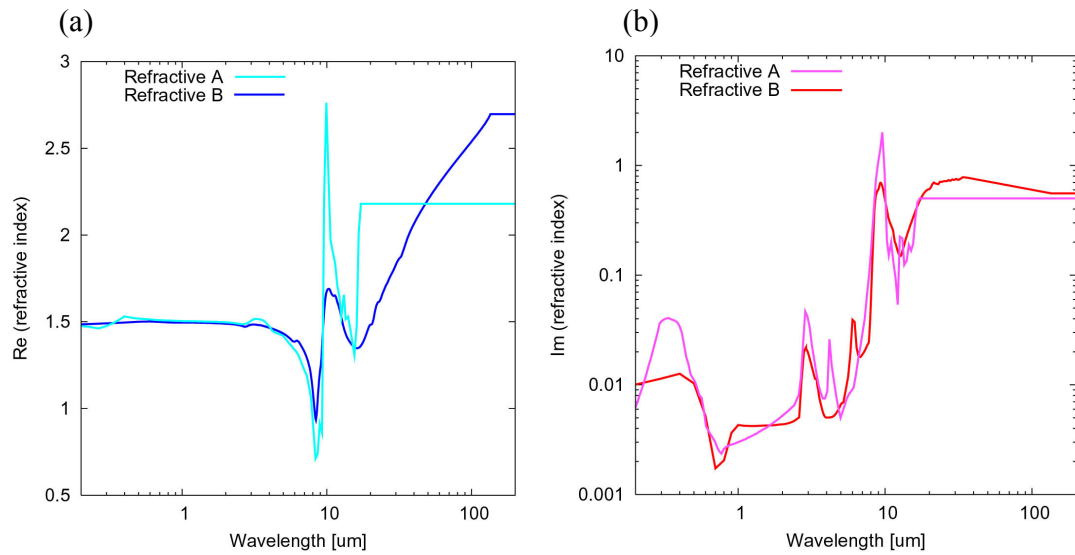


Figure 2: Wavelength distributions of (a) real and (b) imaginary part of refractive indices of Martian dust, the comparison between 'Refractive A' and 'Refractive B'.

1.3 Impact of the global dust storm on the atmospheric temperature

A planet-encircling dust storm, which sometimes occurs during southern springs and summers, greatly affects the Martian meteorology. Figure 3 shows the variance of the dust opacity and daytime atmospheric temperature observed by MGS-TES [Smith, 2004]. This figure shows that the planet-encircling dust storm begins soon after the northern autumn equinox ($L_s=180^\circ$) in Mars Year 25 (corresponding to June 2001 in the Earth calendar). The atmospheric temperature at 0.5 and 1.4 mb rises by ~ 40 K above the equator during the storm compared to the same season in previous Martian year (Mars Year 24) when a dust storm did not occur, while almost the same at 3.7 mb. Figure 4 shows the zonal-mean daytime temperature averaged over $L_s=205^\circ$ - 210° , both with and without a global dust storm, and Figure 5 shows the rise of the temperature owing to the global dust storm. The maximum rise at the equator is ~ 40 K at 0.2-0.5 mb, and the largest value is seen above the south pole at ~ 0.2 mb, is more than 60 K. Meanwhile, the temperature near the surface becomes ~ 10 K colder owing to the planet-encircling dust storm. The rise of the temperature is seen up to the height of 0.01 mb (~ 60 km) [Gurwell *et al.*, 2005], as shown in Figure 6.

Thus, the global dust storm significantly affects the temperature structures in the lower and middle atmosphere of Mars. The change of temperature possibly affects the stability of the atmosphere and the vertical wind shear related to the meridional gradient of temperature, and influences the atmospheric dynamics.

1.4 Baroclinic waves in the Martian atmosphere

Figures 7 and 8 show the day-mean surface pressure observed by Viking Lander 2 (at 47.97° N, 225.74° W) and the dust opacity observed by Viking spacecraft in the corresponding period, respectively. In Figure 7, the oscillation with the period of more than 1 Sol (a Martian solar day which equals to 88,775 seconds) is seen from autumn to spring, which is thought to be due to the passage of the baroclinic waves owing to the vertical wind shear. In addition, it is seen that the oscillation is reduced significantly

during $L_s=280-310^\circ$ of the first year, which is during the second planet-encircling dust storm in Figure 8, while such a reduction is not seen during the first planet-encircling dust storm in $L_s=210^\circ-250^\circ$. According to the spectral analyses by *Barnes* [1980, 1981], the estimated zonal wavenumbers and phase speeds of the dominant baroclinic wave components except during the second planet-encircling dust storm are 1-4 and 15-20 m s^{-1} , respectively. This is consistent with the theoretical expectations by *Leovy* [1969, 1979] and the early Martian GCM results with 2 or 3 vertical layers [*Leovy and Mintz*, 1969; *Pollack et al.*, 1981]. During the second planet-encircling dust storm, the amplitudes, wavenumbers and phase speeds of the dominant baroclinic waves become weaker, larger and slower significantly, respectively, as shown in Figure 9 and Table 1. This seems to be because the global dust storm changes the stability and vertical wind shear of atmosphere drastically, and suppress the onset of baroclinic waves.

Recently, vertical and meridional amplitude cross-section of the baroclinic waves are analyzed using the MGS-TES temperature data. Figure 10 shows the amplitudes of the waves with zonal wavenumber of 1 and 2 (hereafter WN=1 and WN=2, respectively) for different seasons in Mars Year 24 (without global dust storm), analyzed by *Banfield et al.* [2004]. For $L_s=195-225^\circ$ (northern autumn), WN=1 and WN=2 components have similar magnitudes near the surface in the northern hemisphere, while WN=1 is dominant higher. For $L_s=285-315^\circ$ (northern winter), the amplitude of WN=1 becomes larger than in autumn at upper altitudes, and the WN=1 and WN=2 waves do not penetrate northward of $\sim 70^\circ$ N at lower altitude, while they reaches to $\sim 80^\circ$ N in autumn. Figure 11 shows the amplitudes of the waves for $L_s=195-225^\circ$ in Mars Year 25, during a planet-encircling dust storm. There are little changes of the wave structure owing to the global dust storm in autumn, unlike in winter.

Thus, there are some different characteristics for the wave structures between autumn and winter, when without a global dust storm. In addition, a planet-encircling dust storm in winter seems to affect the structures of the baroclinic waves significantly, such as to decrease the amplitude and to increase the dominant wavenumber, while not so much in autumn.

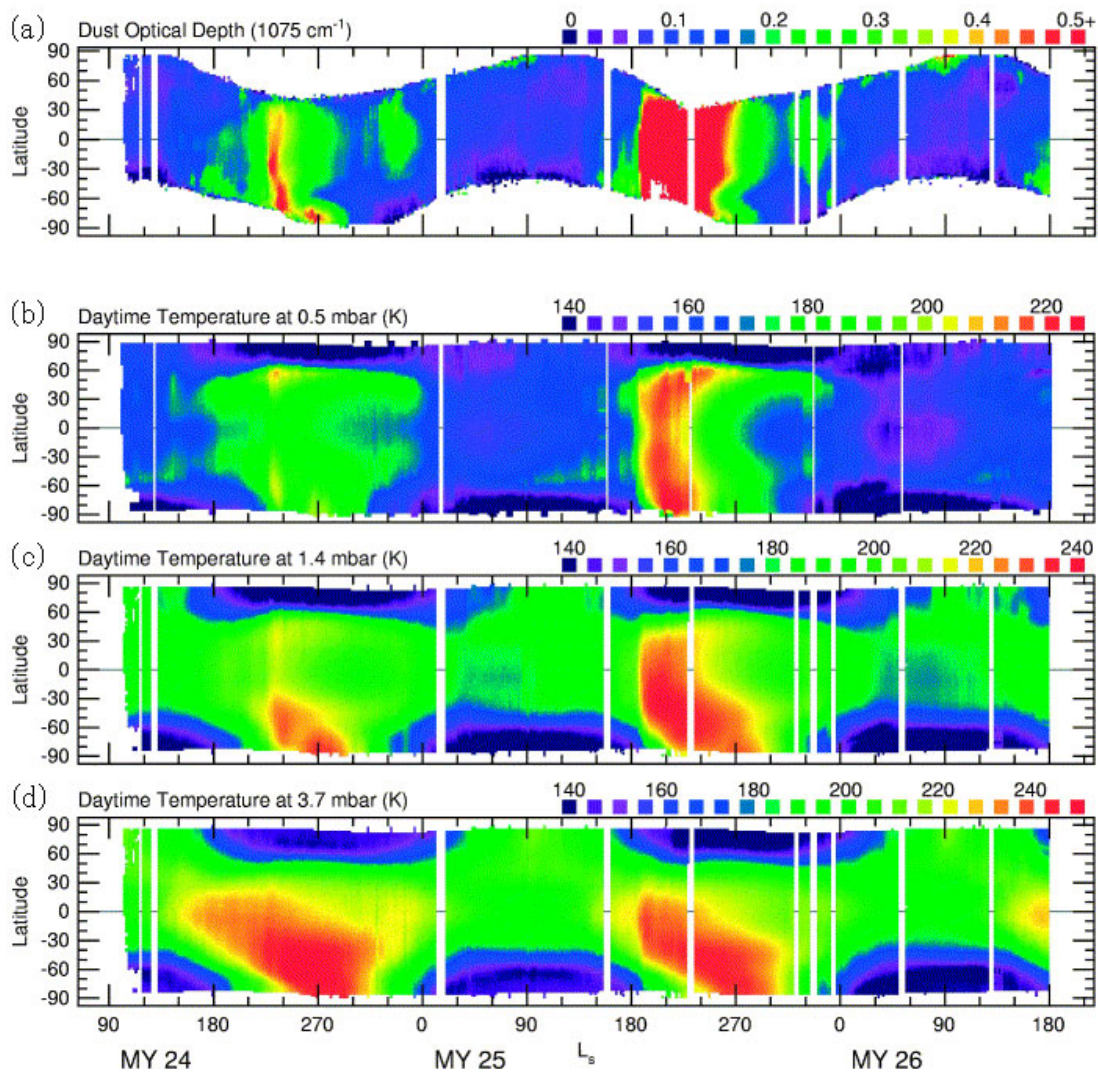


Figure 3: Daytime (local time ~ 1400) MGS-TES observations: (a) dust optical depth at 1075 cm^{-1} (wavelength of $9.3 \mu\text{m}$); (b) atmospheric temperature at 0.5 mb (~ 25 km above a nominal 6.1-mb surface); (c) atmospheric temperature at 1.4 mb (~ 15 km); and (d) atmospheric temperature at 3.7 mb (~ 5 km) from 1 March 1999 ($L_s=180^\circ$ in Mars Year 24) to 4 May 2003 ($L_s=180^\circ$ in Mars Year 26) [Smith, 2004].

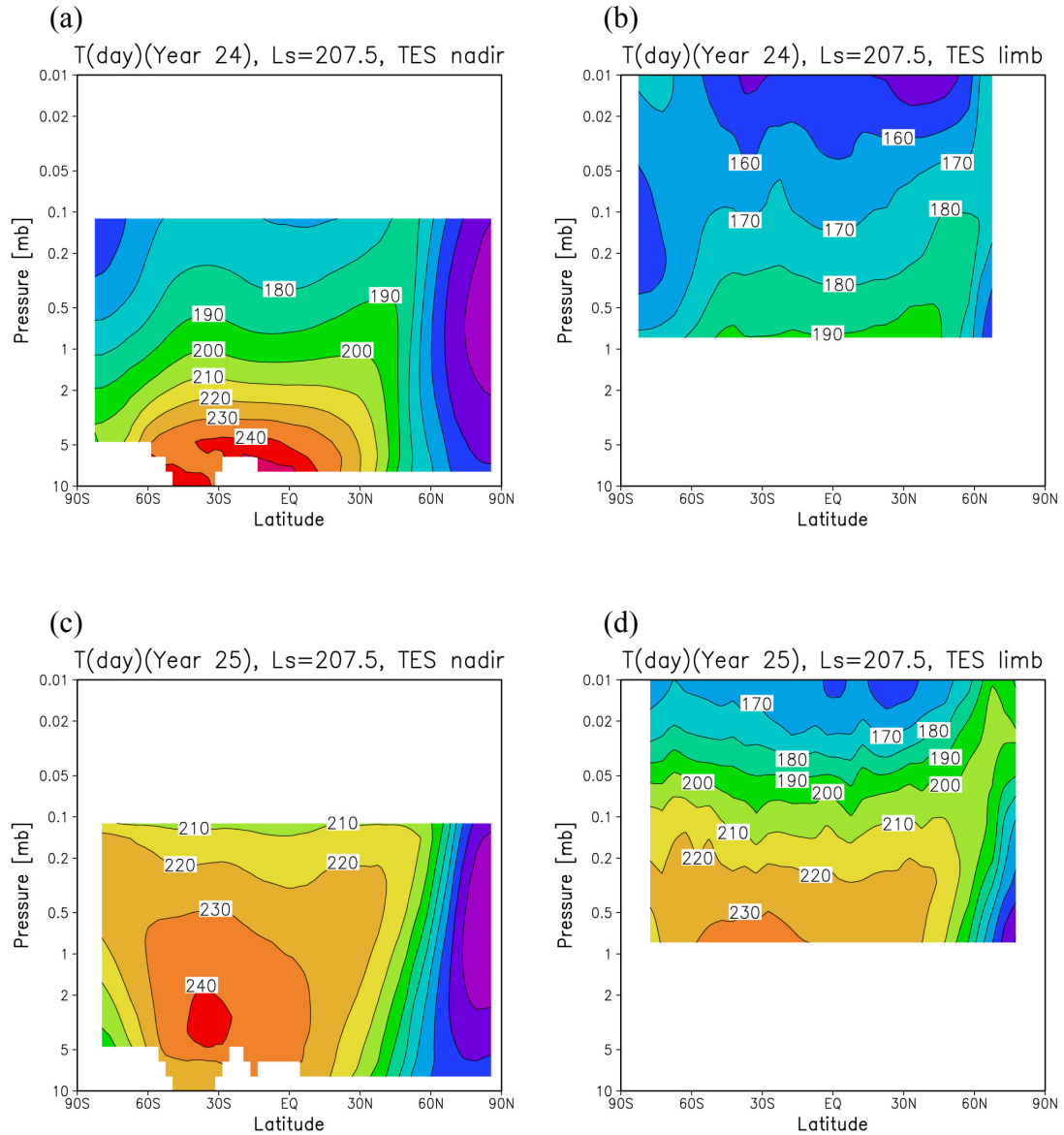


Figure 4: Zonal-mean daytime (local time ~ 1400) temperature [K] averaged over $L_s=205^\circ$ - 210° : (a) and (b) are in Mars Year 24 (without a planet-encircling dust storm) by MGS-TES nadir and limb observations, respectively. (c) and (d) are the same as (a) and (b), respectively, except for Mars Year 25 (with a planet-encircling dust storm).

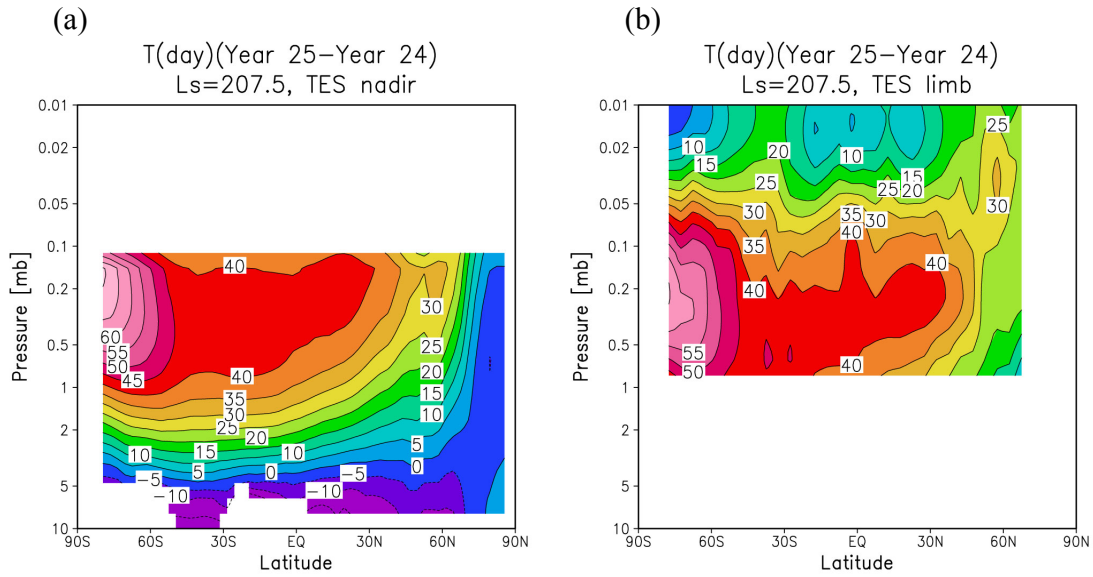


Figure 5: The rise of zonal-mean daytime (local time ~ 1400) temperature [K] averaged over $L_s=205^\circ$ - 210° owing to a global dust storm: (a) is the difference subtracting Figure 4a from Figure 4c, and (b) is the difference subtracting Figure 4b from Figure 4d.

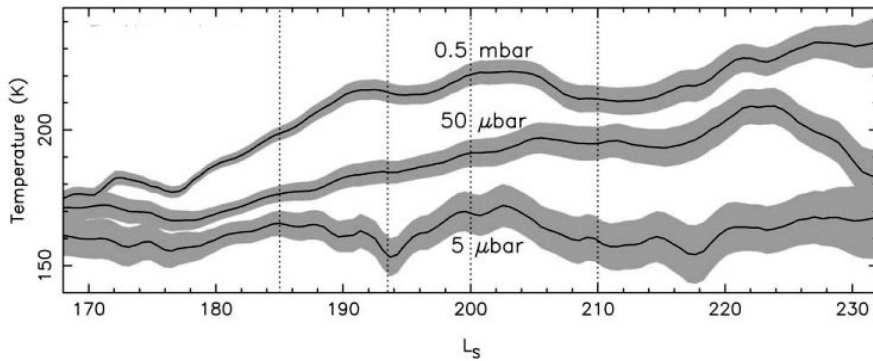


Figure 6: The earth-orbiting Submillimeter Wave Astronomy Satellite (SWAS) observations of global-mean atmospheric temperature in 2001 [Gurwell *et al.*, 2005]. Grayscale represents the formal statistical error of the temperature. Four vertical dotted lines refer to observations of atmospheric dust as measured by MGS-TES [Smith *et al.*, 2002]; from left to right, the period the storm begins rapid growth from smaller regional storms, the storm becomes planet-encircling, the averaged dust opacity become largest in the southern hemisphere, and the averaged dust opacity become largest in the northern hemisphere.

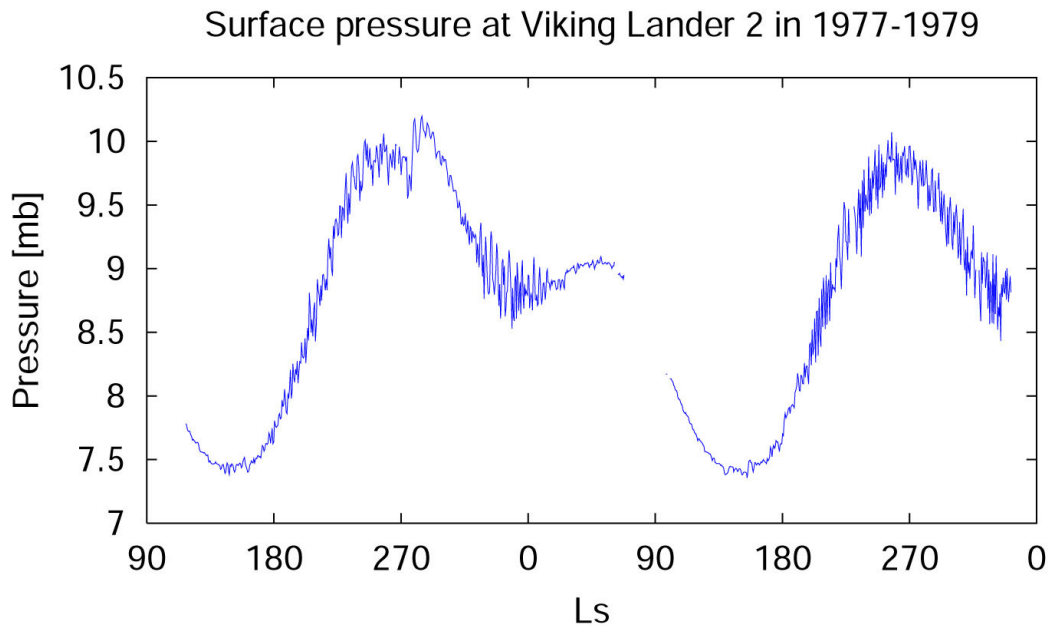


Figure 7: The daily-averaged surface pressure [mb] observed by Viking Lander 2 (at 47.97° N, 225.74° W) from 5 days after landing in 1977 ($L_s=120^\circ$) to $L_s=340^\circ$ in the following Martian year. The plotted data were taken from *Lee* [1995].

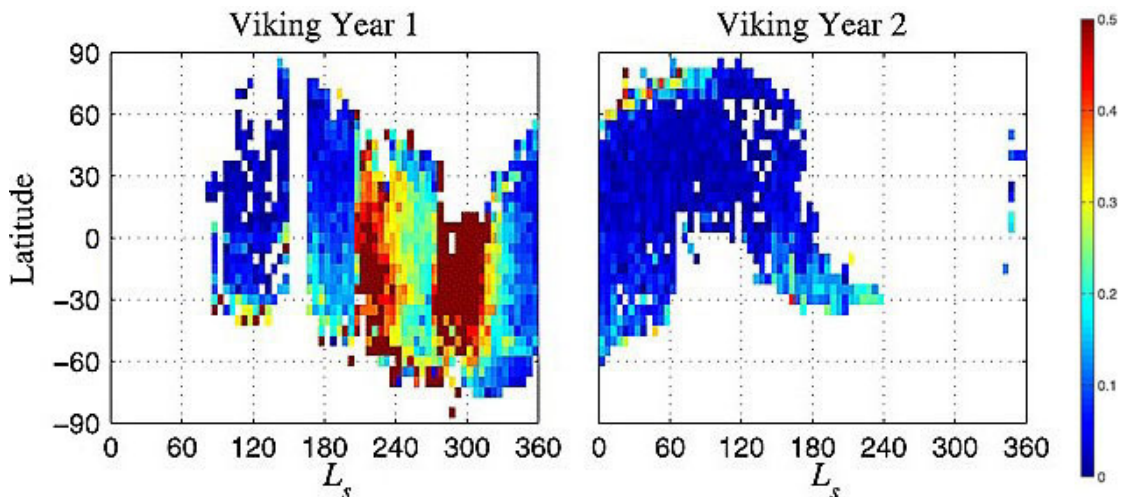


Figure 8: Zonal mean dust opacity observed by Viking IRTM (9- μ m channel wavelengths) [*Liu et al.*, 2003]: $L_s=120^\circ$ in Viking Year 1 and $L_s=340^\circ$ in Viking Year 2 correspond to the time of the beginning and end of plots in Figure 7, respectively.

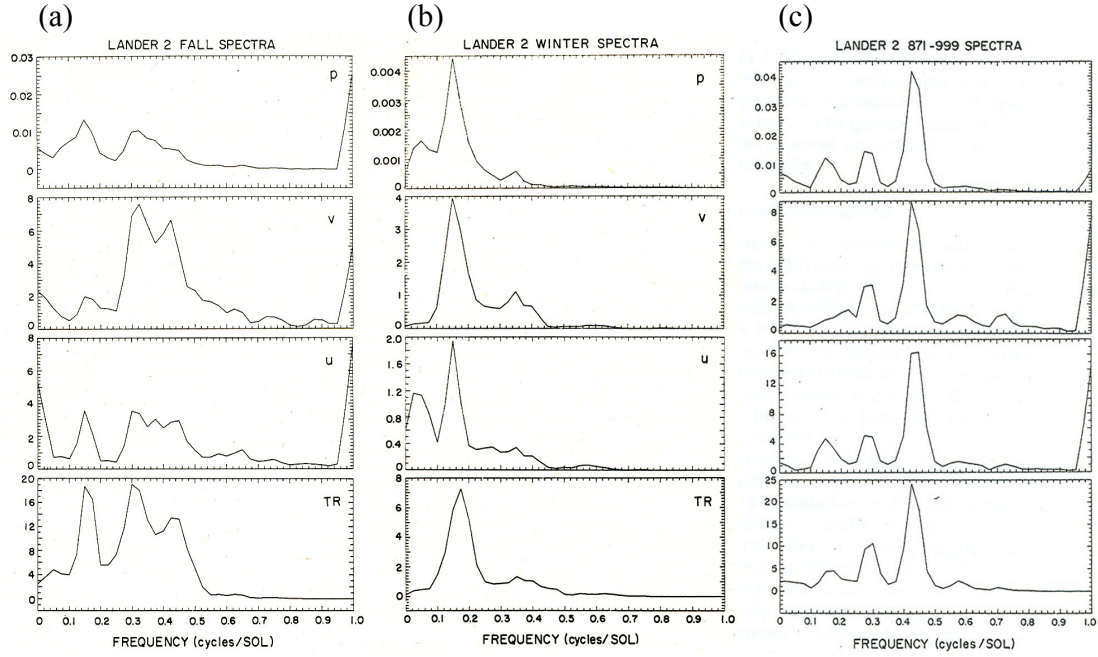


Figure 9: Power spectra of pressure (p), meridional wind (v), zonal wind (u) and reference temperature (TR) for (a) $L_s=195-249^\circ$ in the first year, (b) $L_s=280-313^\circ$ in the first year and (c) $L_s=230-312^\circ$ in the second year at Viking Lander 2 [Barnes, 1980, 1981]. The power spectral density values are given as the variance per unit angular frequency interval, where the pressure unit is mb, the wind m s^{-1} and the temperature K.

Year, Time and Period [Sols]	Wavenumber	Phase speed [m s^{-1}]
First, $L_s=195-249^\circ$, 6.7	1.6	14.9
First, $L_s=195-249^\circ$, 3.1	3.5	14.9
First, $L_s=195-249^\circ$, 2.3	4.3	16.0
First, $L_s=280-313^\circ$, 6.7	4.8	5.5
First, $L_s=280-313^\circ$, 2.9	7.1	7.9
Second, $L_s=230-312^\circ$, 6.7	1.5	15.9
Second, $L_s=230-312^\circ$, 3.5	3.0	15.3
Second, $L_s=230-312^\circ$, 2.3	3.4	20.5

Table 1: The estimated zonal wavenumbers and phase speeds of the baroclinic waves [Barnes, 1980, 1981].

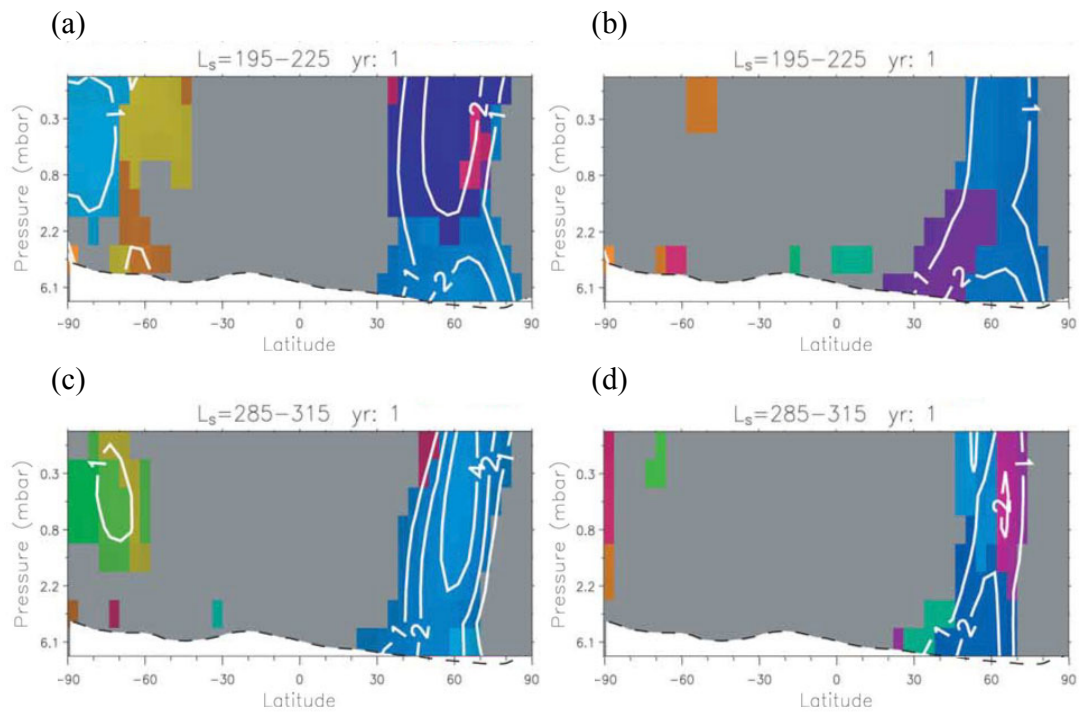


Figure 10: Amplitudes of the waves [K] (contour) in Mars Year 24: (a) for $L_s=195-225^\circ$, WN=1; (b) for $L_s=195-225^\circ$, WN=2; (c) for $L_s=285-315^\circ$, WN=1 and (d) for $L_s=285-315^\circ$, WN=2 [Banfield *et al.*, 2004]. Color represents the periods of the waves, showing ~ 6 Sols for WN=1 and ~ 3 Sols for WN=2, respectively, near the surface.

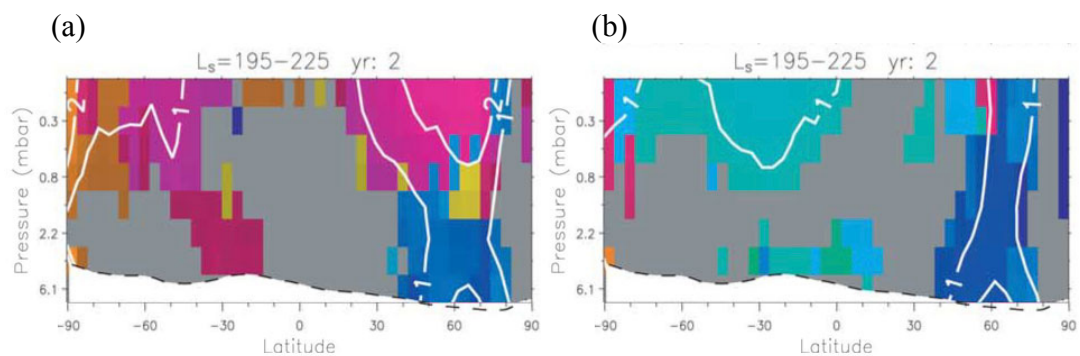


Figure 11: (a) and (b) are the same as Figure 10a and 10b, respectively, except in Mars Year 25 (during a planet-encircling dust storm).

1.5 Importance of this work

A General Circulation Model (GCM) is a very useful tool to study the atmospheric dynamics in three dimensions. *Leovy and Mintz* [1969] developed the first Martian GCM in 1969. The detailed history of studies with Martian GCMs is given in Appendix B. Presently, more observational data from Mars Global Surveyor, Mars Express, Mars Exploration Rover etc. become available, and GCMs are indispensable for treating them as the current state-of-the-art in Martian atmospheric studies.

Linear instability calculations were applied in studying Martian baroclinic waves [e.g. *Barnes*, 1984; *Tanaka and Arai*, 1999]. This kind of study is useful in getting approximate growth rates of waves, but the results cannot accurately describe the reality, in particular, amplitudes cannot be determined. Studies using Martian GCMs have also been done [e.g. *Barnes et al.*, 1993; *Collins et al.*, 1996]. *Barnes et al.* [1993] performed the experiment to reproduce the baroclinic waves at different dust opacity. However, he did not reproduce the significant reduction of the waves during the second planet-encircling dust storm in 1977 even in the experiment with the dust opacity of 5. This is possibly because the 40-50 K warming above the north pole (as observed by Viking spacecraft [*Martin and Kieffer*, 1979]) was not reproduced. *Collins et al.* [1996] reproduced the waves with the periods of ~ 6 Sols for $WN=1$ and ~ 3 Sols for $WN=2$, which are consistent with the observations at lower dust opacity, but the change owing to the dust opacity was not shown.

I was involved in the development of a new Martian GCM, the Center for Climate System Research in University of Tokyo / National Institute for Environmental Studies (CCSR/NIES) Martian GCM [*Kuroda et al.*, 2005]. CCSR/NIES terrestrial AGCM (upon which the Martian GCM is built) has a solar and infrared radiative scheme that takes into account 16-19 wavelength intervals for the calculation of solar incidence, absorption, emission and scattering of gases, clouds and aerosols [*Numaguti et al.*, 1997; *Nakajima et al.*, 2000]. This framework was applied to the computations of the radiative effects of Martian dust in the Martian GCM. Compared to the previous studies with other Martian GCMs (five, at most), significantly more spectral bands are taken into account in the study reported on this thesis. In addition, in the CCSR/NIES Martian GCM, the infrared

radiative bands of CO₂, including 4.3 μm and 10 μm bands in addition to the strong 15 μm band, are also accounted for in this framework. Using this scheme allows one to check on fine details of the sensitivity of model results to the radiative effects of CO₂ and dust at each spectral band. This was never done before in other Martian GCMs.

In this study, the tests have been performed to estimate the sensitivity of the radiative and dynamical response to the presence of different CO₂ infrared bands, and to variations of the following dust parameters: the particle size distribution, refractive indices, and dust opacity, using the CCSR/NIES Martian GCM. The model was applied to investigate the properties of Martian baroclinic waves during different seasons, and for different dust conditions. The study focused on the changes in the atmospheric stability and conditions that affect the generation and propagation of waves. The outline of the CCSR/NIES Martian GCM used in this study is given in Chapter 2. The sensitivity of the simulated thermal structures to the radiative parameters and the comparison with the observations are presented in Chapter 3. Chapter 4 describes the investigation of Martian baroclinic waves for different season and dust opacities. Chapter 5 presents the summary and conclusions.

Chapter 2

Outline of the CCSR/NIES Martian GCM

This chapter describes all the modifications and changes required to convert the CCSR/NIES terrestrial AGCM into the Martian counterpart. Some descriptions in this chapter have been published by *Kuroda et al.* [2005].

2.1 Basic features

The CCSR/NIES Martian GCM is based upon the CCSR/NIES terrestrial AGCM, as written in Section 1.5. The basic features of CCSR/NIES terrestrial AGCM are described by *Numaguti et al.* [1997]. The Martian model does not include water processes and the gravity wave drag parameterization, but incorporates a dry convective adjustment.

The physical parameters of the AGCM were changed according to the Martian environment. The Martian parameters and the comparisons with those for Earth are shown in Table 2.

2.2 Dynamics

The basic equations are the three-dimensional hydrostatic primitive equations on a sphere with normalized pressure (σ) coordinate. The horizontal resolution is set at $\sim 5.6^\circ$ longitude and $\sim 5.6^\circ$ latitude (T21, i.e., triangular truncation with wavenumber 21). The vertical resolution is 30 layers with σ -levels, as in Table 3, and the top altitude of the model is about 80km.

Parameters	Mars	Earth	Unit
Radius of planet	3397	6378	km
Acceleration of gravity	3.72	9.8	m s^{-2}
Atmospheric gas constant	188.86	287	$\text{J K}^{-1} \text{kg}^{-1}$
Atmospheric specific heat at constant pressure	735.9	1000	$\text{J K}^{-1} \text{kg}^{-1}$
Seconds per a solar day (Sol)	88776	86400	s
Amount of solar radiation	589.2	1367.6	W m^{-2}
Sols per a year	669	365	Sol
Eccentricity	0.0934	0.0167	-
Angle of equator inclination	25.19	23.45	degree

Table 2: The physical parameters used in CCSR/NIES Martian GCM (Mars), and the comparison with those for Earth.

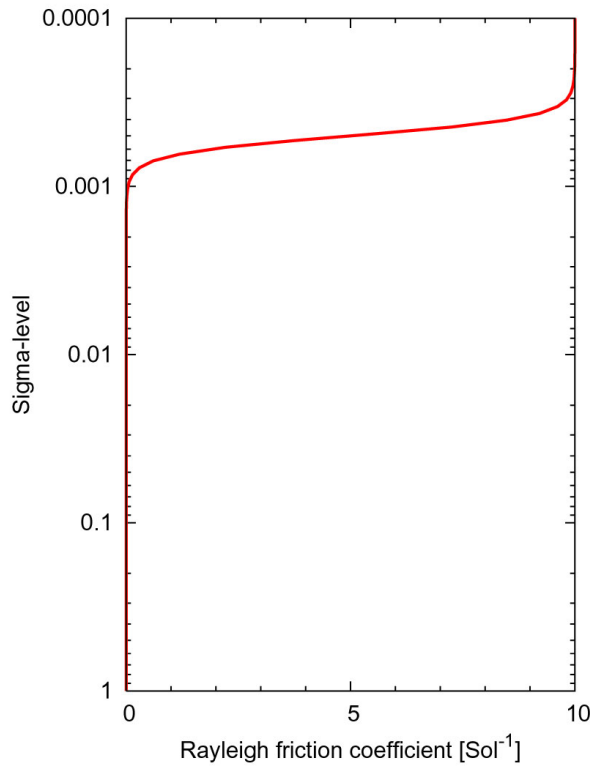


Figure 12: σ -level vertical distribution of the Rayleigh friction coefficient used in this model.

Layer	σ -levels	Approximate Altitudes [m]
1	0.99500	50.1
2	0.98500	151.1
3	0.97500	253.2
4	0.96500	356.3
5	0.95249	486.8
6	0.93749	645.5
7	0.91999	833.9
8	0.89999	1053.7
9	0.87497	1335.7
10	0.84497	1684.5
11	0.80994	2108.0
12	0.76490	2680.1
13	0.70985	3427.0
14	0.63970	4467.6
15	0.54946	5988.2
16	0.45447	7886.2
17	0.36948	9956.6
18	0.29450	12224.8
19	0.22953	14717.2
20	0.17457	17454.3
21	0.12440	20842.5
22	0.084683	24688.4
23	0.059801	28167.3
24	0.039699	32264.3
25	0.024880	36936.9
26	0.014797	42133.3
27	0.0079398	48358.7
28	0.0044392	54172.8
29	0.0019373	62464.6
30	0.00041495	77873.5

Table 3: Vertical resolution used in this model. Approximate altitudes are calculated from the formula $z=-H \ln \sigma$, in which H is the Martian scale height (~ 10 km).

Rayleigh friction is imposed near the upper boundary. The Rayleigh friction coefficient depends on σ -level as shown in Figure 12. The damping coefficient around the top boundary is $\sim 10 \text{ Sol}^{-1}$.

2.3 Surface parameters

The topography, albedo, and thermal inertia data for Mars surface are included in the model. The topography utilized in the model is based on the observations by the Mars Orbiter Laser Altimeter (MOLA) on MGS [Smith *et al.*, 1999]. The data set of surface albedo and surface thermal inertia is the same as that of LMD/AOPP Martian GCM [Forget *et al.*, 1999; thermal inertia data is fixed by Forget *et al.*, 2001]. The data are projected to the model's horizontal grid, as shown in Figures 13, 14 and 15.

The model includes the land scheme that calculates the thermal conduction in the soil, with 7 layers down to the depth of 2 m. The thermal conductivity and specific heat per unit volume of the soil is vertically homogeneous, and are computed from the thermal inertia according to Mellon [2001].

2.4 CO₂ condensation/sublimation processes

CO₂ condensation and sublimation processes are included in this model, using the same method as Forget *et al.* [1998]. The condensation temperature of CO₂ is given by the Clausius-Clapeyron relation [Hourdin *et al.*, 1995].

When the atmospheric temperature predicted from the dynamical and radiative cooling rates falls below the freezing temperature, the condensation occurs and the latent heat is released to keep the atmospheric temperature at the condensation temperature. The condensed CO₂ is set to fall to the surface instantly, because the radius of CO₂ ice particle is estimated to more than 10 μm [Forget *et al.*, 1995] which most of the condensed CO₂ in the atmosphere can fall to the ground within a model timestep (~ 400 seconds). The potential energy released by the falling ice and the energy used to heat the ice up to the

condensation temperature at the lower level are taken into account in calculating the mass of the condensed CO₂. The condensation takes place both in the atmosphere and on the ground. The loss of the atmospheric mass due to the condensation (or, conversely, the gain due to the sublimation) is taken into account by modifying the surface pressure to conserve the total mass of CO₂ (caps + atmosphere).

The value of the surface albedo is set to 0.65 for the surface covered with the CO₂ ice.

2.5 Radiation

A characteristic and unique feature of this Martian GCM is the following radiative scheme for CO₂ and dust.

2.5.1 CO₂ gas

The absorption and emission by the strong CO₂ 15 μm, 10 μm and 4.3 μm bands and the Rayleigh scattering by the molecules are computed by the radiative scheme MSTRN-X based on the *k*-distribution method [Nakajima *et al.*, 2000] with improvements made by Sekiguchi [2004] to suit the upper stratosphere conditions of Earth. No other Martian GCMs take into account the CO₂ 4.3 μm and 10 μm infrared bands. The absorption/emission by the CO₂ band and Rayleigh scattering are considered, and the radiative fluxes are calculated using the two-stream discrete ordinate method [Nakajima and Tanaka, 1986]. The effects of atmospheric heating due to the absorption of the solar radiation in the near-infrared band are included by calculating the heating rate with a simple analytical formula employed in LMD/AOPP Martian GCM [Forget *et al.*, 1999, 2003]. The formula is based on the one-dimensional model calculation of Lopez-Puertas and Lopez-Valverde [1995].

In both the solar and infrared schemes, a Local Thermodynamic Equilibrium (LTE) is assumed at all altitudes. The non-LTE processes are effective above ~80 km [Lopez-Valverde *et al.*, 1998], and are not considered in the model.

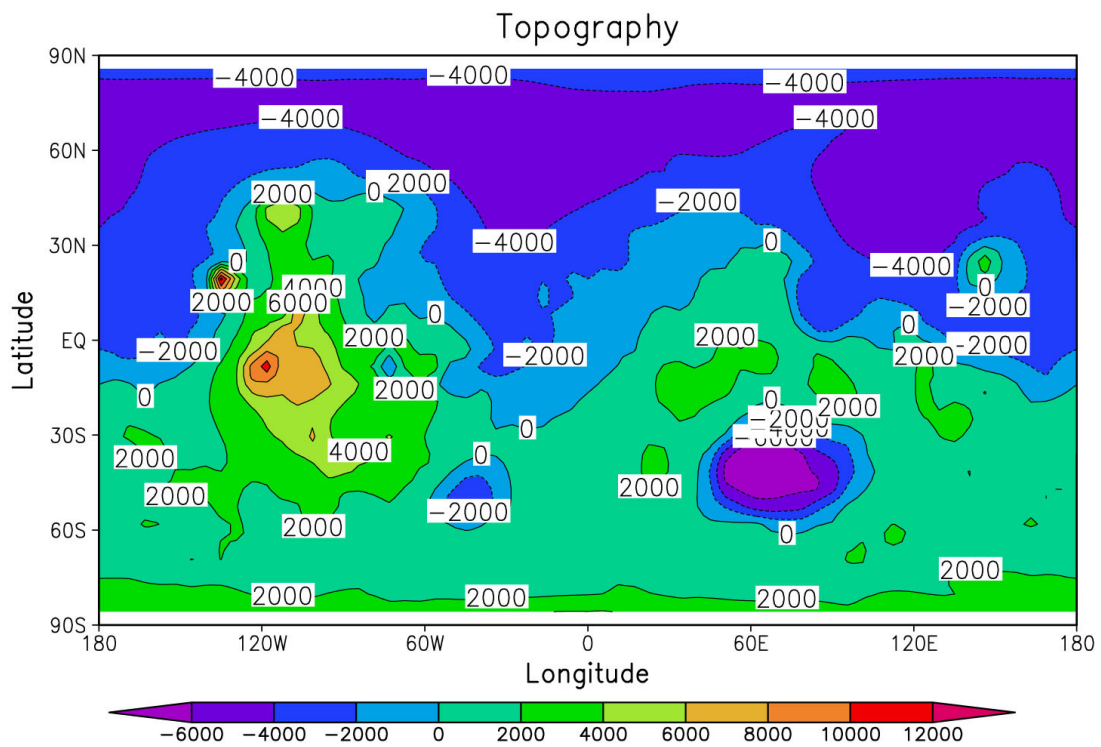


Figure 13: Latitude-longitude distribution of the topography [m] used in this model.

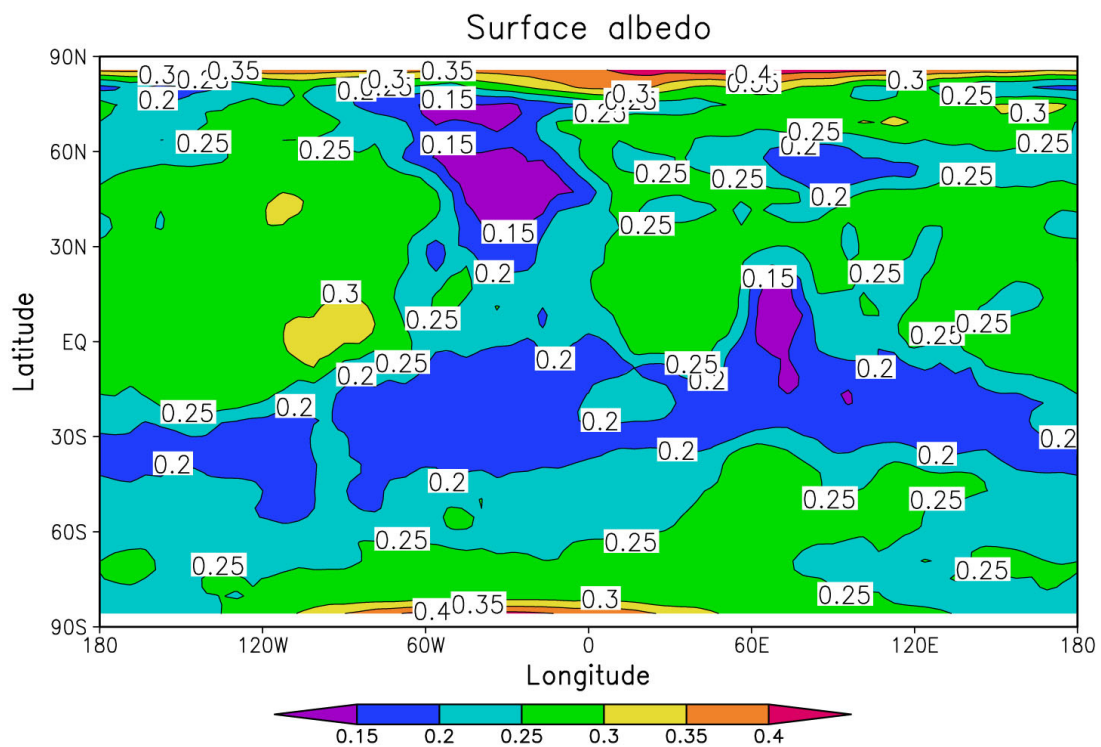


Figure 14: Latitude-longitude distribution of the surface albedo used in this model.

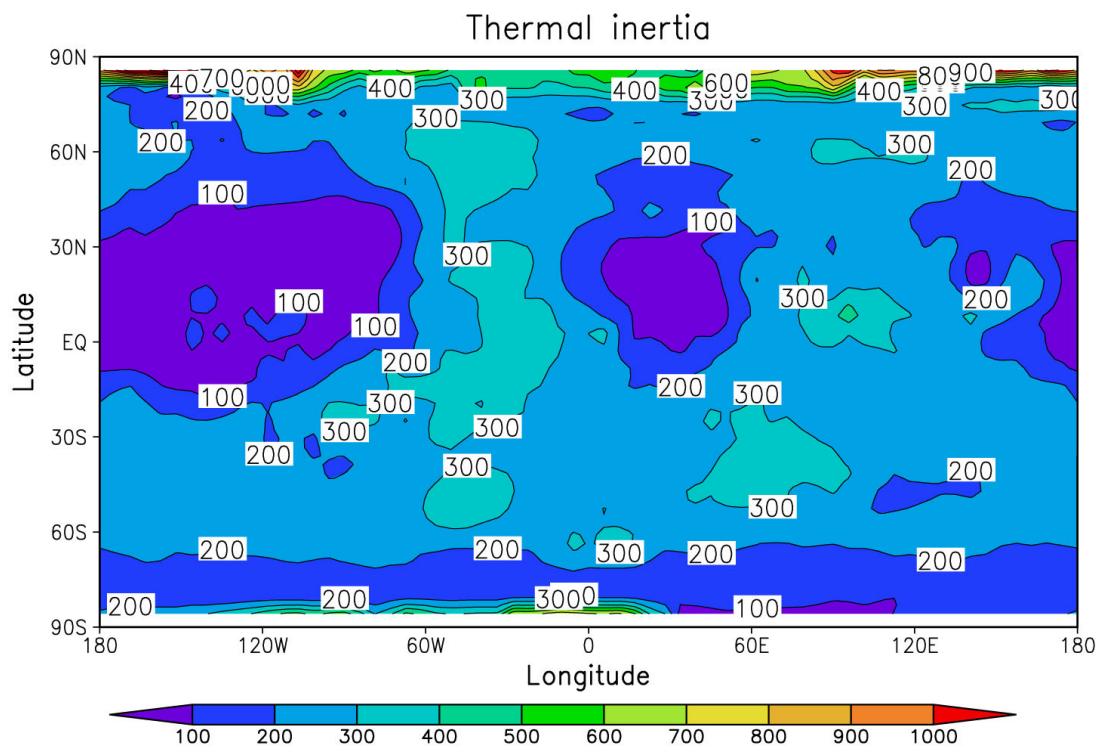


Figure 15: Latitude-longitude distribution of the surface thermal inertia [$\text{J m}^{-2} \text{K}^{-1} \text{s}^{-1/2}$] used in this model.

2.5.2 Dust

The absorption, emission and scattering by atmospheric dust are calculated using the Mie theory under the assumption of spherical particles. Adding the effects of CO₂ absorption/emission in some infrared wavelength bands and Rayleigh scattering to them, the radiative fluxes are calculated for the wavelengths between 0.2 μm and 200 μm utilizing 19 representative wavelength bands: 9 in the visible and 10 in the infrared spectral range, as in Table 4. This scheme is unique compared to other Martian GCMs, which consider 5 bands at most. The calculation of the fluxes at each band is described in detail in Appendix C.

Concerning the dust parameters, three kinds of the particle size distribution and refractive index data set, respectively, are considered in the sensitivity tests in Chapter 3. Each particle size distribution is shown in Figure 16. ‘PSD 1’ is the same as the one employed in the above plots, the effective radius of 1.6 μm and the effective variance of 0.2 μm , as observed by *Tomasko et al.* [1999] (see Subsection 1.2.2 and Figure 1). ‘PSD 2’ and ‘PSD 3’ are the distributions with the effective radius of 2.5 μm and 3.5 μm , respectively, and the effective variance of 0.2 μm . As for the refractive indices, ‘Refractive A-prime (A’), which is the same as ‘Refractive A’ but with uniform imaginary index of 0.01 in the wavelengths shorter than 0.5 μm , is introduced besides ‘Refractive A’ and ‘Refractive B’ (see Subsection 1.2.3 and Figure 2). The three profiles of imaginary refractive index (only for the wavelengths shorter than 2 μm) are shown in Figure 17.

2.6 Atmospheric dust distribution

To imitate the distribution of dust observed by MGS-TES and Viking, three dust scenarios which vary with time and latitude are introduced. They are denoted as the TES2, TES3 and VIK1 dust scenarios. The TES2 dust scenario is based on the dust opacity of TES Year 2 retrieved by *Liu et al.* [2003] (Mars Year 24, from July 1998 to May 2000, see Figure 3a). The TES3 and VIK1 dust scenarios are based on TES Year 3 (Mars Year 25, from May 2000 to April 2002, see Figure 3a) and Viking Year 1 (including two global dust storms in 1977, see Figure 7), respectively. The observations of the dust

opacity by *Smith et al.* [2001, 2002] and *Martin and Richardson* [1993] are also taken into account for determining the distributions in the TES2, TES3 and VIK1 scenarios, respectively. The dust is not transported in the simulations, and therefore the dynamical feedback is not taken into account.

To determine dust opacities at each latitude and time, we use the framework of the dust scenarios of the LMD/AOPP Martian GCM [*Lewis et al.* 2001], which calculates the optical depth at the equator, south and north poles as a function of the aerocentric longitude L_s . When a global dust storm occurs, the growth rate of the dust opacity is faster than the decreasing rate during the decay, according to the observations. To reproduce this feature, the growing dust opacity was approximated by a hyperbolic tangent. The distribution has the following analytical form:

If $L_s < L_{s1}$,

$$\tau_*(L_s) = 0.05 + \frac{\tau_{\max} - 0.05}{2} [1 + \tanh\{(L_s - L_{s0}) * \alpha\}] \quad (5)$$

If $L_s \geq L_{s1}$,

$$\tau_*(L_s) = 0.05 + (\tau_{\max} - 0.05) \{\cos((L_s - L_{s1})/2)\}^\beta \quad (6)$$

where τ^* represents the infrared dust opacity at 7 mb. The factors τ_{\max} is the maximum dust opacity in each regions, L_{s0} is the aerocentric longitude when dust storms occur most intensely, L_{s1} is the aerocentric longitude when the dust opacity begins to decrease, and α and β are the factors of increasing and decreasing rates of dust opacity. Larger α represents faster increase of dust opacity, and larger β represents faster decay. The values of these factors used in each dust scenarios are shown in Table 5. From τ^* calculated at the equator, south pole and north pole, τ_{eq} , τ_S and τ_N , the infrared optical depth at 7 mb, τ , on any point of the planet is interpolated using a hyperbolic tangent transition in northern hemisphere and a sine transition in the southern hemisphere:

$$\tau(\phi, L_s) = \tau_N + \frac{\tau_{eq} - \tau_N}{2} \{1 + \tanh(5(45^\circ - \phi))\} \quad (\phi > 0) \quad (7)$$

$$\tau(\phi, L_s) = \tau_s + \frac{\tau_{eq} - \tau_s}{2} \{1 + \sin(2(45^\circ + \phi))\} \quad (\phi < 0) \quad (8)$$

where ϕ is the latitude.

The vertical distribution of dust is determined based on the theoretical assumption by *Conrath* [1975], as described in Section 1.2. The revised formulae of *Forget et al.* [1999] and *Lewis et al.* [1999] are used, which employ the optical depth instead of the aerocentric longitude to determine the cut-off altitude of dust and set the difference of the cut-off altitude between the equator and the poles in half, as follows:

$$Q = Q_0 \exp \left\{ 0.007 \left[1 - \max \left[\left(\frac{p_0}{p} \right)^{\frac{70}{z_{\max}}}, 1 \right] \right] \right\} \quad (9)$$

$$z_{\max}(\phi, \tau) = 80 - 2(\tau - 2)^2 - 11 \sin^2 \phi \quad (10)$$

where z_{\max} is the cut-off altitude of dust (km), p is the pressure, p_0 is the standard pressure (7 mb), and Q and Q_0 are the dust mass mixing ratio at the pressure levels p and p_0 .

The time-latitude cross-sections of the dust opacity at the surface and the dust cut-off altitude in each scenario are shown in Figures 18 and 19, respectively. The dust opacity used in Figure 18 is the infrared (9-10 μm) value calculated in the model using ‘Refractive A’, to be consistent with the calibration by *Liu et al.* [2003]. The value of Q_0 depends on the refractive indices at 9-10 μm , and here Q_0 is set to 2.5×10^{-5} .

Band	S/I, CO ₂	Wavenumber [cm ⁻¹] range	Wavelength [μm] range
1	I	50-250	40-200
2	I	250-530	18.9-40
3	I, CO ₂	530-610	16.4-18.9
4	I, CO ₂	610-720	13.9-16.4
5	I, CO ₂	720-820	12.2-13.9
6	I, CO ₂	820-980	10.2-12.2
7	I, CO ₂	980-1175	8.5-10.2
8	I	1175-1400	7.1-8.5
9	I	1400-2000	5.0-7.1
10	I, CO ₂	2000-2500	4.0-5.0
11	S	2500-6000	1.667-4.000
12	S	6000-10000	1.000-1.667
13	S	10000-14750	0.678-1.000
14	S	14750-23000	0.435-0.678
15	S	23000-30000	0.333-0.435
16	S	30000-33500	0.299-0.333
17	S	33500-36000	0.278-0.299
18	S	36000-43500	0.230-0.278
19	S	43500-50000	0.200-0.230

Table 4: The band range of the radiation scheme used in this model. S/I represents whether solar (S) or infrared (I) radiation the band deals with, and ‘CO₂’ indicates that CO₂ absorption/emission is included in the band.

	TES2			TES3			VIK1(1)			VIK1(2)		
	N	EQ	S	N	EQ	S	N	EQ	S	N	EQ	S
τ_{max}	0.1	0.2	0.5	0.1	0.7	1.0	0.1	0.6	0.5	0.2	1.3	1.5
L_{s0}	225°	220°	215°	210°	190°	192°	216°	206°	206°	280°	272°	272°
L_{s1}	240°	235°	235°	230°	205°	205°	230°	215°	218°	295°	283°	283°
α	12	15	8	10	18	22	12	22	22	12	18	18
β	30	30	20	20	20	15	30	10	10	30	23	23

Table 5: Values of the factors used in equations (5)~(8) for deciding the time-latitude cross-sections of the three dust scenarios used in this paper. N, EQ and S correspond to the factors for calculating τ_N , τ_{eq} and τ_S , respectively. In the VIK1 dust scenario two major dust storms occur, so the optical depth τ is defined by $\tau = \max[\tau_1, \tau_2]$, where τ_1 and τ_2 are the optical depths of VIK1(1) and VIK1(2), respectively, in this table.

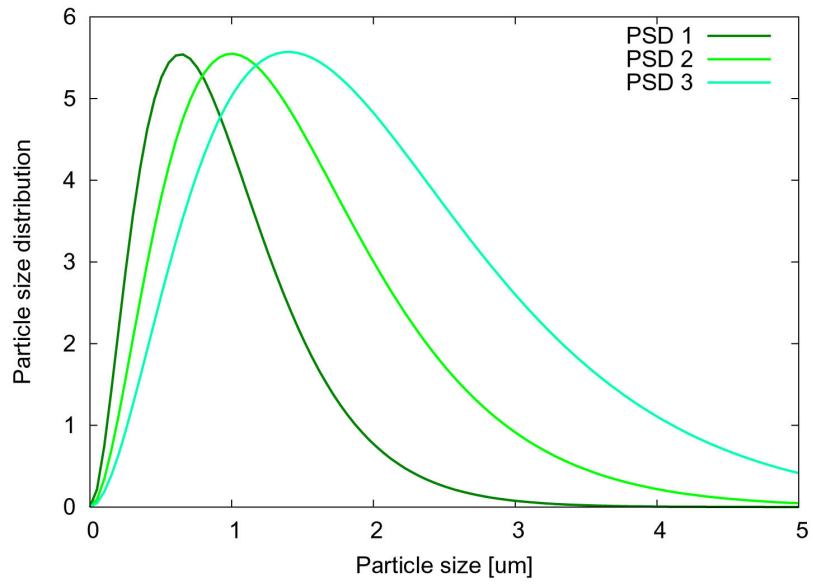


Figure 16: The particle size distributions used in this study.

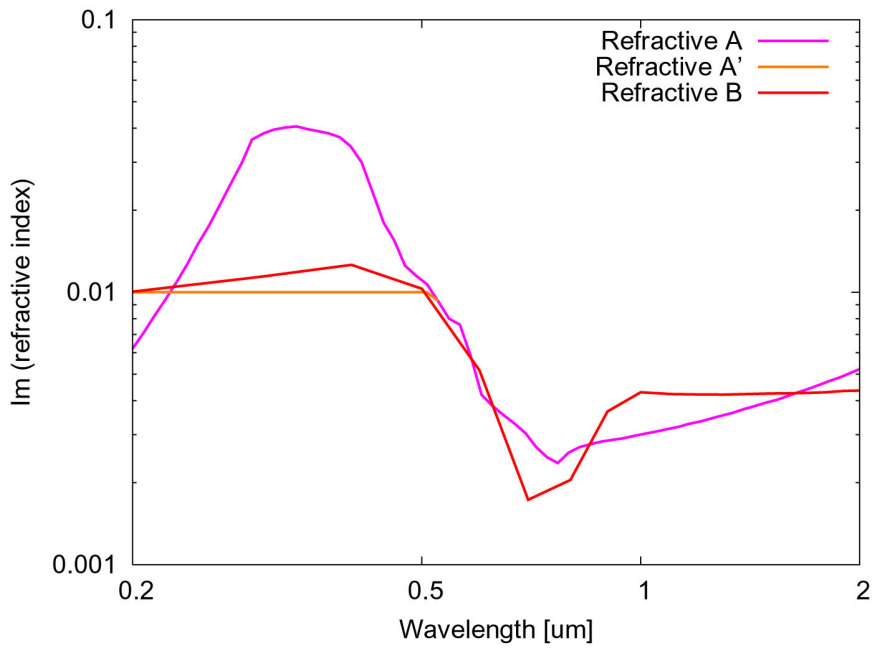


Figure 17: The imaginary parts of the refractive index profiles (for the wavelengths shorter than 2 μm) used in this study.

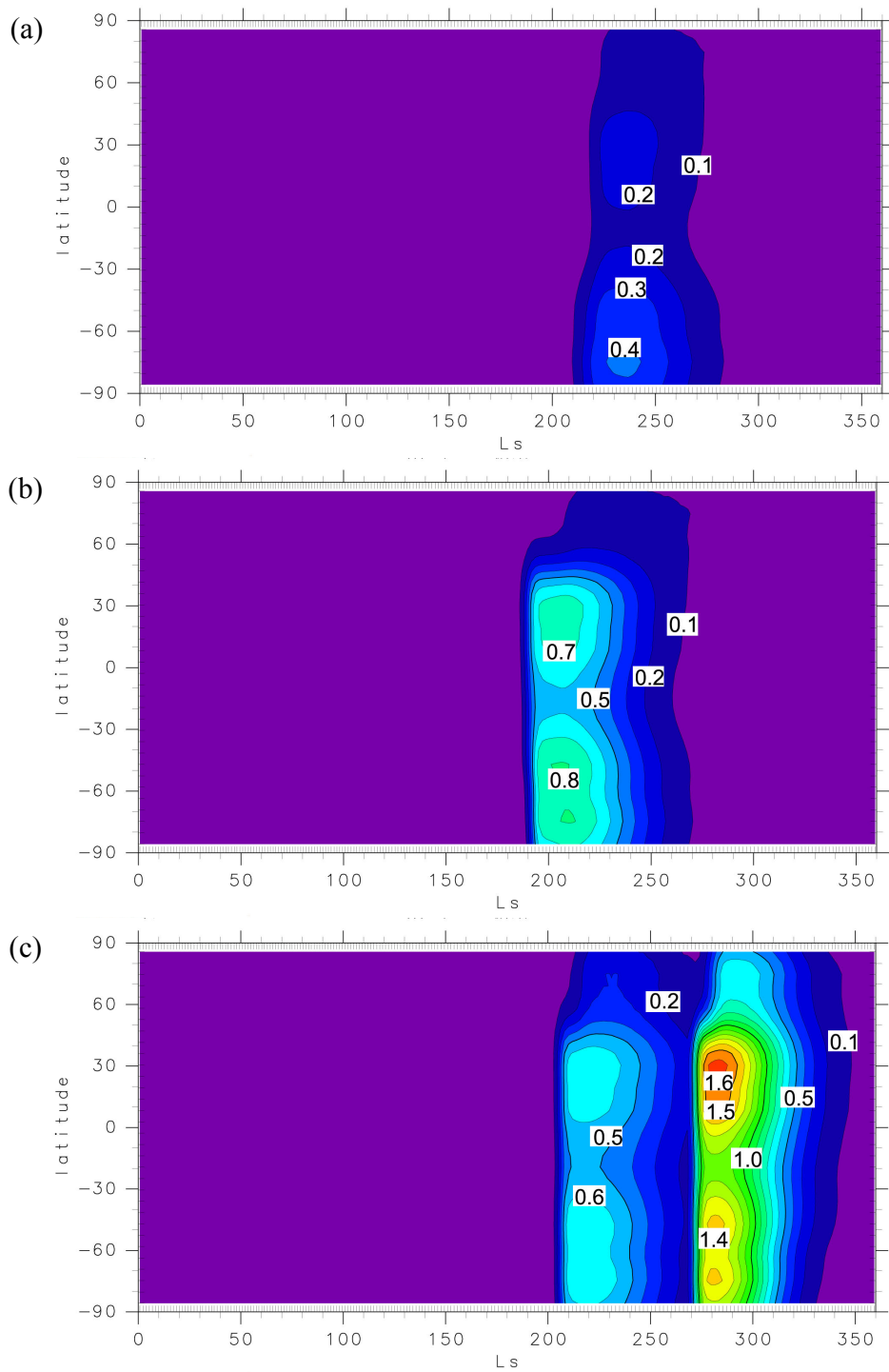


Figure 18: Time-latitude cross-sections of the zonal-mean dust optical depth in infrared wavelengths (9-10 μm) at surface in the (a) TES2, (b) TES3 and (c) VIK1 dust scenarios, respectively.

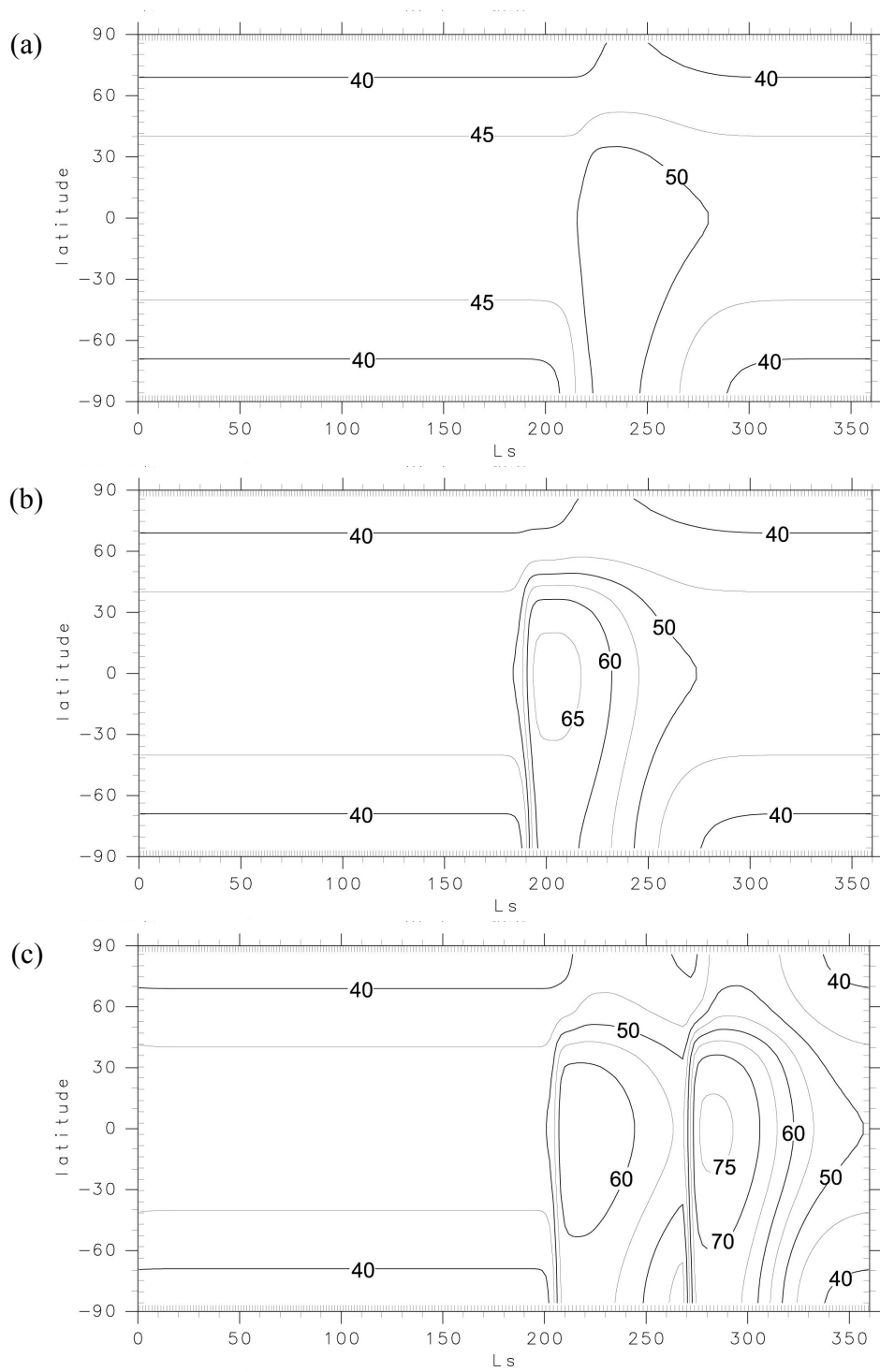


Figure 19: Time-latitude cross-sections of the dust cut-off altitude calculated from (10) in the (a) TES2, (b) TES3 and (c) VIK1 dust scenarios, respectively.

Chapter 3

Sensitivity of the model results to the radiative parameters

3.1 Basic features of the model results in the ‘weak-dust’ case

3.1.1 Daytime temperature and heating/cooling effects

Figure 20 shows the results of the simulations for the zonal-mean daytime (local time ~ 1400) temperature averaged over $L_s=205^\circ-210^\circ$ (northern autumn). Figure 21 presents the corresponding zonal-mean daytime heating/cooling rates due to CO_2 in solar wavelengths (given by the formula of *Forget et al.* [2003]), CO_2 in infrared wavelengths (longer than $4 \mu\text{m}$), dust in solar wavelengths (shorter than $4 \mu\text{m}$), dust in infrared wavelengths (longer than $4 \mu\text{m}$). The large-scale dynamical effects (sum of adiabatic and advective effects), and the small-scale dynamical effects (the sum of the vertical diffusion and dry convective adjustment) are plotted in Figure 21 as well. The TES2 dust scenario (hereafter called the ‘weak-dust’ case, global-mean visible dust opacity of ~ 0.2 in this season), ‘Refractive A’ and ‘PSD 1’ set of dust parameters were employed in these simulations. The comparison of the simulated temperature (Figure 20) with the observations by MGS-TES (Figure 4a and 4b) reveals three main discrepancies. First, the model temperature over the northern polar region is ~ 20 K higher. Similar warmer polar temperature is also present in the results of LMD/AOPP Martian GCM [*Forget et al.*, 2001]. The radiometric calibration of the TES instrument may cause errors of more than 5 K in the cold polar regions [*Conrath et al.* 2000]. In addition, there may be the effects of the simulated surface temperature that prevent cooling of the polar regions, when the daylight time gets shorter. The second difference between the simulations and the MGS-

TES measurements is that the model temperature at lower altitudes (below ~ 1 mb) above the south pole is ~ 10 K higher. This may be due to the effects of the relatively strong dust heating (Figure 21c). The third difference is that the model temperature above ~ 0.5 mb is overall lower than the observations. This might be because of the lack of a gravity wave drag parameterization, as indicated by *Forget et al.* [1999]. Except for these points, the temperature distributions show an overall agreement between the simulation and the observations.

As an advantage of the study using a GCM, we can check the radiative, dynamical and parameterized components of the heating to determine how they affect the temperature fields (Figure 21). As seen from this figure, dust heating in solar wavelengths, CO₂ heating in solar wavelengths, and dynamical heating are dominant in most parts of the domain at 0.3-3 mb, most parts above the altitude of ~ 0.3 mb, and above ~ 0.05 mb in tropics and over the north pole, respectively. Near the surface, CO₂ radiation in infrared wavelengths (longer than 4 μm) has a strong heating effect at tropics, subtropics and midlatitudes (see Figure 21b). This effect is due to the absorption of the fluxes coming from the surface, and is known as the ‘greenhouse’ effect. This strong heating is compensated by the vertical diffusion and dry convective adjustment to transport the excessive heat up to ~ 3 mb (see Figure 21f).

3.1.2 Nighttime temperature and heating/cooling effects

Figure 22 shows the results of the simulations for the zonal-mean nighttime (local time ~ 0200) temperature averaged over $L_s=205^\circ$ - 210° (northern autumn). Figure 23 displays the corresponding zonal-mean nighttime heating/cooling rates due to CO₂ in infrared wavelengths, dust in infrared wavelengths, dynamical effects, and the sum of the vertical diffusion and dry convective adjustment. The radiative effects in solar wavelengths are virtually zero, except in the southern polar region where the sun illuminates atmosphere all day round. Figure 24 shows the MGS-TES observational nighttime temperature, for comparison with Figure 22. The temperature distributions show an overall agreement between in the simulation and the observations, except for the three main discrepancies, which are the same as for the daytime. At this time, cooling by CO₂ becomes the strongest near the surface at tropics, subtropics and midlatitudes (see

Figure 23c). Cooling by dust is very weak in comparison with the CO₂ cooling (see Figure 23b).

3.1.3 Sensitivity to the CO₂ infrared band

Unlike in all other Martian GCMs, the CO₂ 4.3 μm and 10 μm infrared bands are taken into account in this model. Here the effects of the CO₂, including the sensitivity to the 4.3 μm band, are presented.

Figures 25 and 26 show the temperature and CO₂ heating/cooling rate in infrared wavelengths during daytime and nighttime, respectively, with the 4.3 μm infrared band excluded. In comparison with the results with the 4.3 μm infrared band included (Figures 20, 21b, 22 and 23a), the lower temperature over the north pole gets slightly higher, and the temperature difference between days and nights is slightly smaller. Generally, the model response to this band is very small. Virtually no sensitivity is seen to the CO₂ 10 μm infrared band in the zonal mean fields.

If all the CO₂ infrared radiative effects are excluded, the zonal mean temperature near the surface becomes ~20 K higher in daytime, and virtually no difference is seen in temperature between days and nights. This means that the CO₂ nighttime emission exceeds the daytime ‘greenhouse’ effect (which affects the heating below ~3 mb height) when averaged daily. Detailed explanation about this feature is given in Appendix D.

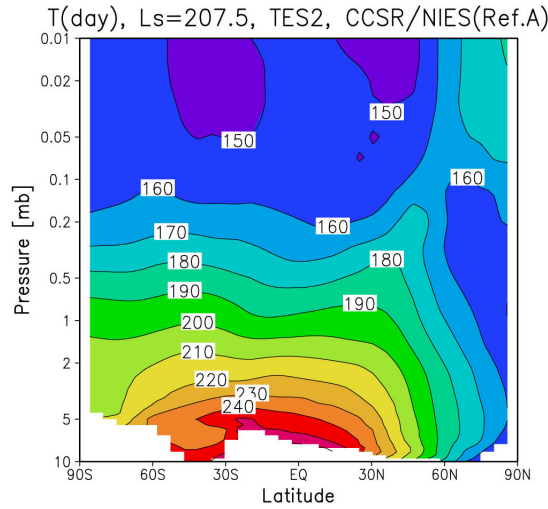


Figure 20: Zonal-mean daytime (local time ~ 1400) model results of temperature [K] averaged over $L_s=205^\circ$ - 210° , using the TES2 dust scenario, ‘Refractive A’ and ‘PSD 1’.

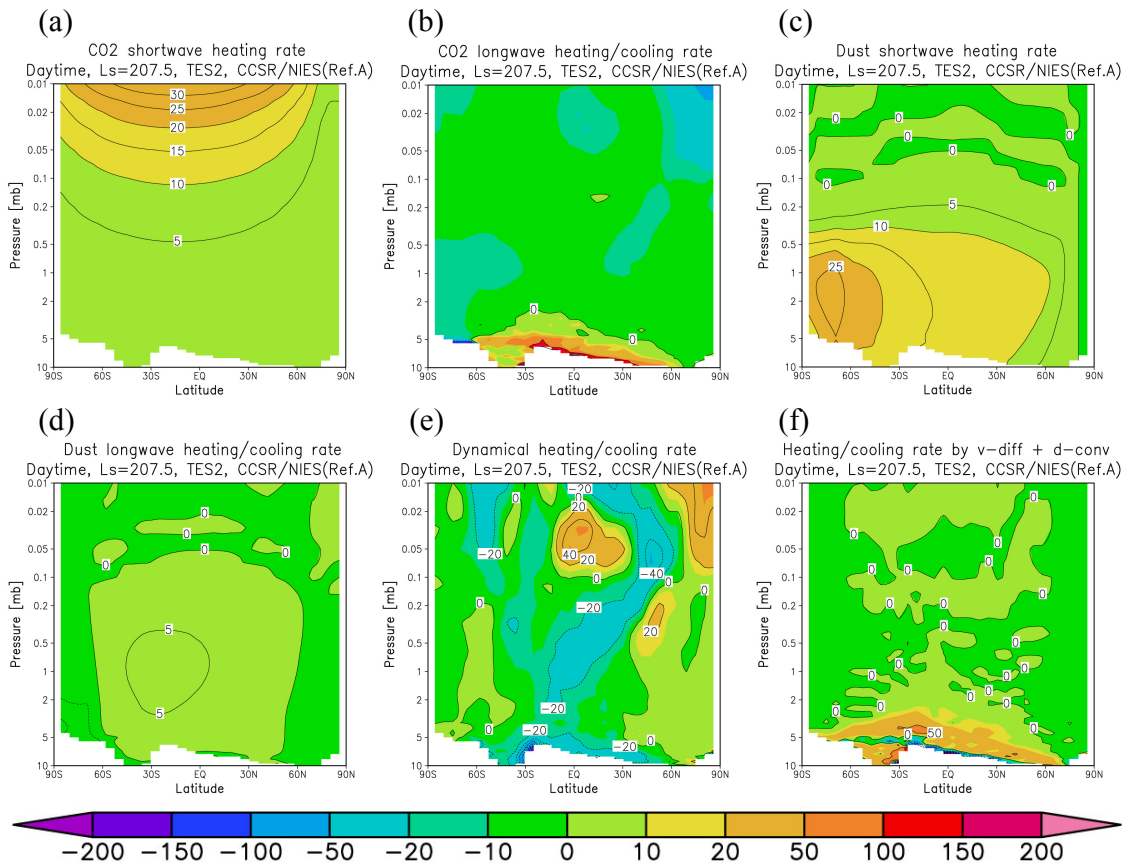


Figure 21: Zonal-mean daytime (local time ~ 1400) heating/cooling rates [K Sol^{-1}] averaged over $L_s=205^\circ$ - 210° , using the TES2 dust scenario, ‘Refractive A’ and ‘PSD 1’: (a) due to CO_2 in solar wavelengths, (b) due to CO_2 in infrared wavelengths, (c) due to dust in solar wavelengths, (d) due to dust in infrared wavelengths, (e) due to the dynamical (sum of adiabatic and advective) effects and (f) due to the sum of the vertical diffusion and dry convective adjustment.

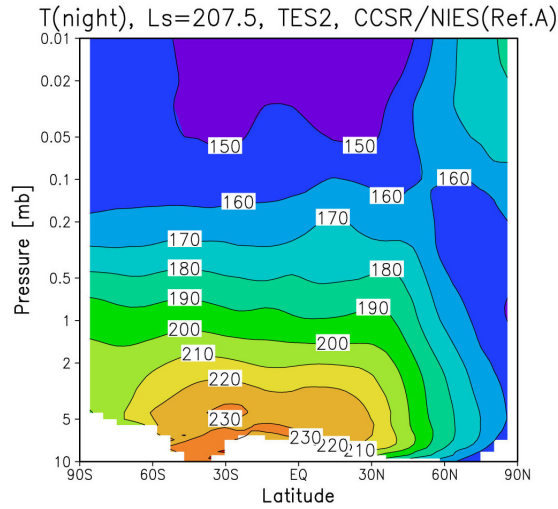


Figure 22: Same as Figure 20, except zonal-mean nighttime (local time ~ 0200) temperature.

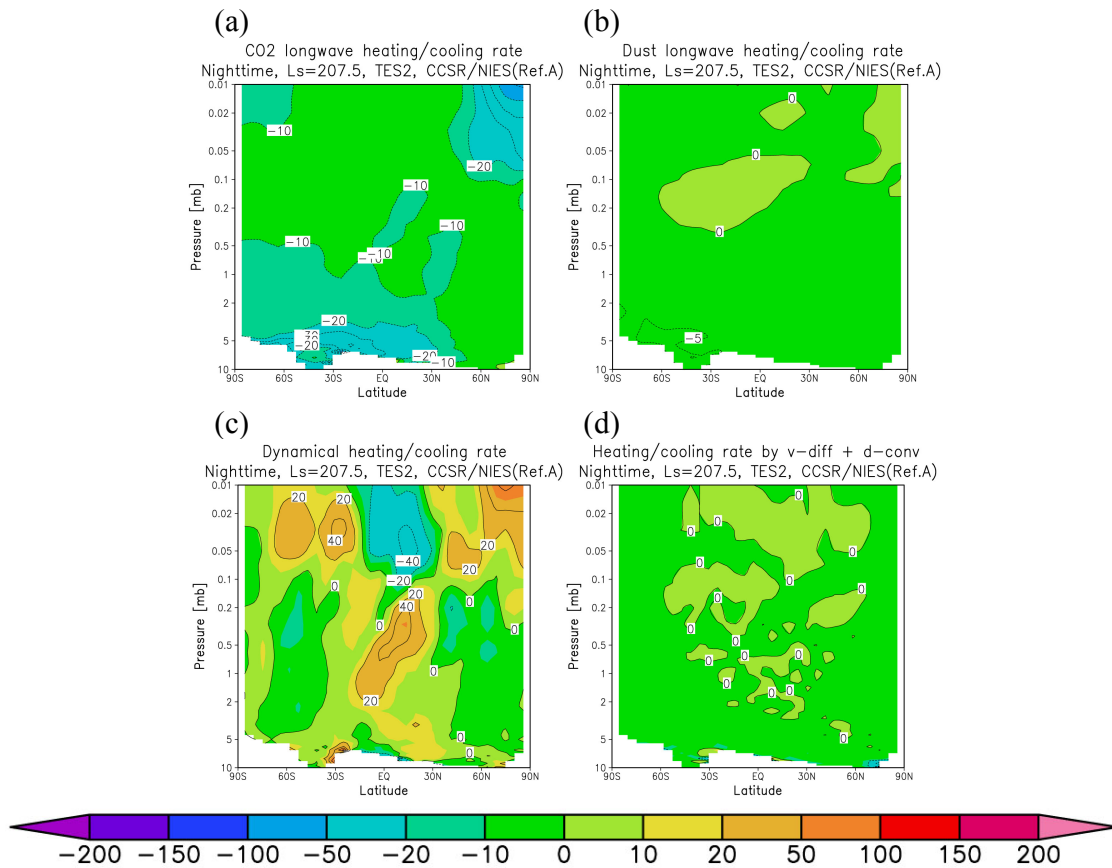


Figure 23: Zonal-mean nighttime (local time ~ 0200) heating/cooling rates [K Sol^{-1}] averaged over $L_s=205^\circ\text{-}210^\circ$, using the TES2 dust scenario, 'Refractive A' and 'PSD 1': (a) due to CO_2 in infrared wavelengths, (b) due to dust in infrared wavelengths, (c) due to the dynamical (sum of adiabatic and advective) effects and (d) due to the sum of the vertical diffusion and dry convective adjustment.

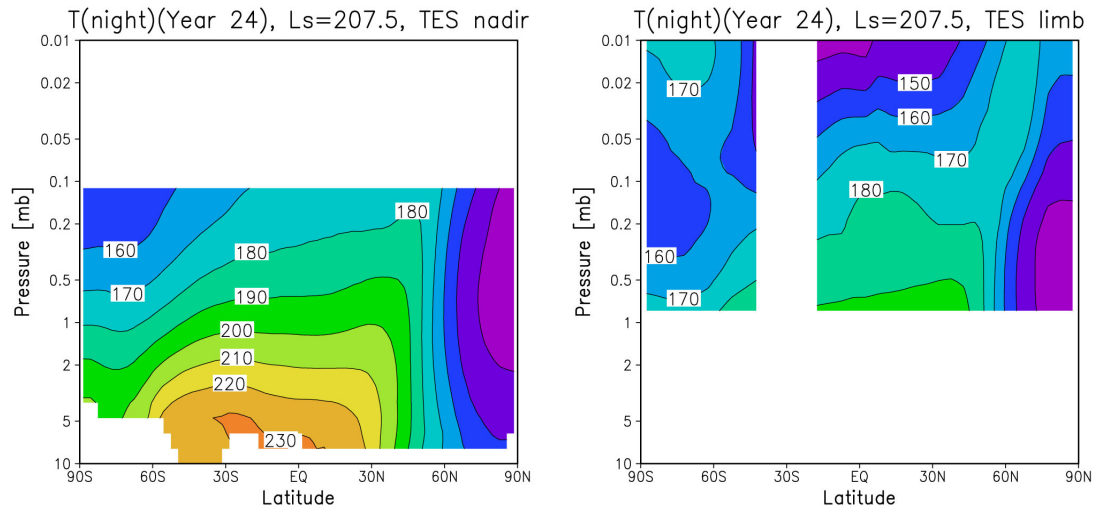


Figure 24: Same as Figure 4a and 4b, except for the zonal-mean nighttime (local time ~0200) temperature.

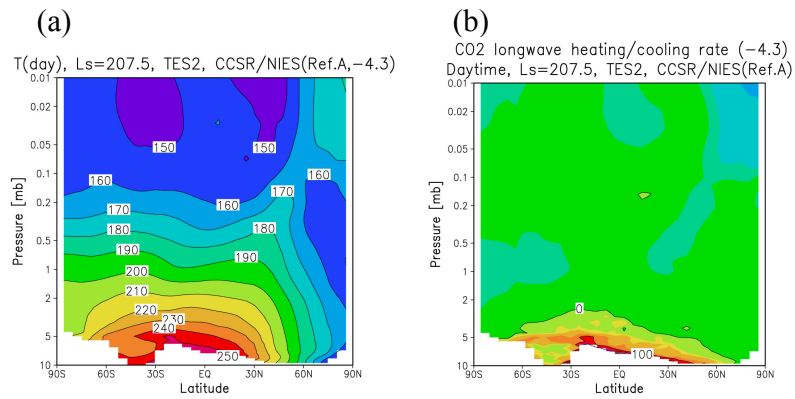


Figure 25: Same as (a) Figure 20 and (b) Figure 21b, respectively, except with the CO₂ 4.3 μ m infrared band excluded.

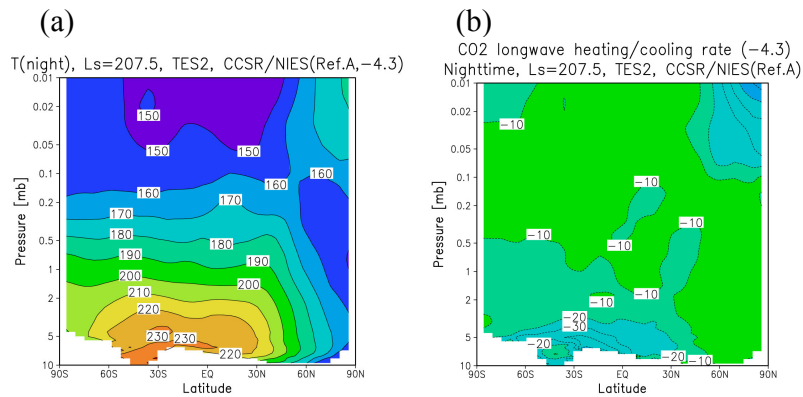


Figure 26: Same as (a) Figure 22 and (b) Figure 23a, respectively, except with the CO₂ 4.3 μ m infrared band excluded.

3.2 Basic features of the model results in the ‘strong-dust’ case

3.2.1 Daytime temperature and heating/cooling effects

Figures 27 and 28 show the same plots as Figures 20 and 21, but with the TES3 dust scenario (hereafter called the ‘strong-dust’ case, global-mean visible dust opacity of ~ 2.2 during a planet-encircling dust storm) using ‘Refractive A’ and ‘PSD 1’. The simulated temperature is about 10-20 K higher than in the MGS-TES observations (Figure 4c and 4d) below the altitude of ~ 0.2 mb. The dust heating rates in solar wavelengths become 8-10 times larger than in the ‘weak-dust’ case. The cooling by CO₂ and dust in infrared wavelengths and the dynamical cooling become larger accordingly, and the ‘greenhouse’ effect near the surface becomes weaker.

3.2.2 Nighttime temperature and heating/cooling effects

Figures 29 and 30 show the same plots as Figures 22 and 23, but for the ‘strong-dust’ case. As well as in daytime, the simulated temperature is about 10-20 K higher than in the MGS-TES observations (Figure 31) below the altitude of ~ 0.2 mb in north of southern midlatitude. At the height of 0.1-1 mb above the south pole, the simulated temperature is ~ 40 K higher. Stronger cooling by CO₂ and dust and stronger dynamical heating than the ‘weak-dust’ case makes the heat balance. Effects by the vertical diffusion and dry convective adjustment are small, as well as for the ‘weak-dust’ case.

3.2.3 Sensitivity to the CO₂ infrared band

Figures 32 and 33 show the same plots as Figures 25 and 26, but for the ‘strong-dust’ case. In this case, the cooling by CO₂ (Figures 32b and 33b) becomes weaker in less than ~ 10 K Sol⁻¹ by excluding the 4.3 μm band, in comparison with Figures 28b and 30a. But the difference of temperature is not seen (Figures 32a and 33a, in comparison with Figures 27 and 29), because the difference of CO₂ cooling by excluding the 4.3 μm band is very small in comparison with the heating/cooling effects by the CO₂ 15 μm band and dust. Virtually no sensitivity is seen to the CO₂ 10 μm infrared band in the zonal-mean fields, as well as in the ‘weak-dust’ case.

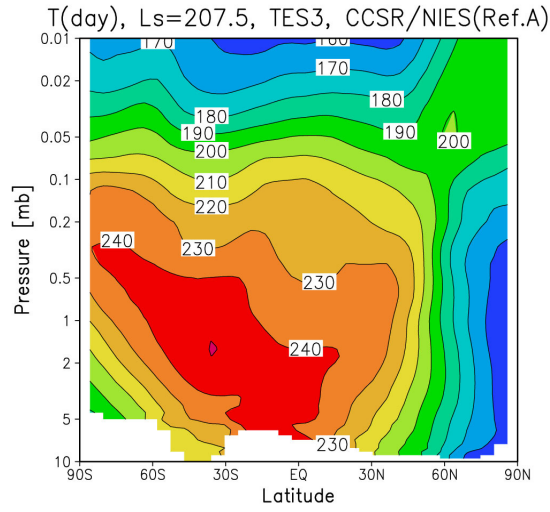


Figure 27: Same as Figure 20, except using the TES3 dust scenario.

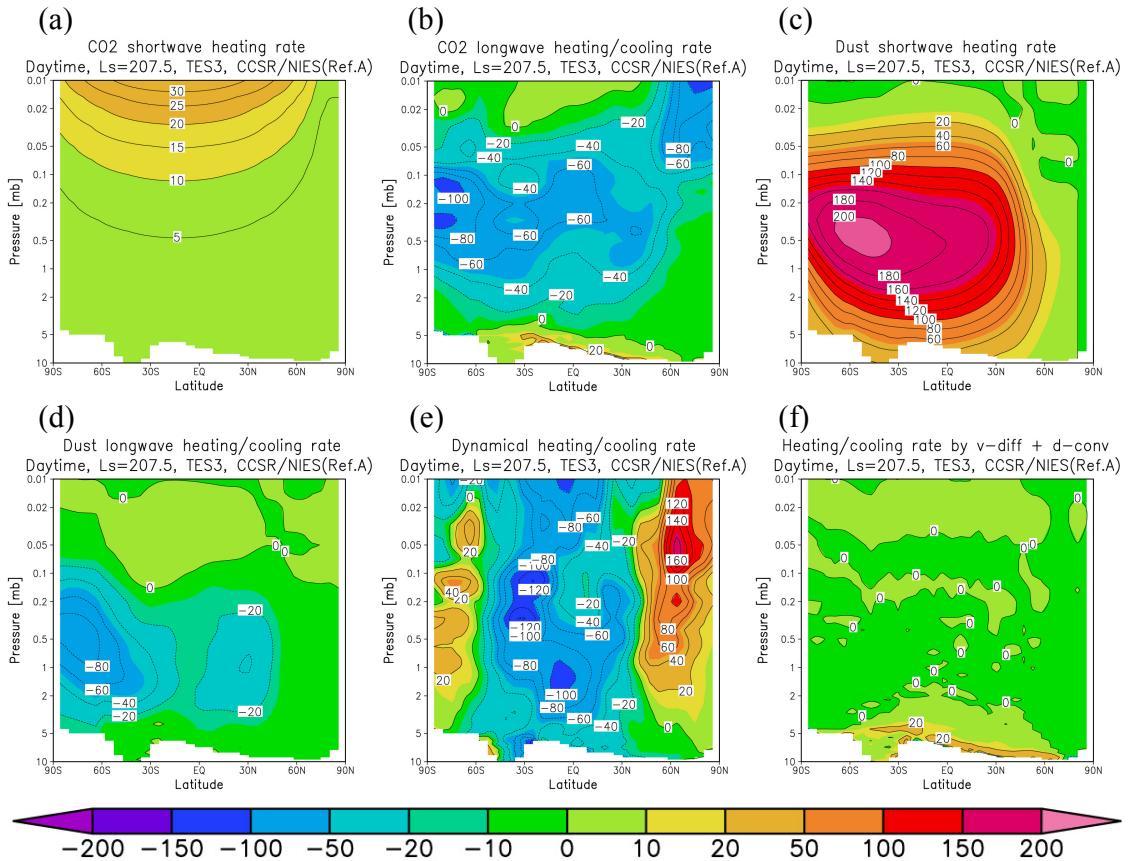


Figure 28: Same as Figure 21, except using the TES3 dust scenario.

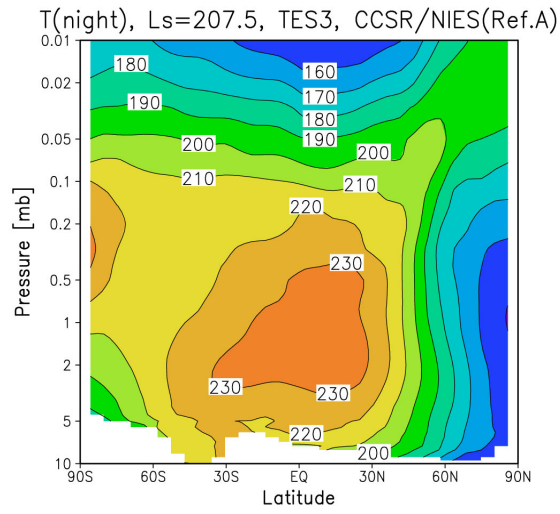


Figure 29: Same as Figure 22, except using the TES3 dust scenario.

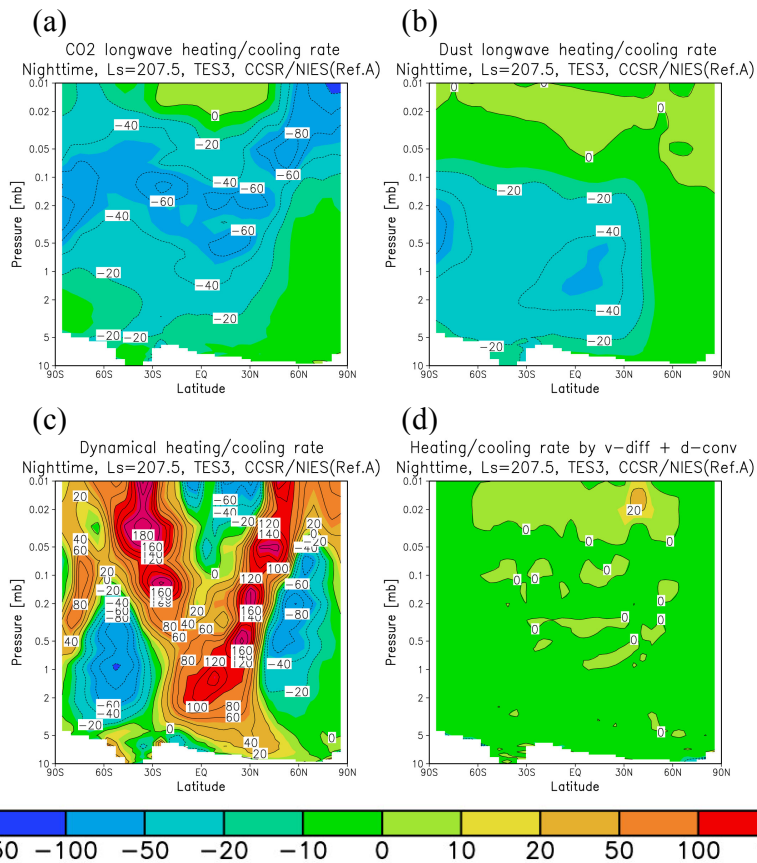


Figure 30: Same as Figure 23, except using the TES3 dust scenario.

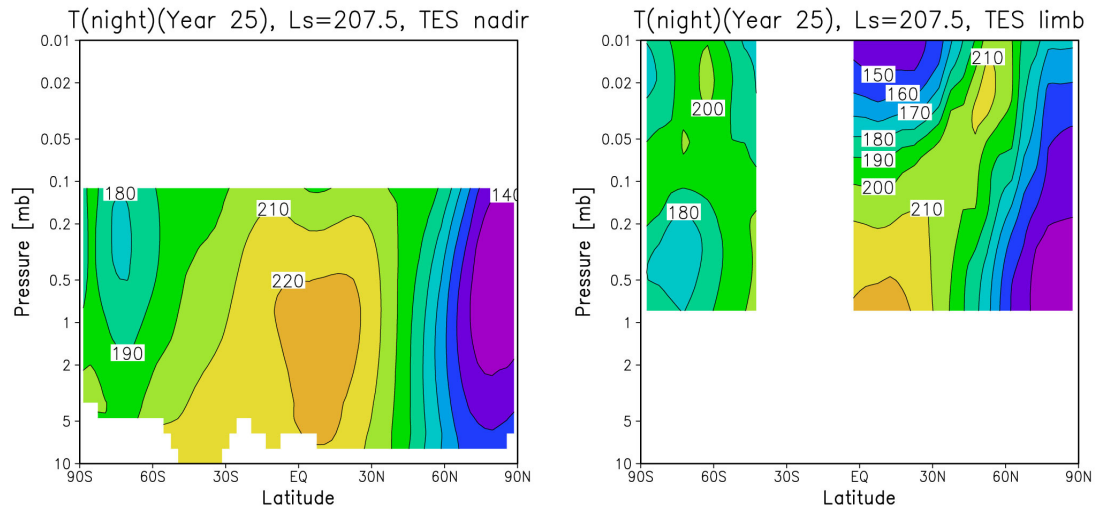


Figure 31: Same as Figure 4c and 4d, except for the zonal-mean nighttime (local time ~0200) temperature.

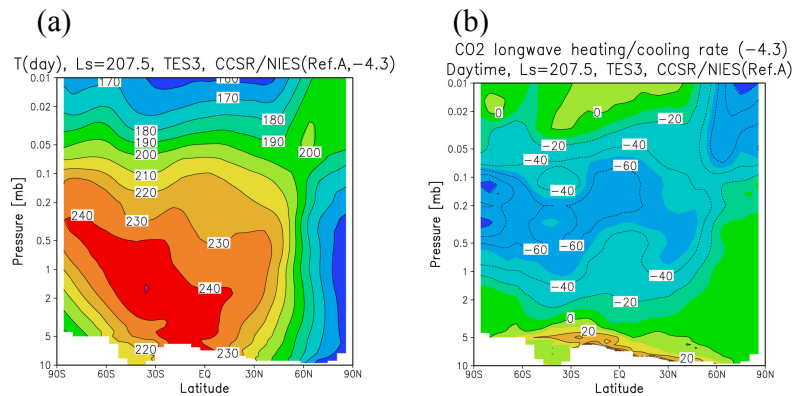


Figure 32: Same as Figure 25, except using the TES3 dust scenario.

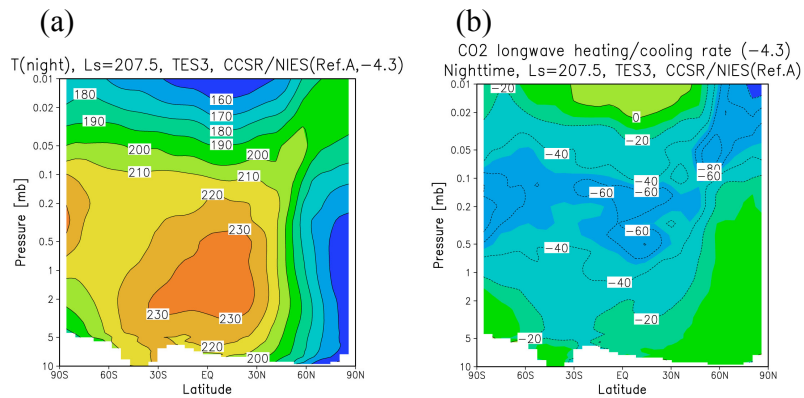


Figure 33: Same as Figure 26, except using the TES3 dust scenario.

As above, the CO₂ 15 μm band is dominant in the CO₂ infrared radiative effects, and there is little sensitivity of the zonal-mean temperature fields to the CO₂ 4.3 μm and 10 μm infrared bands in both the ‘weak-dust’ and ‘strong-dust’ cases.

3.3 Sensitivity to the dust parameters

The radiative effects of dust depend on the dust parameters (refractive index and particle size distribution), as described in Section 1.2 and Appendix A. As seen in Section 3.2, the simulations using the parameters ‘Refractive A’ and ‘PSD 1’ produce higher temperature below ~0.1 mb than the MGS-TES observations in both daytime and nighttime. To modify the dust heating (which seems to be rather strong in this case) and correct the temperature fields to fit the observations, sensitivity tests to the particle size distribution and refractive indices are performed.

3.3.1 Sensitivity to the particle size distribution

The particle size distribution of dust affects the ratio of dust opacity between for solar wavelengths and infrared wavelengths, as written in Subsection 1.2.2. The dust radiation scheme used in this model gives the visible-to-infrared ratio of the dust opacity (the opacity at 0.435-0.678 μm band divided by the one at 8.5-10.2 μm band) as 3.70, if ‘Refractive A’ and ‘PSD 1’ are used. If the particle size of dust becomes larger, the ratio gets smaller, and weaker heating in solar wavelengths and stronger cooling in infrared wavelengths are expected. The visible-to-infrared ratios of dust opacities in ‘PSD 2’ and ‘PSD 3’ are 2.56 and 2.00, respectively, if ‘Refractive A’ is used for calculation. These values are close to the observed values of the ratio, between 2 and 2.5 [*Martin, 1986; Clancy et al., 1995*].

Figures 34 and 35 show the daytime dust heating rate in solar wavelengths, and temperature, respectively, with different particle size distributions and the ‘Refractive A’. Figure 34 demonstrates that the smaller the visible-to-infrared ratio of dust opacities gets, the smaller the dust heating rate in solar wavelengths becomes. The maximum dust heating rate at the height of ~0.5 mb becomes ~20 % smaller with ‘PSD 3’ than with

‘PSD 1’. Meanwhile, it becomes $\sim 30\%$ larger near the surface at the equator. As for the temperature, Figure 35 shows that the smaller the visible-to-infrared ratio of dust opacities becomes, the lower the temperature at the height of 0.1-1 mb becomes. Above the south pole, it is ~ 10 K smaller with ‘PSD 3’ than with ‘PSD 1’. Meanwhile, the temperature near the surface at the equator becomes ~ 10 K higher for smaller visible-to-infrared ratio. This seems to be because when the dust opacity in visible wavelengths becomes smaller, the sunlight more easily penetrates into the lower atmosphere where it subsequently produces heating.

The simulated temperature with ‘PSD 3’ is closer to the MGS-TES observations (Figure 4c and 4d) than with ‘PSD 1’ in the altitude on 0.1-1 mb, but the temperature with ‘PSD 1’ is closer to the observations than with ‘PSD 3’ below the altitude of ~ 4 mb. We cannot determine which particle size distribution should be appropriate from only these results.

3.3.2 Sensitivity to the refractive indices

‘Refractive A’ has larger values of imaginary refractive index than ‘Refractive B’ in ultraviolet and visible wavelengths, which means that ‘Refractive A’ should produce stronger solar heating, as described in Subsection 1.2.3. By decreasing the values or replacing to ‘Refractive B’, the decrease of solar heating and lower temperature fields are expected to be produced.

Figures 36 and 37 present the daytime dust heating rates in solar wavelengths and temperature, respectively, simulated with the different refractive indices profiles and ‘PSD 1’. The comparison between the simulations with ‘Refractive A’ and ‘Refractive A-prime’ shows that the decrease of imaginary parts of the refractive index in solar wavelengths contributes to the decrease of the dust heating rates by $\sim 30\%$ as well as to the decrease of the daytime temperature by ~ 10 K. ‘Refractive B’ results in a slightly higher dust heating rates than in ‘Refractive A-prime’, but the daytime temperature is colder because the effects of cooling in infrared wavelengths with ‘Refractive B’ are stronger than in ‘Refractive A’.

The simulated daytime temperature using ‘Refractive B’ and ‘PSD 1’ shows an overall agreement with the MGS-TES observations (Figure 4c and 4d).

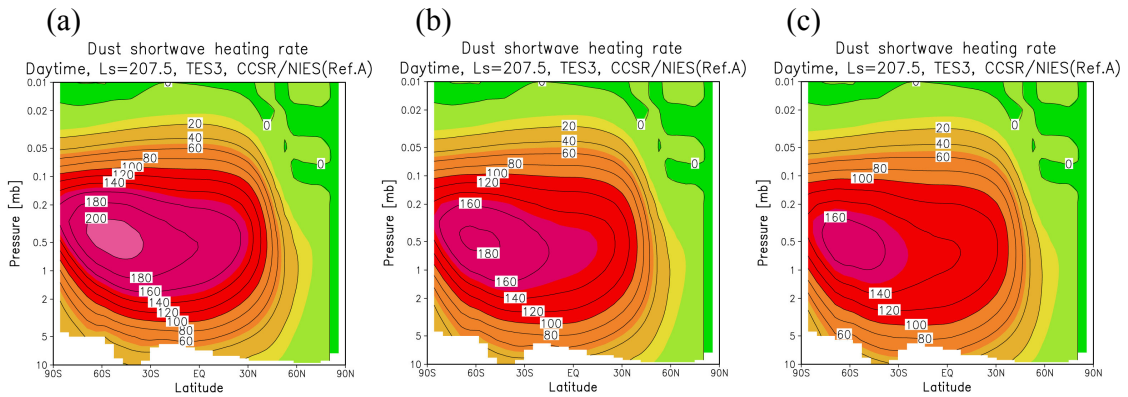


Figure 34: Zonal-mean daytime (local time ~ 1400) dust heating rate [K Sol^{-1}] in solar wavelengths averaged over $L_s=205^\circ-210^\circ$ using the TES3 dust scenario and ‘Refractive A’, with the particle size distribution of (a) ‘PSD 1’, (b) ‘PSD 2’ and (c) ‘PSD 3’ given in Subsection 2.5.2.

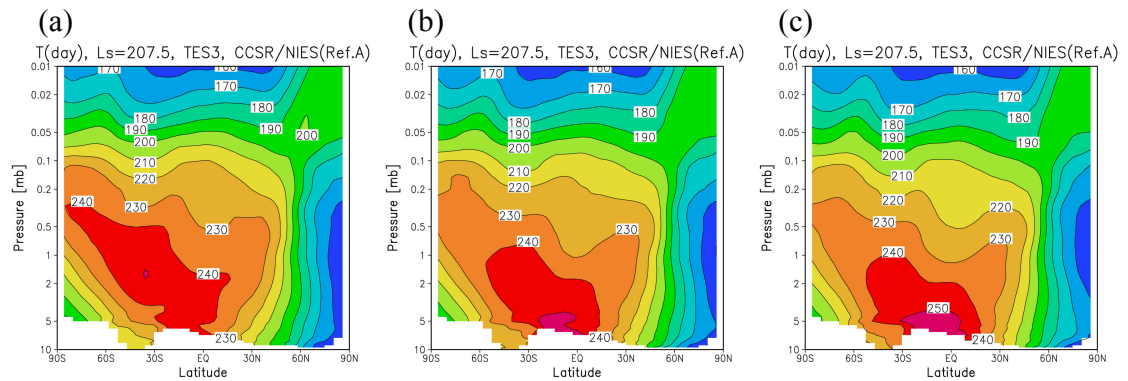


Figure 35: Same as Figure 34, except for the temperature.

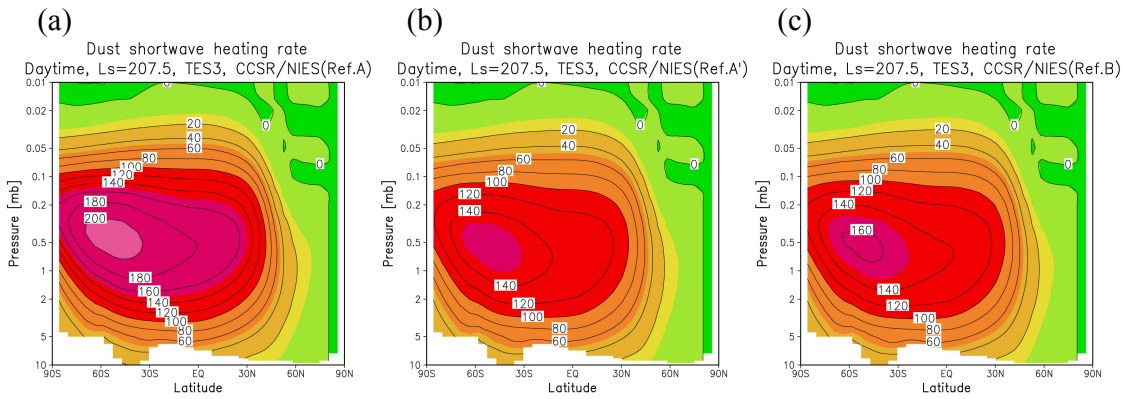


Figure 36: Zonal-mean daytime (local time ~ 1400) dust heating rate [K Sol^{-1}] in solar wavelengths averaged over $L_s=205^\circ$ - 210° using the TES3 dust scenario and ‘PSD 1’, with the refractive indices profile of (a) ‘Refractive A’, (b) ‘Refractive A-prime’ and (c) ‘Refractive B’ given in Subsection 2.5.2.

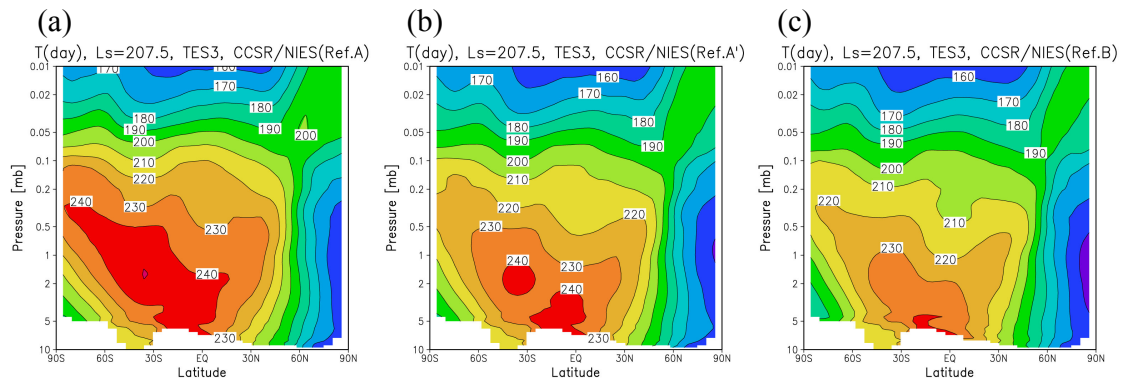


Figure 37: Same as Figure 36, except for the temperature.

3.4 Summary and the accuracy of the simulated temperature for different dust opacities

Figures 38-45 show the same plots as Figures 20-23 and 27-30 averaged over $L_s=205^\circ$ - 210° (northern autumn) using ‘PSD 1’ and ‘Refractive B’. In the ‘weak-dust’ case, the difference of the zonal-mean temperature between ‘Refractive A’ and ‘Refractive B’ is within ~ 10 K in both daytime (see Figures 20 and 38) and nighttime (see Figures 22 and 40). The difference of temperature is the largest near the surface, where daytime dust heating rate in solar wavelengths is ~ 5 K Sol^{-1} smaller with ‘Refractive B’ than with ‘Refractive A’. The nighttime cooling rate due to CO_2 near the surface is ~ 5 K Sol^{-1} smaller with ‘Refractive B’ than with ‘Refractive A’, owing to a little bit colder temperature. The heating/cooling rates due to other components are almost the same for both refractive indices profiles (see Figures 21, 23, 39 and 41).

Meanwhile, in the ‘strong-dust’ case, the difference of the temperature simulated with different refractive indices profiles is up to 15-20 K mainly at the altitude of 0.1-2 mb, in both daytime (see Figures 27 and 42) and nighttime (see Figures 29 and 44). As well as ~ 30 % decrease of daytime dust heating rate in solar wavelengths, as seen in Subsection 3.3.2, CO_2 cooling rate in both daytime and nighttime decreases in ~ 30 % in ‘Refractive B’, owing to the colder temperature (see Figures 28, 30, 43 and 45). With ‘Refractive B’ the simulated temperature fields show an overall agreement with the MGS-TES observations (see Figures 4c, 4d and 31), though nighttime temperature at the height of 0.1-1 mb above the south pole is still ~ 30 K higher. At present, the observational data for the dust opacity by MGS-TES can be obtained only for daytime, and the daily variance of the opacity is still not known from the observations. It can be expected that the nighttime dust opacity is smaller than the daytime, because the calculation of the surface wind stress shows that the value tends to exceed the threshold value needed for lifting only in daytime [Newman *et al.*, 2002a]. Therefore, the daily variance of the dust opacity might be needed to take into account for the accurate simulation in a future work.

Figure 46 shows the difference in the simulated daytime temperature between the ‘strong-dust’ and ‘weak-dust’ cases using ‘Refractive A’ and ‘Refractive B’. With ‘Refractive B’, the maximum difference is 10-15 K smaller than with ‘Refractive A’ above the equator and south pole, but 10-15 K higher than in the observations (Figure 5)

above the equator. Figure 47 shows the comparison of temperature at the equator between the model and the observations in the ‘weak-dust’ case, and shows that the simulated temperature at 0.03-1 mb is colder than in the observations by up to 15-20 K for both day and night, with both ‘Refractive A’ and ‘Refractive B’. If the dust opacity is increased by a factor of two, the simulated temperature improves to some extent, but there are still 10-15 K discrepancies. In the ‘weak-dust’ case, the sensitivity of the temperature to the particle size distribution is weak, within ~ 2 K at all heights for all three profiles introduced in Subsection 2.5.2. Therefore, these discrepancies are not due to the dust radiation scheme, but due to the CO₂ radiation scheme, due to a lack of the subgrid-scale dynamics effects, or due to both of them. This should be improved in the future.

Figure 48 shows the comparison of the temperature at the equator between the model and the observations in the ‘strong-dust’ case. From this figure, the simulation with ‘Refractive B’ shows an overall agreement with the observations, except at the heights of 0.2-2 mb at daytime, where the maximum is colder by ~ 15 K. In the simulation with 1.5 times of the dust thickness, the temperature in this region improves, but above ~ 0.2 mb, the temperature becomes higher compared to the observations both for day and night. The sensitivity to the particle size distribution in the ‘strong-dust’ case is presented in Figure 49. It shows that ‘PSD 1’ produces the overall closest agreement for both day and night, although the difference between the distributions is small (within ~ 7 K except near the surface in daytime). Therefore, the combination of ‘PSD 1’ and ‘Refractive B’ is apparently the best-fit dust parameters up to now.

In Chapter 4, the dust parameters ‘PSD 1’ and ‘Refractive B’ are used for the model simulations. The combination of these parameters produces closer to the observational result daytime temperature cross-section than other combinations tested in this chapter. It also produces an acceptable nighttime temperature cross-section during a planet-encircling dust storm when the sensitivity to the dust parameter is strong. Although there are still some deviations from the observations that could not be improved enough in this chapter, a good agreement is seen for the meridional temperature gradient in the northern hemisphere. Therefore, using this model, the zonal-mean wind fields of a good accuracy to observations are expected to be produced, and realistic baroclinic waves are expected to be reproduced.

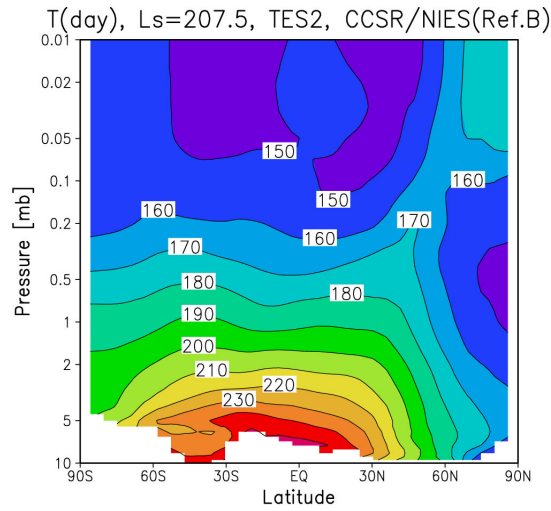


Figure 38: Same as Figure 20, except using ‘Refractive B’.

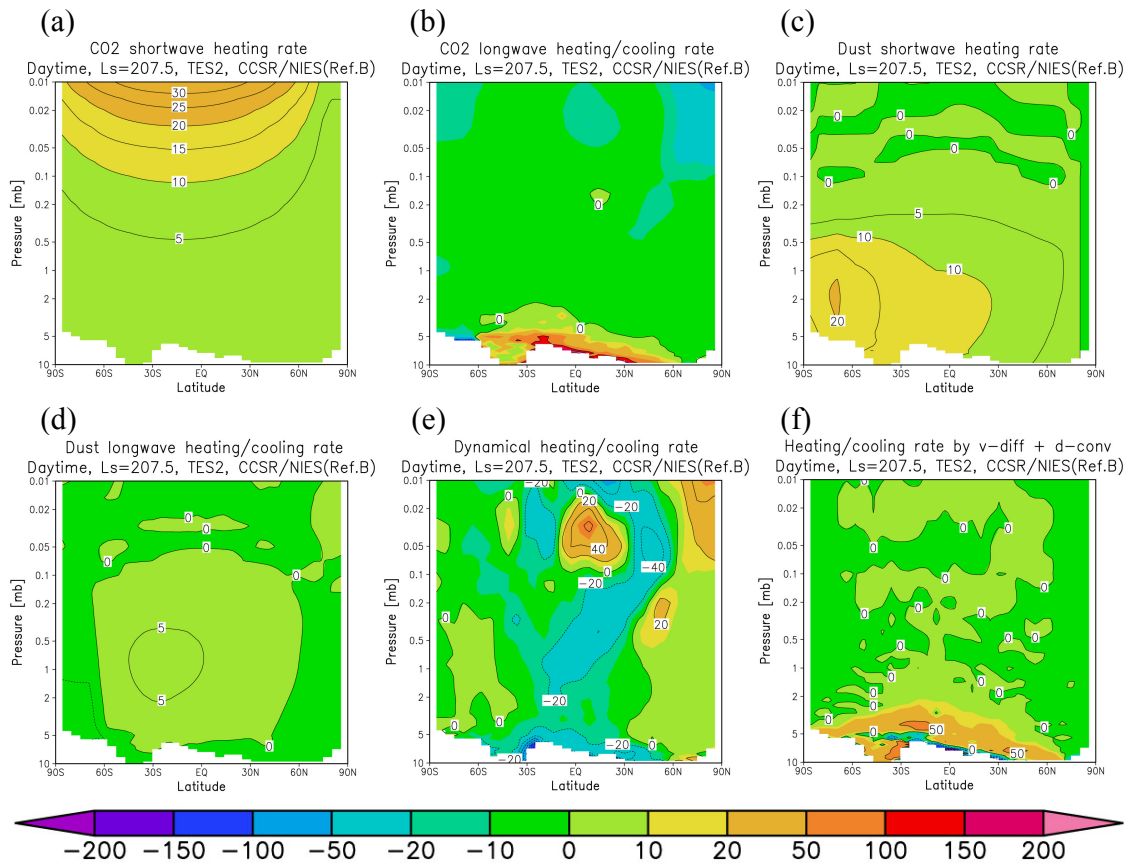


Figure 39: Same as Figure 21, except using ‘Refractive B’.

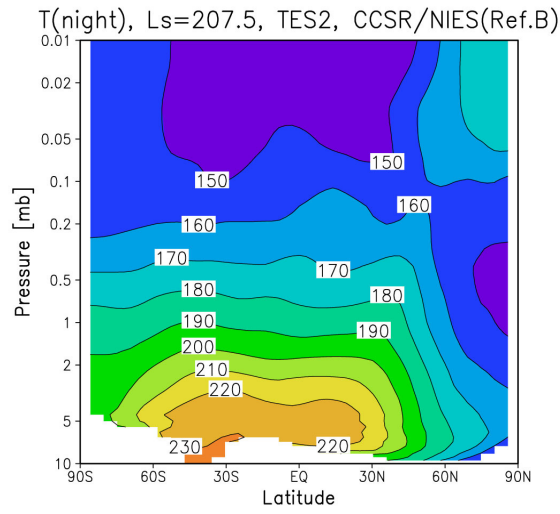


Figure 40: Same as Figure 22, except using 'Refractive B'.

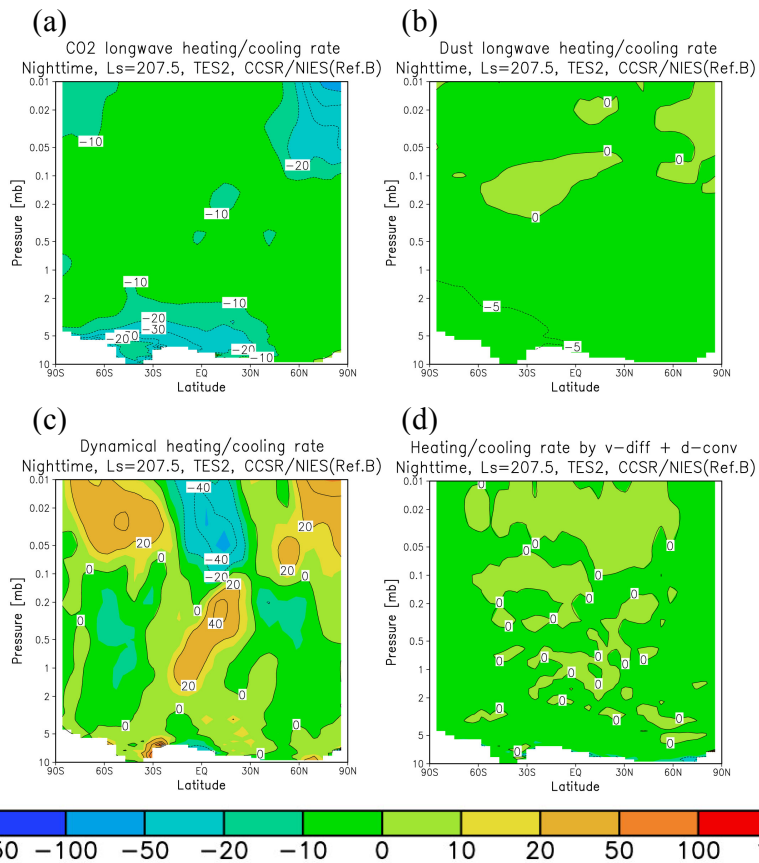


Figure 41: Same as Figure 23, except using 'Refractive B'.

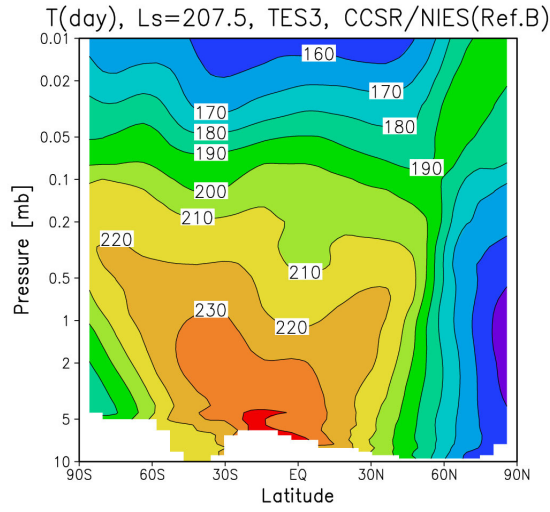


Figure 42: Same as Figure 27, except using ‘Refractive B’.

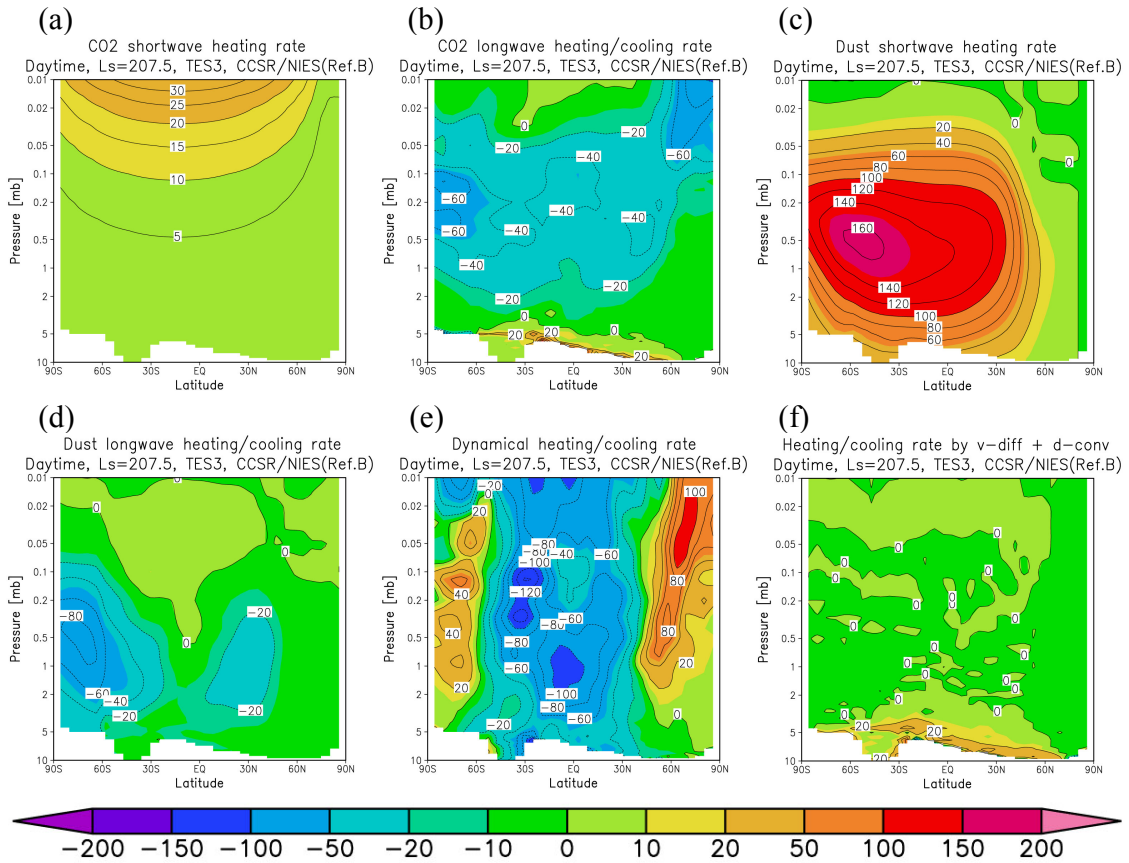


Figure 43: Same as Figure 28, except using ‘Refractive B’.

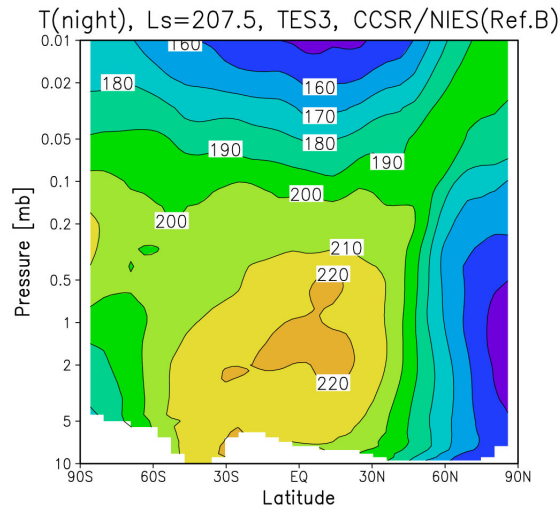


Figure 44: Same as Figure 29, except using 'Refractive B'.

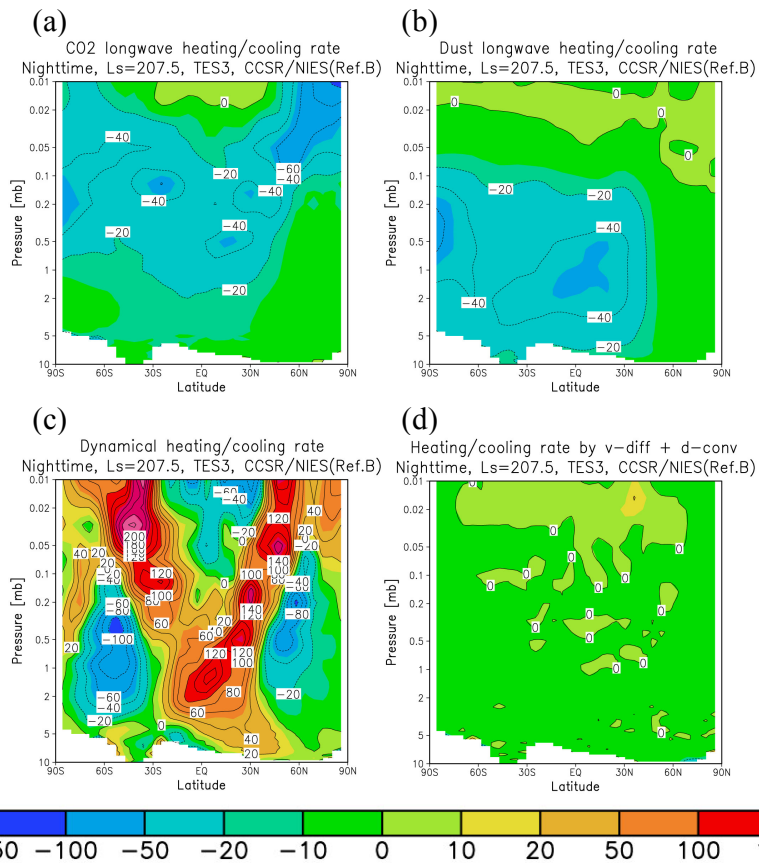


Figure 45: Same as Figure 30, except using 'Refractive B'.

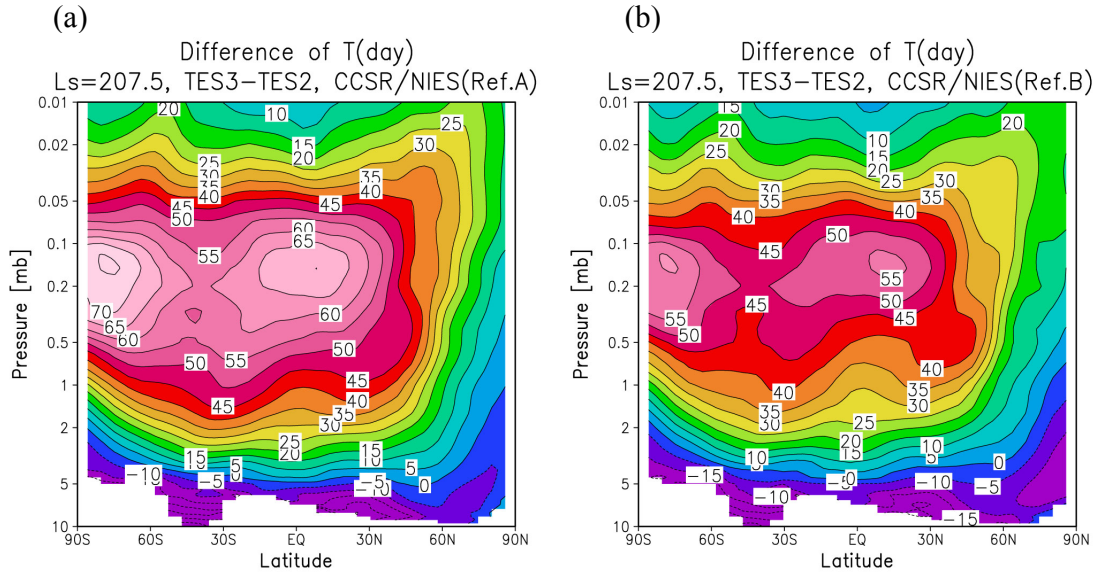


Figure 46: Difference of daytime (local time ~ 1400) temperature [K] between the ‘strong-dust’ (TES3 dust scenario) and ‘weak-dust’ (TES2 dust scenario) cases, averaged over $L_s=205^\circ$ - 210° using ‘PSD 1’: (a) using ‘Refractive A’ and (b) using ‘Refractive B’.

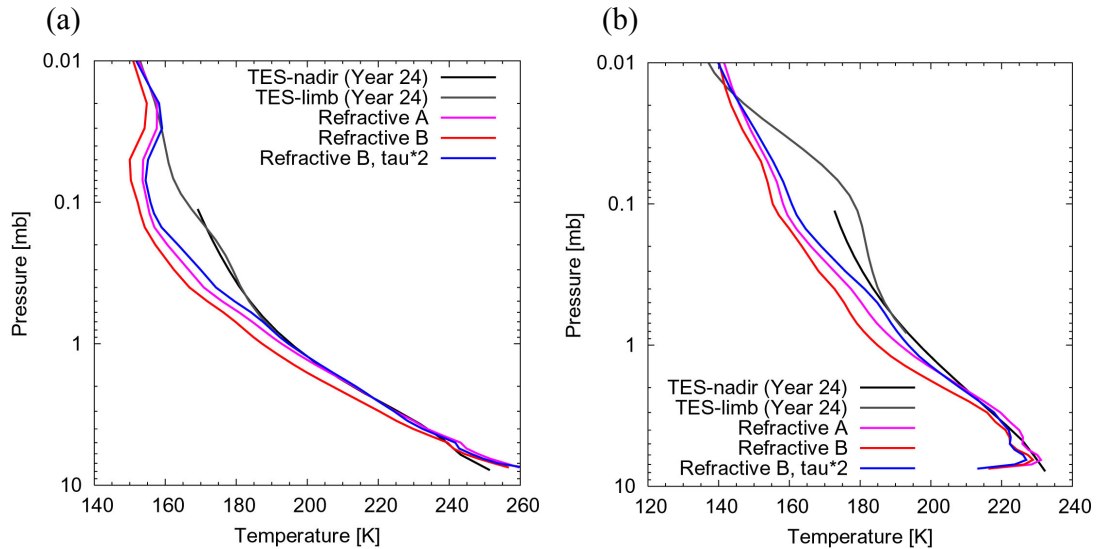


Figure 47: Comparison of the zonal-mean temperature [K] at the equator (between 5° S and 5° N) averaged over $L_s=205^\circ$ - 210° in the ‘weak-dust’ (TES2 dust scenario) case between the MGS-TES observations and model results using different refractive indices profiles: (a) daytime (local time ~ 1400) and (b) nighttime (local time ~ 0200). Blue lines are for the dust thickness of twice of that in the TES2 dust scenario.

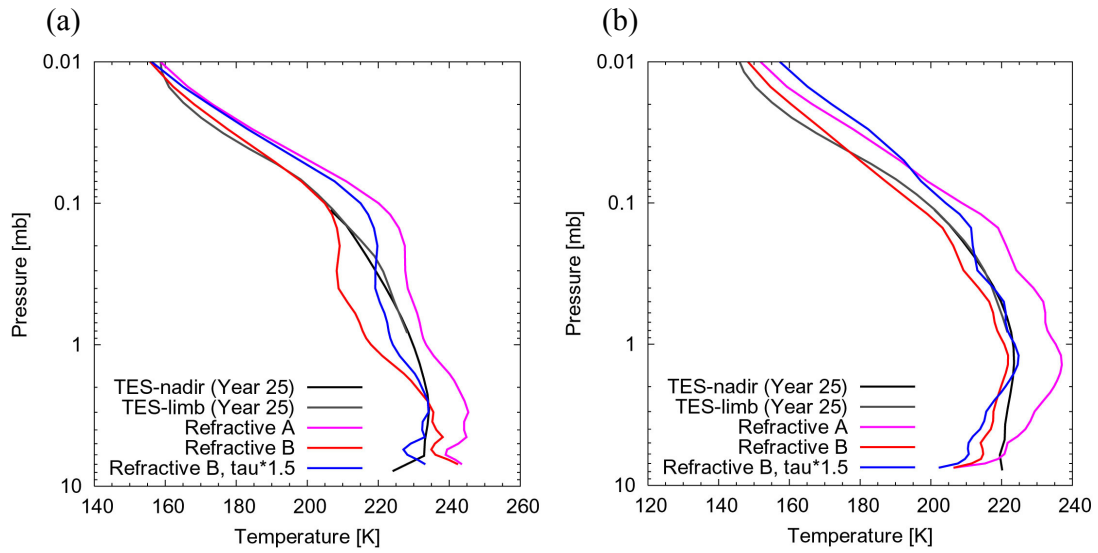


Figure 48: Same as Figure 47, but for the ‘strong-dust’ (TES3 dust scenario) case; blue lines are for the dust thickness of 1.5 times higher than that in the TES3 dust scenario.

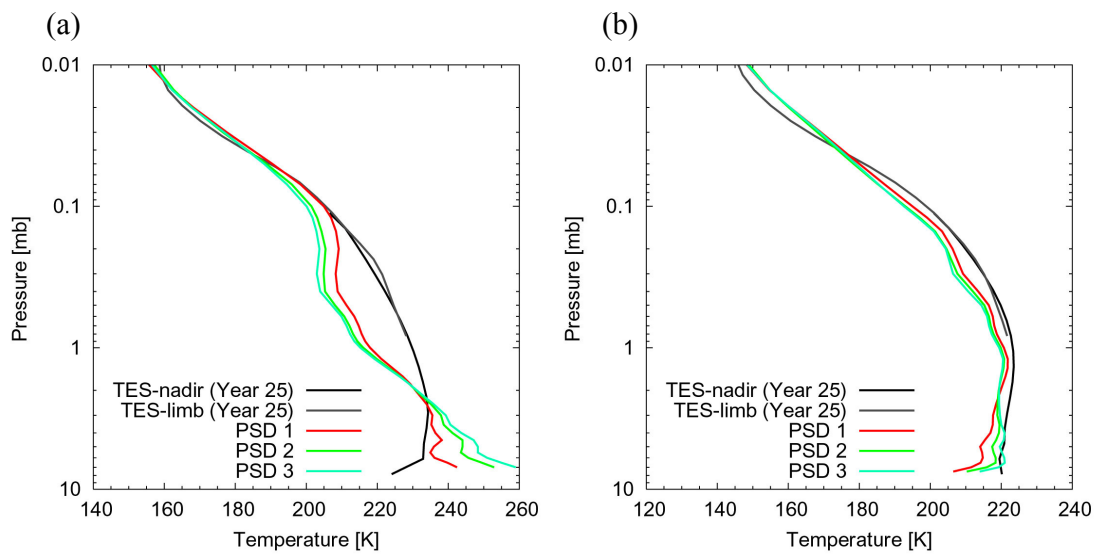


Figure 49: Same as in Figure 47, but the comparison for the particle size distributions using ‘Refractive B’ and the ‘strong-dust’ (TES3 dust scenario) case.

Chapter 4

Baroclinic waves in the Martian atmosphere for different seasons and dust conditions

4.1 Basic features of the simulated waves in ‘autumn’ for the ‘weak-dust’ scenario

4.1.1 Comparison with the Viking Lander 2 observations

Figure 50 presents the annual variations of the daily-averaged surface pressure at the grid point in the Martian GCM nearest to Viking Lander 2 (47° N, 225° W) simulated using the TES2 dust scenario. It is compared with the Viking Lander 2 observations for the same period of time when there was no planet-encircling dust storm (in 1979). It shows an overall agreement between in the model and the observations, especially in summer and autumn, in both the pressure values and the time when the oscillations appear.

Figure 51 presents the spectral decomposition of the surface pressure and the 2-m height temperature at 47° N for $L_s=195^\circ$ - 225° (hereafter ‘autumn’) in the GCM for zonal wavenumbers and periods longer than 1 Sols. As seen from the figure, the spectral component with ~ 3 Sols period and $WN=2$ dominates, and the component with ~ 5 Sols period and $WN=2$ is the second strongest in both the surface pressure and temperature. The ~ 5.5 Sols period and $WN=1$ component is also evident in the surface pressure. Comparison of these results with the spectral analysis of the Viking Lander 2 data for the same season (Figure 52, done by *Barnes* [1981]) reveals that the periods of the dominant harmonics are consistent, while the period of the second largest peak is longer in the

observations of the surface pressure. It is impossible to obtain accurate zonal wavenumbers from the Viking Lander 2 measurements. *Barnes* [1981], who utilized estimates of the geostrophic wind and the cross-isobar angle using the method of *Willebrand* [1978], made rough calculations. According to his analysis, the zonal wavenumber is ~ 2 for the period of ~ 7.2 Sols, and ~ 4 for the period of ~ 2.7 Sols. The wavenumber for the longer period harmonic is consistent with the simulations, but is smaller in the model for the shorter period wave.

4.1.2 Linear estimation of baroclinic growth rates

In order to understand the ability of the baroclinically unstable zonal flow to excite the planetary waves, we performed linear estimations of the baroclinic growth rates for these waves. In these calculations, we used the solutions of the Charney problem under the approximation of the constant vertical wind shear ($\partial\bar{u}/\partial z$), Brunt-Väisälä frequency (N) and scale height (H). Note that this approximation does not fully reproduce the real wave excitation mechanism, but it is useful for a qualitative comparison nevertheless. *Branscome* [1983] described the growth rate σ_i as a function of the wavenumber as follows:

$$\sigma_i = \frac{\pi e^{-2}(\partial\bar{u}/\partial z)f^2 k'(1+\gamma)}{K'^2 N^2 H} \left[1 - \frac{0.26(1+\gamma)f}{K'NH} \right] \quad (11)$$

where

$$\gamma = \frac{\beta N^2 H}{f^2(\partial\bar{u}/\partial z)}, \quad (12)$$

$$K' = \sqrt{k'^2 + l'^2}, \quad (13)$$

$$k' = \frac{k}{a \cos \phi}, \quad (14)$$

$$l' = \frac{l}{a}, \quad (15)$$

f is the Coriolis parameter, $\beta = df/dy$, a is the radius of the planet, ϕ is the latitude, and k and l are the zonal and meridional wavenumbers, respectively. By solving $\partial\sigma_i/\partial k = 0$ from

equation (11), the expressions for the maximum growth rate $\sigma_{i,\max}$ and for the most unstable wavenumber k_{\max} can be written as follows.

$$\sigma_{i,\max} \propto \frac{f}{N} \frac{\partial \bar{u}}{\partial z} \quad (16)$$

$$k_{\max} \propto \frac{(1+\gamma)f}{NH} \quad (17)$$

Formula (16) shows that the maximum growth rate is proportional to the vertical wind shear, and is inversely proportional to the Brunt-Väisälä frequency. Moreover, (17) shows that the larger vertical wind shear generates waves with smaller wavenumbers, and the smaller Brunt-Väisälä frequency tends to excite waves with larger wavenumbers, for $N \sim 0.01$ in this case.

Figure 53 presents the estimates of the growth rate using (11) and the typical values of $\partial \bar{u} / \partial z$, N and H at 47° N in ‘autumn’. This figure shows that the estimation qualitatively explains the GCM result that the harmonic with the wavenumber 2 is dominant.

4.1.3 Vertical structures

Figure 54 presents the comparison of the spectral decomposition of the temperature at 47° N and $z=2$ m, and at 58° N and at 0.7 mb, in ‘autumn’ for the ‘weak-dust’ scenario. It shows that the wave with $WN=1$ and 5.5 Sols period (hereafter denoted as {5.5 Sols, $WN=1$ } wave) becomes strong at higher altitudes, as well as {3.1 Sols, $WN=2$ } wave.

Figure 55 displays the meridional and vertical cross-sections of the squared refractive index and the amplitude of the temperature fluctuations for {5.5 Sols, $WN=1$ } and {3.1 Sols, $WN=2$ } waves. The squared refractive index characterizes the propagation conditions for waves. It is defined in e.g. *Andrews et al.* [1987]:

$$n_k^2 = \frac{\partial \bar{q} / \partial y}{\bar{u} - c} - \frac{k^2}{a^2 \cos^2 \phi} - \frac{f^2}{4N^2 H^2} \quad (18)$$

where $\partial \bar{q} / \partial y$ is the mean potential vorticity gradient,

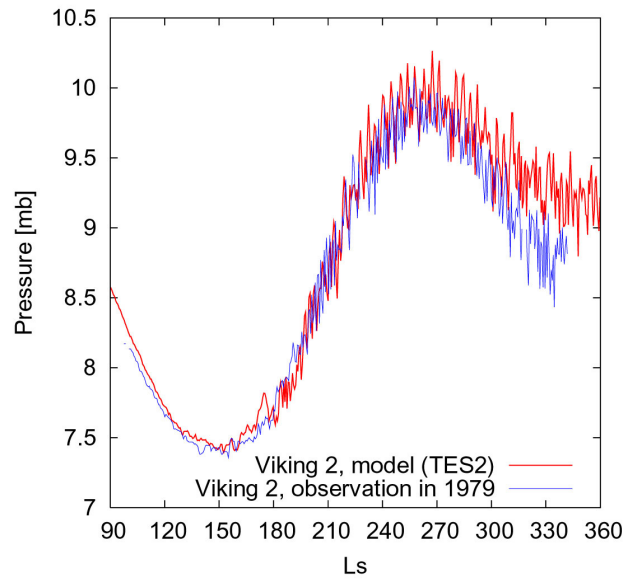


Figure 50: (Red) daily-averaged surface pressure variations at 47° N, 225° W in the GCM run using the TES2 dust scenario ('weak-dust' case), and (blue) those observed by Viking Lander 2 in 1979 (same as the latter part of Figure 7).

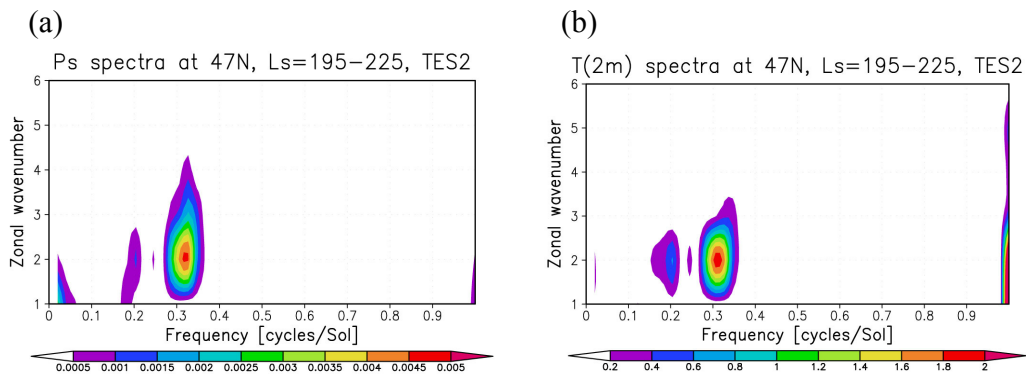


Figure 51: Spectral decomposition of (a) the surface pressure and (b) 2m-height temperature variations at 47° N in the GCM in 'autumn' ($L_s=195^\circ$ - 225°) for the 'weak-dust' (TES2) scenario.

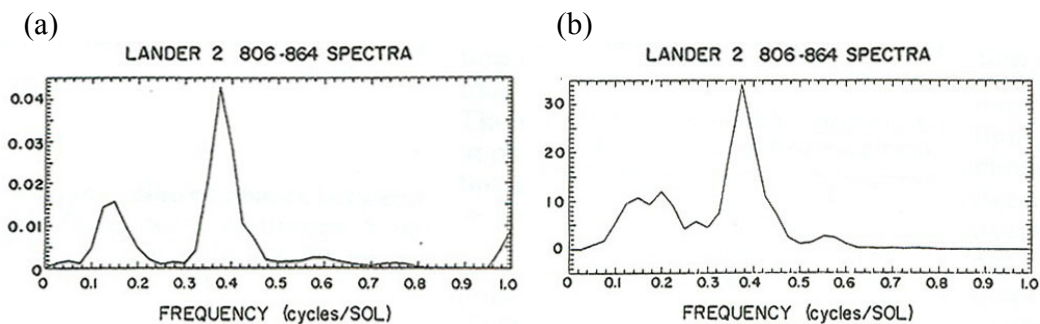


Figure 52: Results of the spectral analyses of (a) surface pressure and (b) temperature variations of the Viking Lander 2 observations for $L_s=190^\circ$ - 226° [Barnes, 1981].

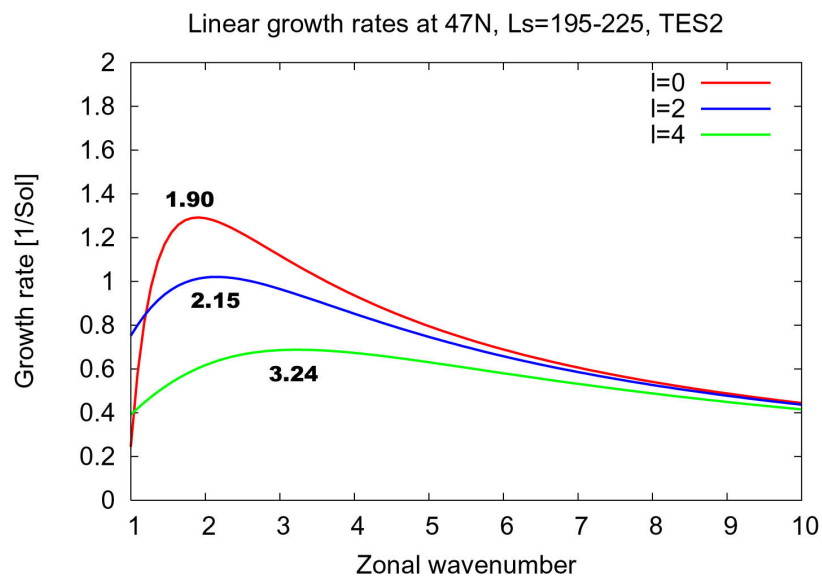


Figure 53: Baroclinic growth rates calculated from (10) [Branscome, 1983] using the typical values of $\partial\bar{u}/\partial z$, N and H from the GCM at 47° N in ‘autumn’ ($L_s=195^\circ-225^\circ$) for the ‘weak-dust’ (TES2) scenario. The plots are for the meridional wavenumbers 0, 2, and 4. The numbers in the figure present the theoretical values of zonal wavenumbers for most unstable meridional harmonics.

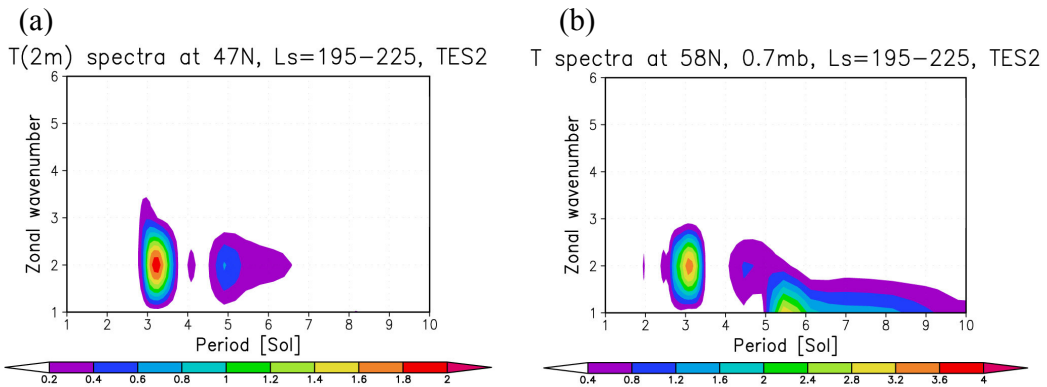


Figure 54: Spectral decomposition of the simulated temperature: (a) at 47° N and $z=2$ m (same as in Figure 51b, but the definition of the horizontal axis is changed), and (b) at 58° N and at 0.7 mb in ‘autumn’ ($L_s=195^\circ$ - 225°) for the ‘weak-dust’ (TES2) scenario.

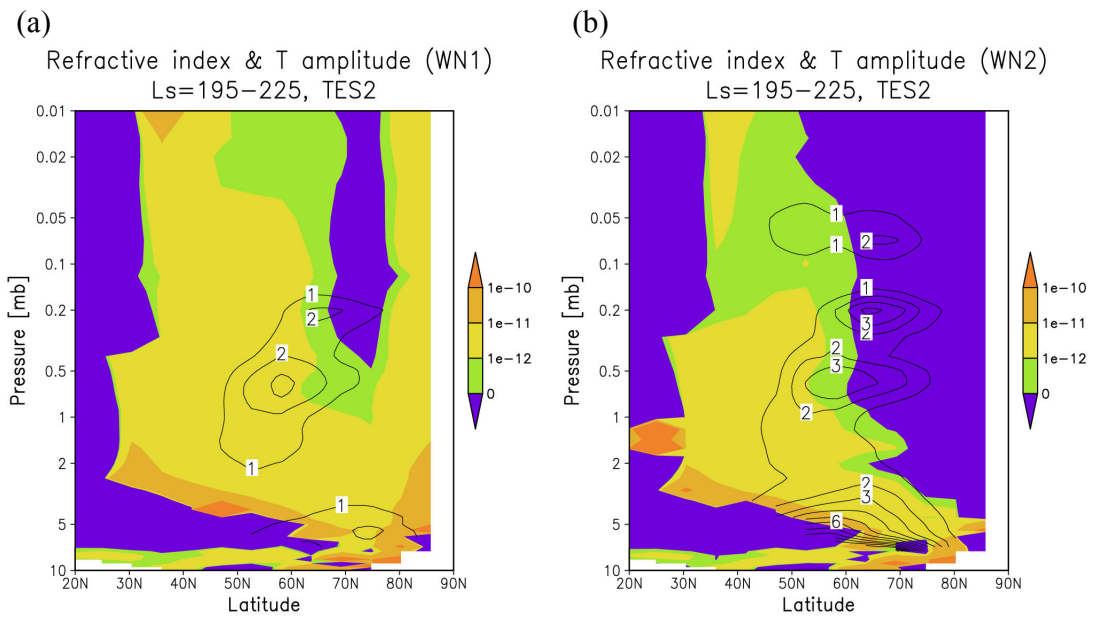


Figure 55: Squared refractive index (shades) and the temperature amplitude (contours) in the north of 20° N for (a) {5.5 Sols, WN=1} and (b) {3.1 Sols, WN=2} waves, in ‘autumn’ ($L_s=195^\circ$ - 225°) for the ‘weak-dust’ (TES2) scenario. The contour interval for the temperature amplitude is 1 K in both (a) and (b).

$$\frac{\partial \bar{q}}{\partial y} = \beta - \frac{f^2}{\rho} \frac{\partial}{\partial z} \left(\frac{\rho}{N^2} \frac{\partial \bar{u}}{\partial z} \right) - \frac{\partial^2 \bar{u}}{\partial y^2} \quad (19)$$

c is the phase speed of the wave component and ρ is the atmospheric density. The wave can propagate only along the region where n_k^2 has positive value. This figure shows that the area where the {3.1 Sols, WN=2} wave can propagate becomes smaller than for the {5.5 Sols, WN=1} harmonic, as the altitude goes up. Due to this reason, it is more difficult for the wave {3.1 Sols, WN=2} to propagate upward than for the {5.5 Sols, WN=1} wave. Therefore, the maximum amplitude of the {3.1 Sols, WN=2} wave at 0.5 mb height is smaller than the amplitude near the surface. The {5.5 Sols, WN=1} wave has almost the same maximum at 0.5 mb and near the surface. These vertical structures for WN=1 and WN=2 components are qualitatively consistent with the spectral analyses of the MGS-TES observational data (see Figure 10a and 10b). Quantitatively the amplitude for WN=2 is ~ 3 times larger than the MGS-TES observational data, while mostly consistent at both heights for WN=1.

4.2 Seasonal changes of the wave properties in the ‘weak-dust’ case

4.2.1 Vertical structure of the waves in ‘winter’

Figure 56 presents the spectral decomposition of the temperature at different altitudes, same as in Figure 54 but for $L_s=280^\circ-300^\circ$ (hereafter labeled as ‘winter’). It is seen from the figure that the {6.6 Sols, WN=1} wave is dominant both near the surface and higher in the GCM. This result is consistent with the MGS-TES observations for this season, in which the {6.5 Sols, WN=1} wave is dominant [Wilson *et al.*, 2002]. The squared refractive index and the magnitude of the temperature fluctuations for the {6.6 Sols, WN=1} wave is plotted in Figure 57. The maximum amplitude of this wave is ~ 35 K at ~ 0.7 mb height and near the surface, which is ~ 10 times larger than for the WN=1 component in ‘autumn’ (see Figure 55a) and 5-10 times larger than in the MGS-TES observational data shown in Figure 58 [Wilson *et al.*, 2002].

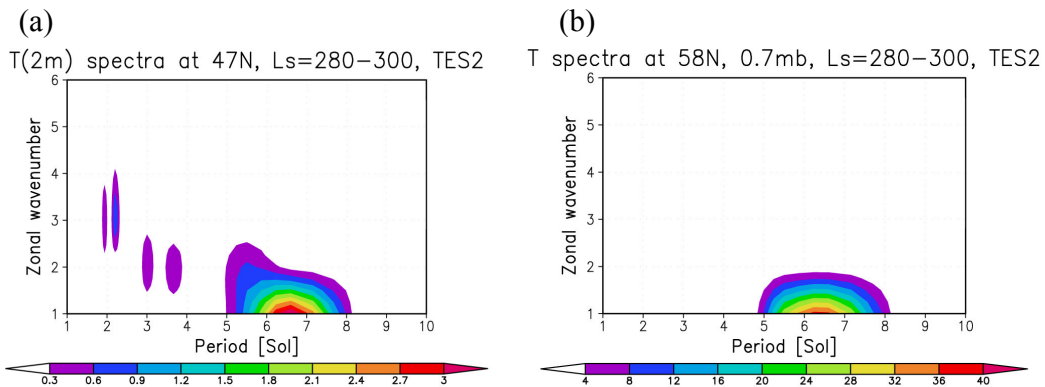


Figure 56: Same as in Figure 54, except in ‘winter’ ($L_s=280^\circ-300^\circ$)

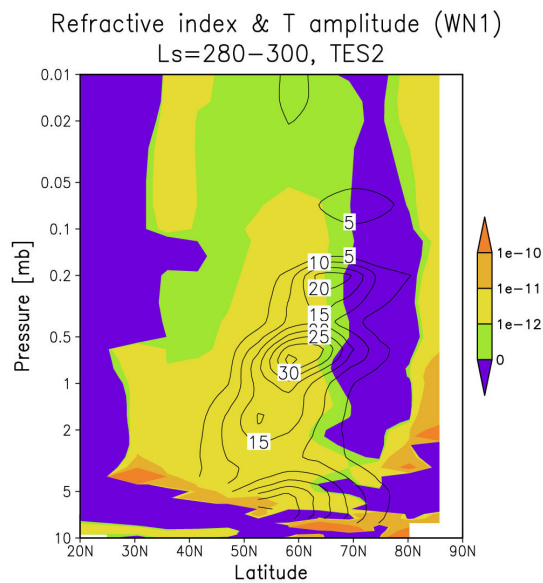


Figure 57: Squared refractive index (shades) and the temperature amplitude (contours) for the {6.6 Sols, WN=1} wave in ‘winter’ ($L_s=280^\circ-300^\circ$) for the ‘weak-dust’ (TES2) scenario. The contour interval for the temperature amplitude is 5 K.

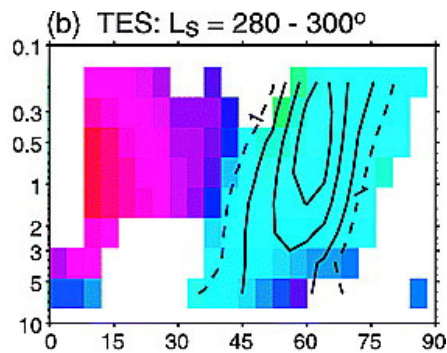


Figure 58: Temperature amplitude of the {6.5 Sols, WN=1} wave in the MGS-TES data for $L_s=280^\circ-300^\circ$ of Mars Year 24 [Wilson et al., 2002]

4.2.2 Seasonal changes of the atmospheric fields

Figures 59, 60 and 61 present the comparison of the zonal-mean temperature / zonal wind, vertical wind shear / squared Brunt-Väisälä frequency and potential vorticity gradient, respectively, between in ‘autumn’ and ‘winter’ for the ‘weak-dust’ scenario. The potential vorticity gradient contains information on the necessary condition for the instability. Change of the sign of $\partial\bar{q}/\partial y$ in the domain usually indicates a baroclinically unstable flow.

The meridional temperature gradient in the northern hemisphere becomes stronger in ‘winter’, which causes larger $\partial\bar{u}/\partial z$ in lower altitude of midlatitudes (below ~ 1 mb, 35 - 65° N), than in ‘autumn’. N^2 at that region also becomes larger in ‘winter’ than in ‘autumn’. These changes are qualitatively consistent with the seasonal change of the wave properties, which dominant wavenumber is shifted from 2 (in ‘autumn’) to 1 (in ‘winter’), from formulae (16) and (17). Moreover, the potential vorticity gradient becomes negative in the upper part (0.1-2 mb) at $\sim 70^\circ$ N in ‘winter’, while such a region is not seen in ‘autumn’. This demonstrates that the instability of internal jet can occur in the upper atmosphere and that baroclinic waves can be generated there only in ‘winter’. As seen from (19), the potential vorticity gradient decreases if $\partial^2\bar{u}/\partial z^2$ and/or $\partial^2\bar{u}/\partial y^2$ increase. One can notice from Figure 59 that $\partial^2\bar{u}/\partial z^2$ and $\partial^2\bar{u}/\partial y^2$ are larger in ‘winter’ than in ‘autumn’ in the north polar region, which may cause the negative value of the potential vorticity gradient in ‘winter’.

Figures 62-64 show the same plots as Figures 59-61, but from the MGS-TES nadir observational data in Mars Year 24, when without a global dust storm. For these figures, the zonal-mean eastward wind velocity \bar{u} is calculated using the following thermal wind relation [e.g. *Andrews et al.*, 1987] assuming $\bar{u}=0$ at ~ 7.8 mb:

$$\left(f + \frac{2\bar{u} \tan \phi}{a}\right) \frac{\partial\bar{u}}{\partial z} = -\frac{g}{aT} \frac{\partial\bar{T}}{\partial\phi} \quad (20)$$

where g is the acceleration of gravity and \bar{T} is the zonal-mean temperature. $\partial\bar{u}/\partial z$ and the potential vorticity gradient are calculated using \bar{u} estimated as above. Note that their values possibly contain considerable errors. Therefore, we consider these results as only

indicative of the tendencies of the change of values.

The model and the observations agree in showing that $\partial\bar{u}/\partial z$ and N^2 at lower levels over midlatitudes increase, and the negative $\partial\bar{q}/\partial y$ region at $\sim 70^\circ$ N gets larger in ‘winter’. These changes can explain the larger amplitude of the baroclinic waves especially for WN=1 in ‘winter’ (see Figure 10).

Figure 65 shows the squared refractive indices for WN=1 wave with a supposed period of 7 Sol, calculated using the parameters in Figures 62-64 from the MGS-TES nadir data in Mars Year 24. As seen in (18), larger negative $\partial\bar{q}/\partial y$ region at $\sim 70^\circ$ N prevents the waves from penetrating northward. In addition, it possibly increases the wave generation. The amplitude distributions of WN=1 waves in both seasons (Figures 10a and 58) fit the distributions of the positive squared refractive index shown in Figure 65. Both the model (see Figures 55a and 57) and the observations show that the seasonal change of the region with negative $\partial\bar{q}/\partial y$ explains the fact that, in ‘winter’, wave amplitudes are stronger and are located southward of $\sim 70^\circ$ N.

4.2.3 Note: Surface temperature and EP-flux

In the model results the quantitative amplitudes of the WN=2 and WN=1 waves in ‘autumn’ and ‘winter’, respectively, are considerably larger than in the observational data, as described in Subsections 4.1.3 and 4.2.1. Here we discuss the possible reasons of this discrepancy.

Figures 66 and 67 compare the daytime surface temperature from the northern autumn equinox to spring equinox using the TES2 dust scenario (‘weak-dust’ case) in the model and the MGS-TES observations. It is seen that the surface temperature at the equator in the model is 20-30 K higher in ‘autumn’ and ~ 10 K higher in ‘winter’, than the MGS-TES observation. Higher surface temperature tends to produce a higher atmospheric temperature near the surface due to the ‘greenhouse’ effect described in Subsection 3.1.1. As the surface temperature in the northern polar region is almost the same between in the model and the observations, the meridional temperature gradient near the surface should be larger in the model.

Figure 68 shows the transient wave component (for the period of more than 1 Sol and

the components by the stationary wave are eliminated) of meridional heat flux $\overline{v'T'}$ and EP-flux $\mathbf{F}=(F_y, F_z)$ calculated using the model output of each season. The components of the EP-flux are defined as follows [e.g. *Andrews et al.*, 1987]:

$$F_y = \frac{p}{p_s} \cos \phi \left[\frac{(\partial \bar{u} / \partial z) \overline{v' \theta'}}{(\partial \bar{\theta} / \partial z)} - \overline{v' u'} \right] \quad (21)$$

$$F_z = \frac{p}{p_s} \cos \phi \left\{ \left[f - \frac{1}{a \cos \phi} \frac{\partial (\bar{u} \cos \phi)}{\partial \phi} \right] \frac{\overline{v' \theta'}}{(\partial \bar{\theta} / \partial z)} - \overline{w' u'} \right\} \quad (22)$$

where p_0 is the reference pressure (defined as 7.0 mb in the simulations). This figure shows that the waves are generated, and the strong northward heat transport is seen near the surface, where $\partial \bar{q} / \partial y$ has negative values (see Figure 61) in both seasons. In the MGS-TES observations, such instability near the surface is not seen (see Figure 64), although the resolution of the data is quite rough. In summary, the existence of the strong instabilities near the surface due to higher daytime surface temperature in tropics may cause the generation of the baroclinic waves with larger than observed amplitudes.

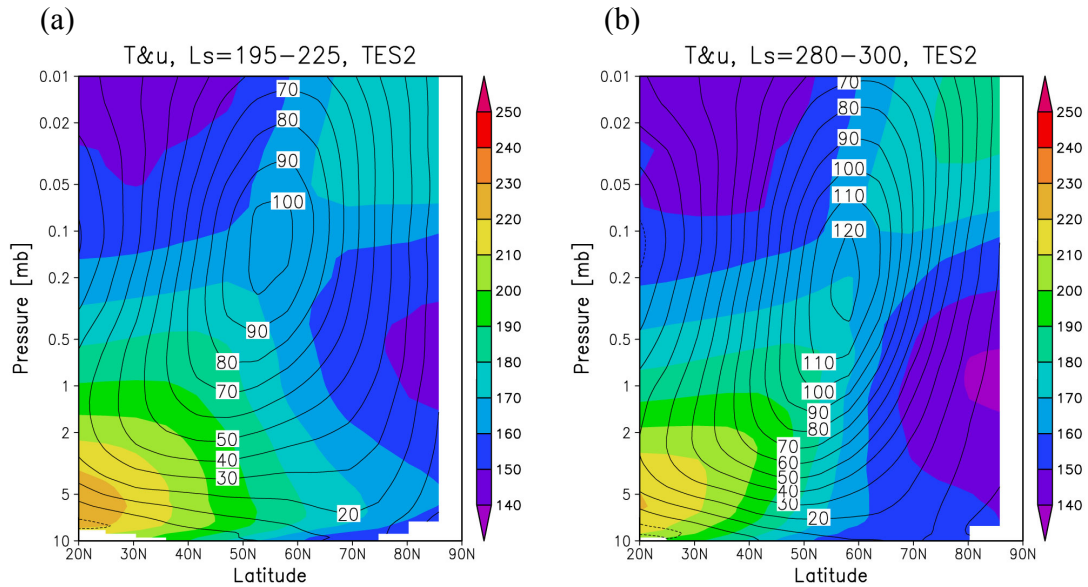


Figure 59: Zonal-mean temperature [K] (shades) and zonal wind [$m s^{-1}$] (contours) simulated in the model for the 'weak-dust' (TES2) scenario, (a) in 'autumn' ($L_s=195^\circ-225^\circ$) and (b) in 'winter' ($L_s=280^\circ-300^\circ$).

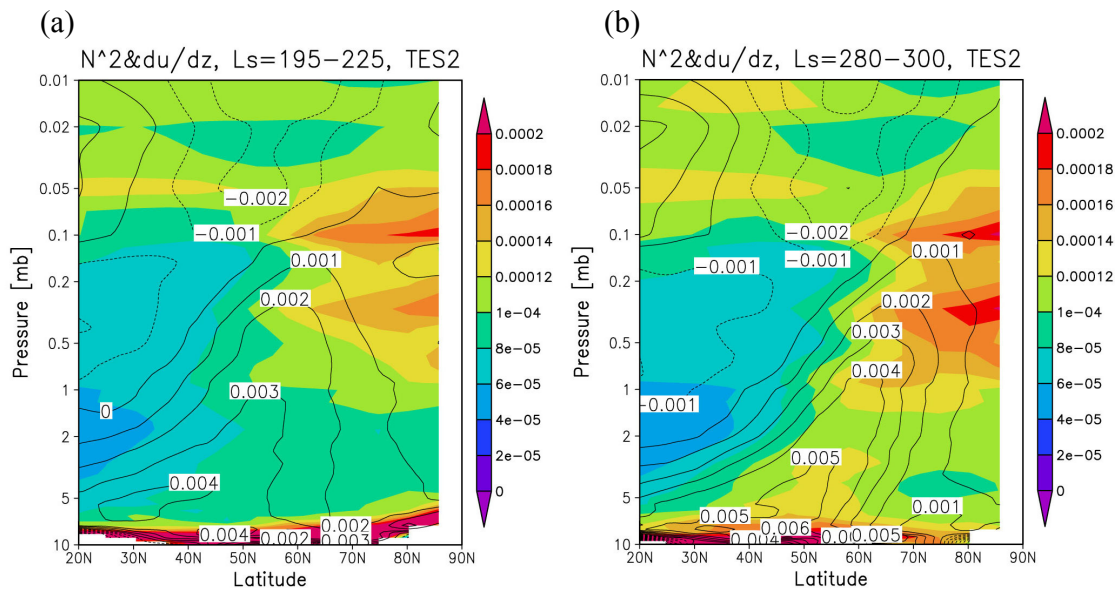


Figure 60: The vertical wind shear [s^{-1}] (contours) and the squared Brunt-Väisälä frequency [s^{-2}] (shades) simulated in the model for the 'weak-dust' (TES2) scenario, (a) in 'autumn' ($L_s=195^\circ-225^\circ$) and (b) in 'winter' ($L_s=280^\circ-300^\circ$).

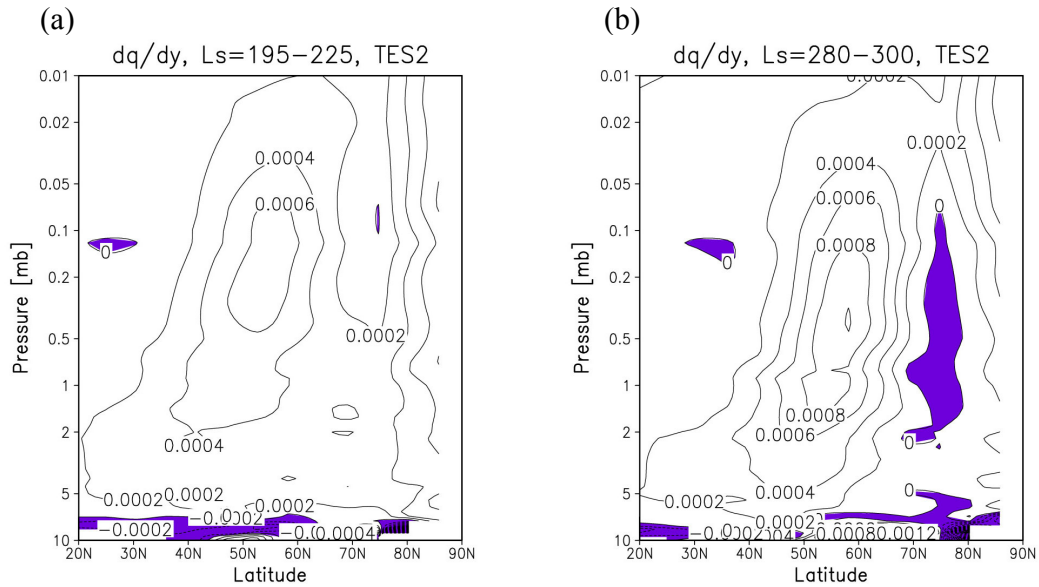


Figure 61: The meridional gradient of the potential vorticity $\partial\bar{q}/\partial y$ multiplied by the radius of planet [s^{-1}] simulated in the model for the ‘weak-dust’ (TES2) scenario, (a) in ‘autumn’ ($L_s=195^\circ-225^\circ$) and (b) in ‘winter’ ($L_s=280^\circ-300^\circ$). The purple shades indicate the area where the potential vorticity gradient is negative and the necessary condition for instability of internal jet is satisfied.

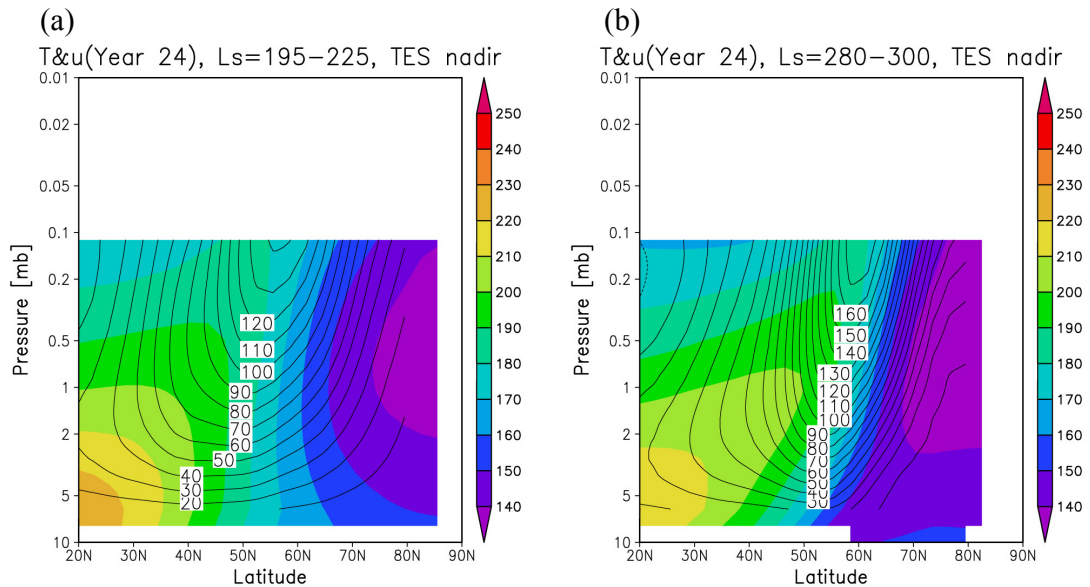


Figure 62: Same as in Figure 59, except from the MGS-TES nadir observational data in Mars Year 24.

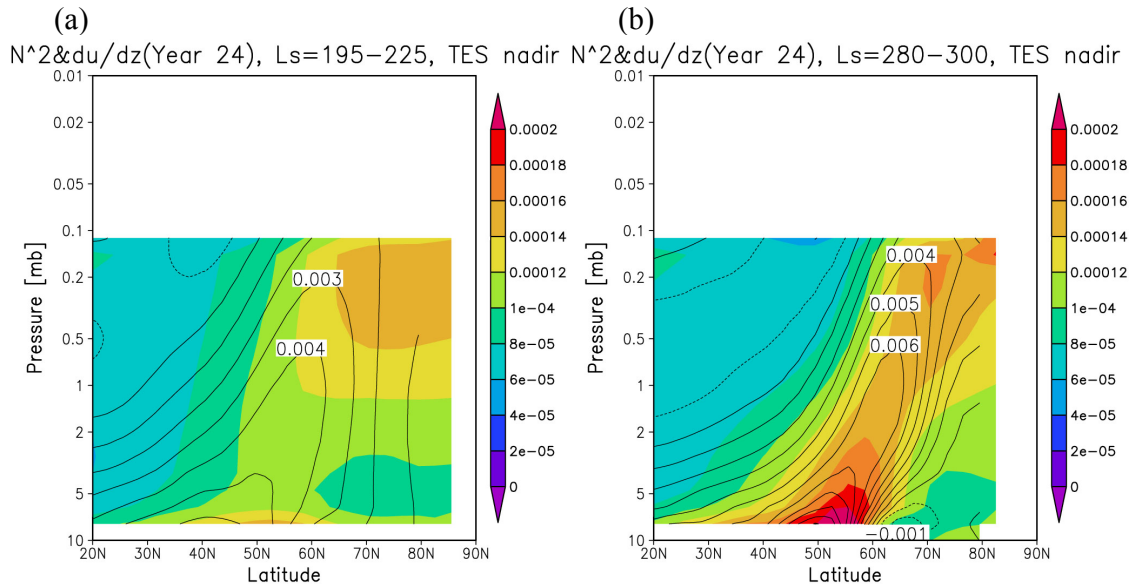


Figure 63: Same as in Figure 60, except from the MGS-TES nadir observational data in Mars Year 24.

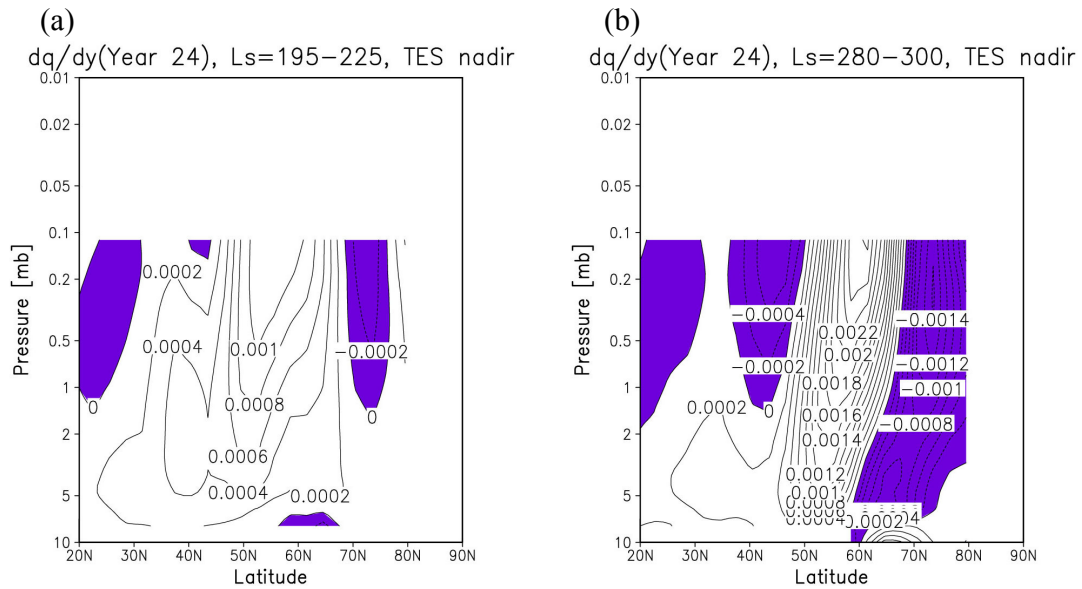


Figure 64: Same as in Figure 61, except from the MGS-TES nadir observational data in Mars Year 24.

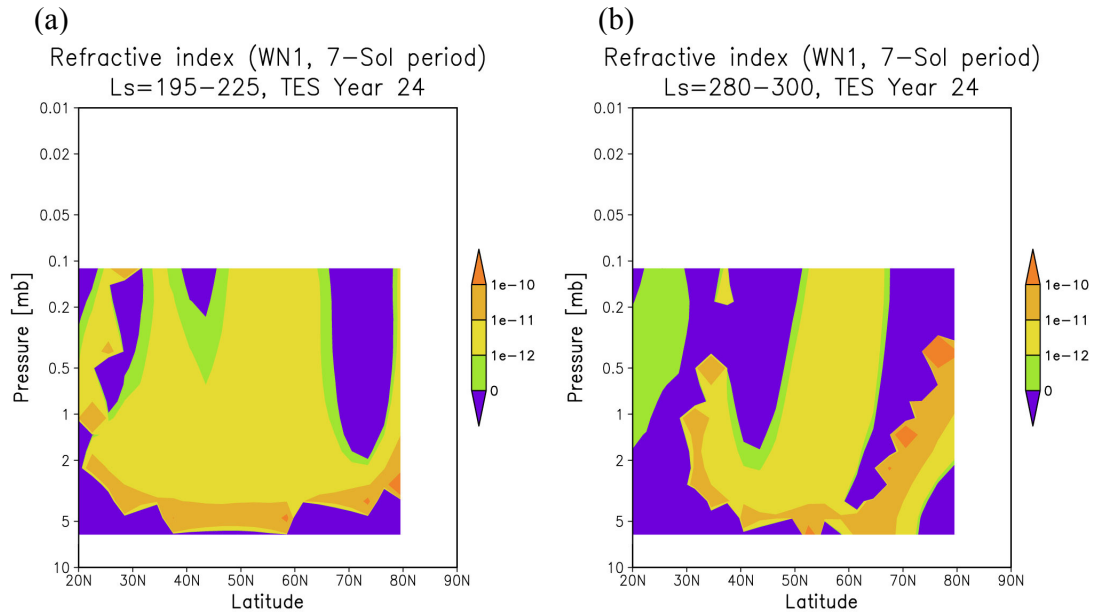


Figure 65: Squared refractive index (shades) in the north of 20° N for the {7 Sols, WN=1} wave from the MGS-TES nadir observational data in Mars Year 24, (a) in ‘autumn’ ($L_s=195^\circ\text{-}225^\circ$) and (b) in ‘winter’ ($L_s=280^\circ\text{-}300^\circ$).

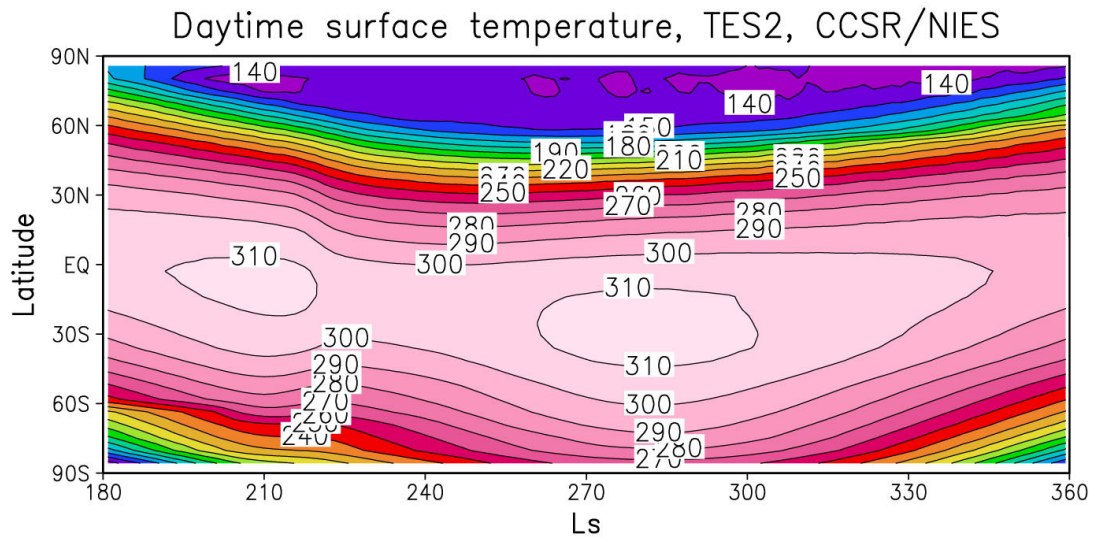


Figure 66: Time-latitude cross-section of zonal-mean daytime (local time ~1400) model results of surface temperature [K] from the northern autumn equinox ($L_s=180^\circ$) to spring equinox ($L_s=360^\circ$), using the TES2 dust scenario (‘weak-dust’ case).

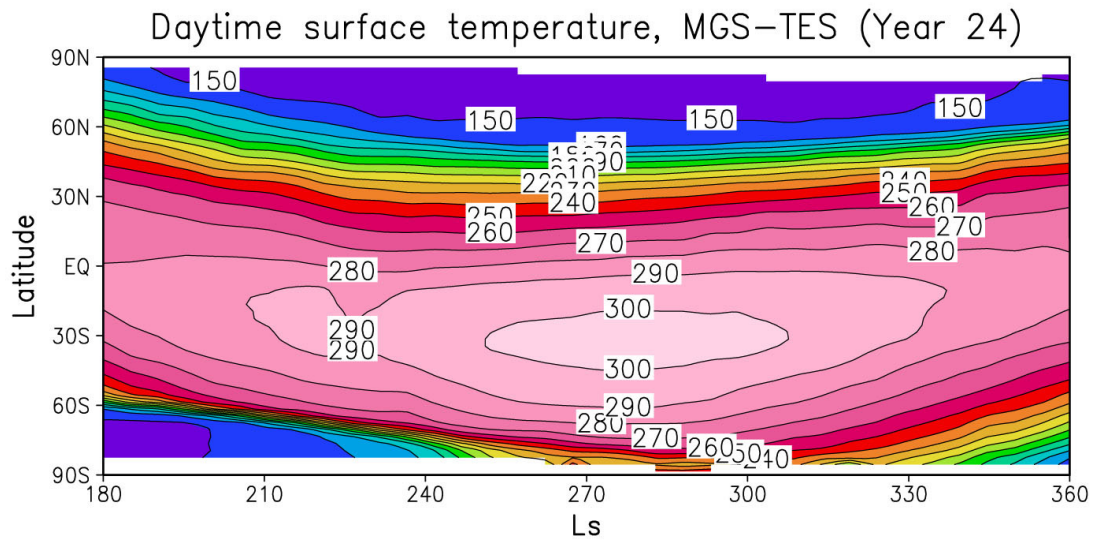


Figure 67: Same as in Figure 66, except for the MGS-TES observations in Mars Year 24.

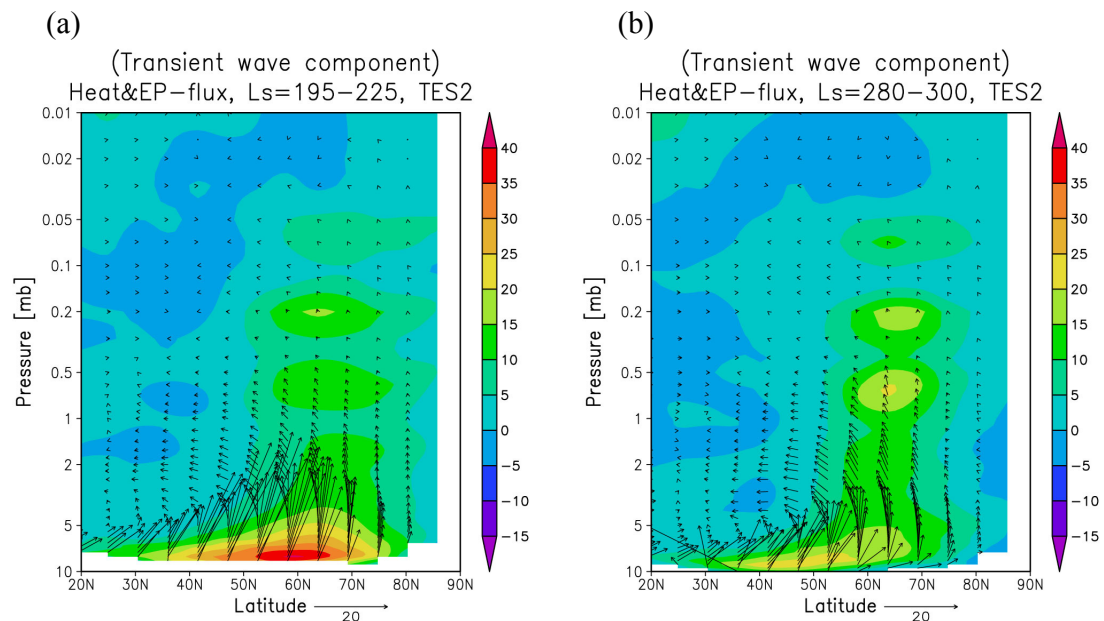


Figure 68: Transient wave component of the meridional heat flux $\overline{v'T'}$ [K m s^{-1}] (shades) and EP-flux [$\text{m}^2 \text{s}^{-1} \text{Sol}^{-1}$] (arrows) simulated in the model for the ‘weak-dust’ (TES2) scenario, (a) in ‘autumn’ ($L_s=195^\circ\text{-}225^\circ$) and (b) in ‘winter’ ($L_s=280^\circ\text{-}300^\circ$).

4.3 Changes of the wave properties due to the global dust storm

4.3.1 In ‘autumn’

It is seen in Figures 42-45 that a planet-encircling dust storm induces strong dynamical heating rates above ~ 1 mb over the northern polar region, which results in the strong winter polar warming, and that the stronger dust heating causes the temperature increase above ~ 4 mb. Figure 69 shows the mass stream function Ψ_M defined as follows, for the comparison between the ‘weak-dust’ and ‘strong-dust’ cases:

$$\Psi_M = -\frac{2\pi a \cos \phi}{g} \int_0^p v dp \quad (23)$$

where v is the northward meridional wind velocity, and p is the pressure. The meridional and vertical gradients of Ψ_M show the strength of the circulation, as the velocities of meridional wind v and vertical wind ω (the unit is Pa s^{-1} , i.e. a positive value shows a downward flow) are related to Ψ_M via the following equations.

$$v = -\frac{g}{2\pi a \cos \phi} \frac{\partial \Psi_M}{\partial p} \quad (24)$$

$$\omega = \frac{g}{2\pi a^2 \cos \phi} \frac{\partial \Psi_M}{\partial \phi} \quad (25)$$

From Figure 69 and the above equations, it is apparent that the downward flow at $\sim 60^\circ$ N around 0.01-0.2 mb height is stronger in the ‘strong-dust’ case, as the stronger dust heating in the southern subtropics enhances the meridional circulation. Note that the existence of the positive values of the mass stream function near the surface of tropics and subtropics is due to the southward and upward flow which follows the zonal-mean topography with the south-north slope (details are in Appendix E).

Figure 70 shows the simulated zonal mean temperature, zonal wind, $\partial \bar{u} / \partial z$ and N^2 in the ‘strong-dust’ case. $\partial \bar{u} / \partial z$ and N^2 increase in mid-latitudes compared to the ‘weak-dust’

case (see Figures 59a and 60a). It occurs because of the significant increase of the temperature above ~ 2 mb in the south of $\sim 40^\circ$ N due to the dust radiative heating (see Figure 43), although the temperature above the north pole also increases.

Figure 71 demonstrates the results of the spectral analysis for the temperature at different altitudes, same as in Figure 54 but for the run with the ‘strong dust’. This figure shows that, in the simulations, the {8.2 Sols, WN=1} wave is dominant both near the surface and higher, unlike in the ‘weak-dust’ case for which the {3.1 Sols, WN=2} harmonic is the strongest. The altered wavenumber of the dominant wave can be explained by the larger $\partial\bar{u}/\partial z$ and N^2 in the ‘strong-dust’ case. When enters the linear instability estimate (17), this vertical wind shear tends to generate harmonics with smaller wavenumber. The phase speed of the dominant wave becomes slower, possibly, because the zero line separating easterlies and westerlies near the surface is shifted northward (see Figures 59a and 70a).

Figure 72 presents the squared refractive index and the amplitude of the temperature for the {8.2 Sols, WN=1} wave. The maximum amplitude of ~ 12 K occurs near the surface and at ~ 0.2 mb height. The distribution of the amplitude is qualitatively consistent with the MGS-TES observations (see Figure 11a).

Figure 73 shows the daytime surface temperature in comparison with the MGS-TES observations in Mars Year 25, and Figure 74 shows the transient wave component of the meridional heat flux and EP-flux. Compared to the ‘weak-dust’ case, the magnitude of the meridional heat flux near the surface becomes smaller (less than $\sim 70\%$), especially to the south of $\sim 60^\circ$ N. This is possibly because the meridional temperature gradient near the surface becomes smaller than in the ‘weak-dust’ case, as expected from the lower surface temperature in midlatitudes and subtropics due to a global dust storm (see Figures 66 and 73a). Nevertheless, the surface temperature in midlatitudes and subtropics is 20-30 K higher than in the MGS-TES observations during a global dust storm (see Figure 73), which seems to cause a ~ 6 times larger wave amplitude than in the observational data (see Figures 11a and 72).

Figure 75 presents the zonal mean temperature, zonal wind, $\partial\bar{u}/\partial z$ and N^2 from the MGS-TES data in Mars Year 25. In comparison with the same season in Mars Year 24 (see Figures 62a and 63a), $\partial\bar{u}/\partial z$ is almost the same and N^2 increases. It is seen that the

temperature increase above ~ 2 mb in the south of $\sim 40^\circ$ N keeps the meridional temperature gradient in the northern midlatitudes, as well as in the model.

4.3.2 In ‘winter’

Hereafter the ‘strong-dust’ case will denote the VIK1 dust scenario with the global-mean visible dust opacity averaged over ‘winter’ ($L_s=280^\circ$ - 300°) of 4.2.

Figure 76 gives the seasonal variations of the simulated (using the VIK1 dust scenario) daily mean surface pressure, and compares them with the Viking Lander 2 observations. The latter include the occurrence of two planet-encircling dust storms (in 1977). As described in Chapter 1, the significant reduction of the oscillations induced by baroclinic waves was observed during the second planet-encircling dust storm (around $L_s=280^\circ$ - 310°). This reduction of the oscillations is reproduced in the simulation. No significant reduction was observed during the first dust storm. As described in the previous subsection, the planet-encircling dust storm in ‘autumn’ does not extinguish the meridional temperature gradient because of the stronger dust heating effects in subtropics compared to the dynamical heating above the northern polar region (see Figure 43), and thus favors the baroclinic wave generation.

Figure 77 presents the comparison of the zonal mean temperature during the ‘winter’ for the ‘weak-dust’ and ‘strong-dust’ cases. In the ‘strong-dust’ case, the temperature above ~ 1 mb at 50 - 80° N rises extremely, by ~ 60 K in the maximum. This temperature above the polar night is comparable to that observed by Viking spacecraft [Martin and Kieffer, 1979]. The comparisons of the diabatic and dynamical heating/cooling rates are plotted in Figure 78, and the comparison of the mass stream function is shown in Figure 79. The strong adiabatic heating produces the polar temperature maxima in both ‘autumn’ and ‘winter’. However, in ‘winter’, the stream function shows that the anti-clockwise Ferrel type circulation cell completely disappears in the northern hemisphere, while a small cell remains during the ‘autumn’ (see Figure 69b). Ferrel circulation may indicate a possibility or a likelihood of the existence of baroclinic waves. Therefore, the disappearance of the Ferrel cell may show a drastic change in the wave structure at midlatitudes.

Figure 80 shows the spectral decomposition of the simulated temperature at different

altitudes, same as Figures 54, 56 and 71 but in ‘winter’ for the ‘strong-dust’ scenario. As seen in Figure 80a, the dominant waves near the surface have larger wavenumbers and smaller amplitudes than in the three cases discussed above. This is qualitatively consistent with the results of the spectral analysis of the Viking Lander 2 observational data (see Table 1). The dominant waves have wavenumbers up to $WN=5$, while in the other three cases, they normally have $WN=2$ to 3. Moreover, the amplitude of the dominant wave is ~ 0.12 K for the {4.7 Sols, $WN=2$ } wave, or about only 1/30 of that for the {6.6 Sols, $WN=1$ } wave in the ‘weak-dust’ case.

These differences can be explained with the linear instability analysis given by formulae (16) and (17). Figure 81 presents the simulated zonal-mean temperature, zonal wind, $\partial\bar{u}/\partial z$ and N^2 in this case. It is seen that the low-level vertical wind shear above midlatitudes is mostly weaker than in the ‘weak-dust’ case (see Figures 59b and 60b). Especially near the surface it becomes less than 0.001 s^{-1} , while ~ 0.006 s^{-1} in the ‘weak-dust’ case. It follows from (12) that the value of γ increases approximately from 0.5 to 3, if $\partial\bar{u}/\partial z$ changes from 0.006 to 0.001 and the other variables remain the same. For $\gamma=3$, k_{\max} becomes 2.67 times larger than for $\gamma=0.5$. This agrees well with the GCM results. Smaller Brunt-Väisälä frequency near the surface in the ‘strong-dust’ case also tends to increase the dominant wavenumber. In the ‘weak-dust’ case, the model has a strong CO_2 heating near the surface owing to the daytime infrared radiation (see Figure 78a and Section 3.1). In the ‘strong-dust’ case, the near surface heating gets weaker (see Figure 78d and Section 3.2), which results in less stability near the surface.

Figure 82 presents the squared refractive index and the amplitude of the temperature fluctuations for the {5.5 Sols, $WN=1$ }, {4.7 Sols, $WN=2$ } and {3.7 Sols, $WN=3$ } waves. As seen in Figure 80, the wave spectrum differs significantly near the surface and higher, which is quite different from other three cases discussed above (see Figures 54, 56 and 71). The {4.7 Sols, $WN=2$ } and {3.7 Sols, $WN=3$ } waves which are strong near the surface, but almost disappear at higher altitudes, while the {5.5 Sols, $WN=1$ } wave becomes the dominant. As seen in the refractive index cross-section in Figure 82 and is described in Section 4.1, the upward propagation is more difficult for the harmonics with larger wavenumbers. For the waves with $WN=3$ or larger, there is no region where the refractive index is positive in the middle atmosphere at midlatitudes, as seen in Figure

82c, i.e. the propagation is inhibited.

Figure 83 shows the transient wave component of meridional heat flux and EP-flux. The magnitude of the fluxes from the surface is very small. This shows that the propagation of waves from the surface to higher altitudes almost disappears.

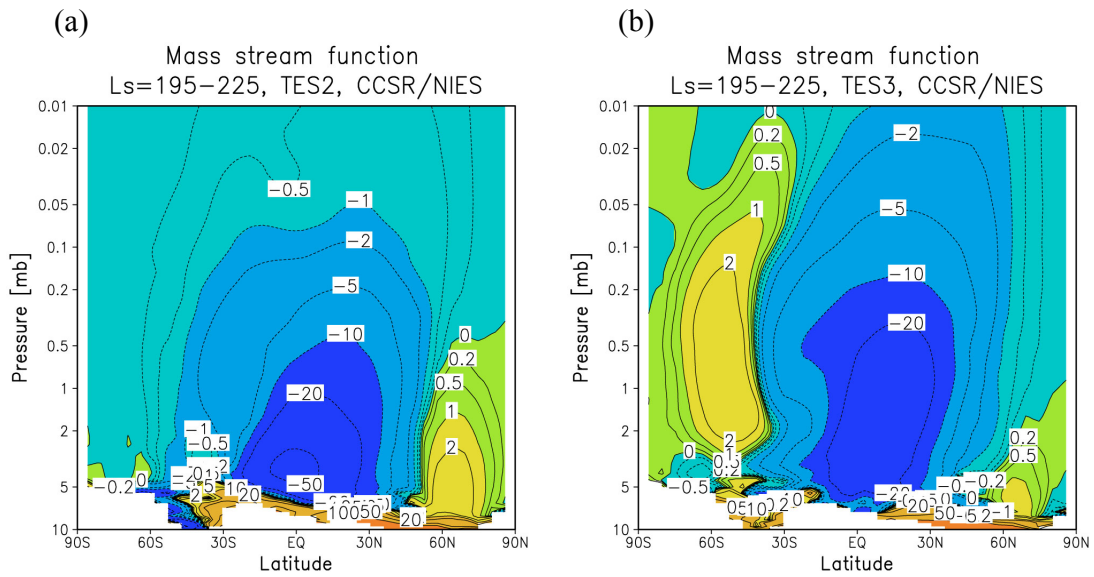


Figure 69: Mass stream function [$\times 10^8 \text{ kg s}^{-1}$] in 'autumn' ($L_s = 195^\circ - 225^\circ$), (a) for the 'weak-dust' (TES2) scenario, and (b) for the 'strong dust' (TES3) scenario.

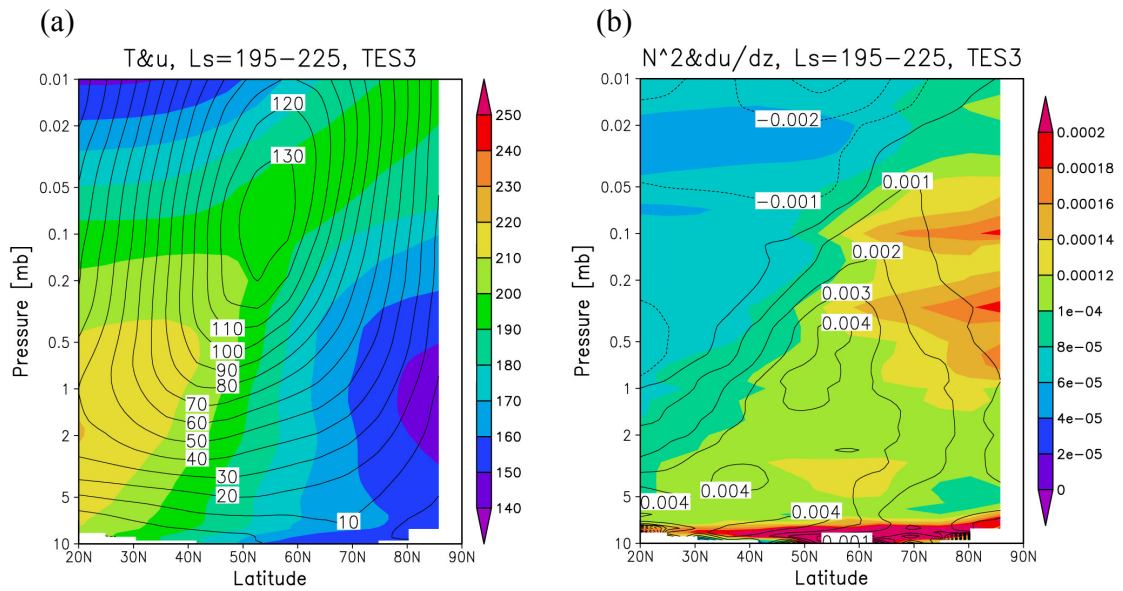


Figure 70: Same as in (a) Figure 59a and (b) Figure 60a, except for the 'strong-dust' (TES3) scenario.

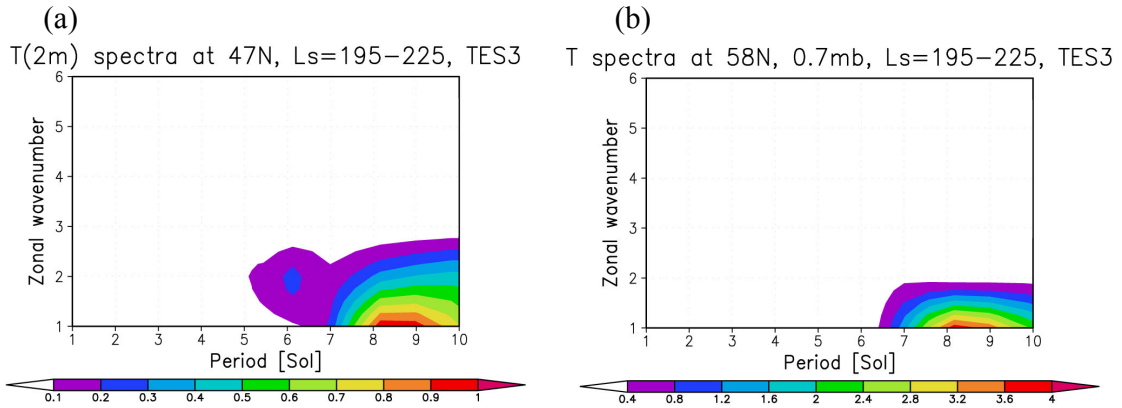


Figure 71: Same as in Figure 54, except for the ‘strong-dust’ (TES3) scenario.

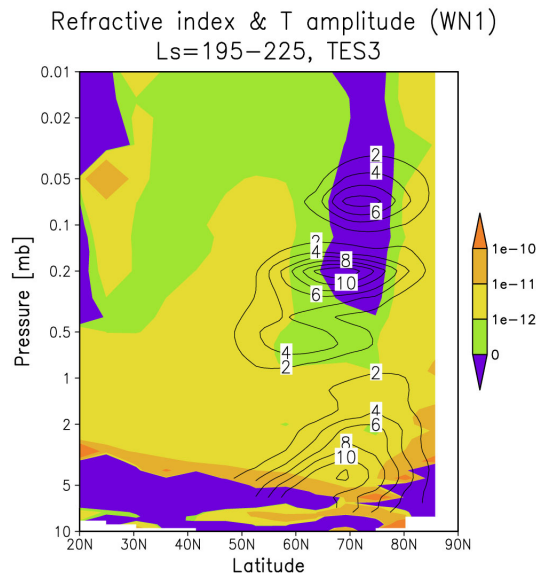


Figure 72: Squared refractive index (shades) and the temperature amplitude (contours) in the north of 20° N for the {8.2 Sols, WN=1} wave in ‘autumn’ ($L_s=195^\circ-225^\circ$) for the ‘strong-dust’ (TES3) scenario. The contour interval for the temperature amplitude is 2 K.

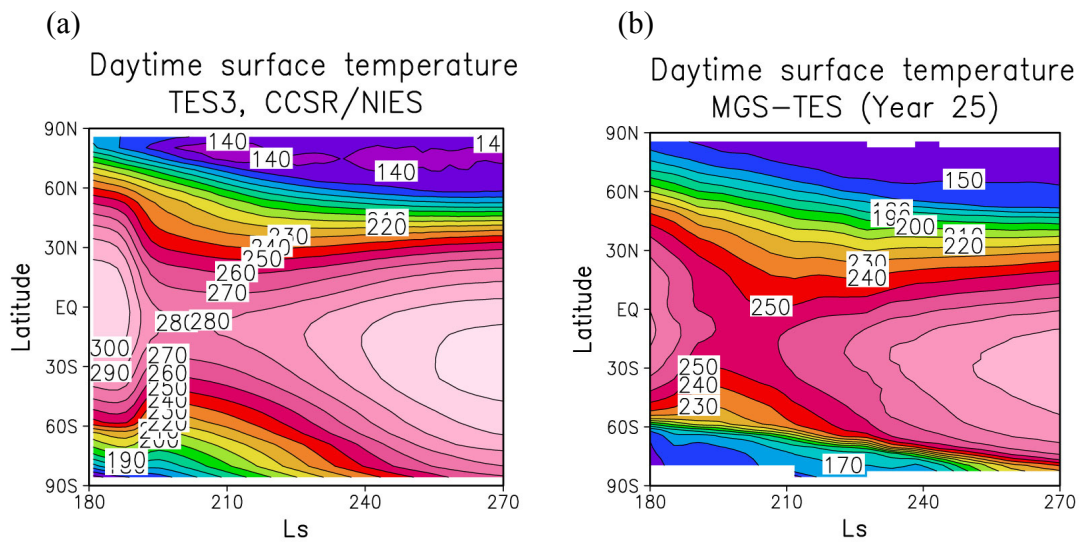


Figure 73: (a) Same as in Figure 66, except from the northern autumn equinox ($L_s=180^\circ$) to the winter solstice ($L_s=270^\circ$) and using the TES3 dust scenario ('strong-dust' case). (b) Same as in Figure 67, except for the MGS-TES observations in Mars Year 25.

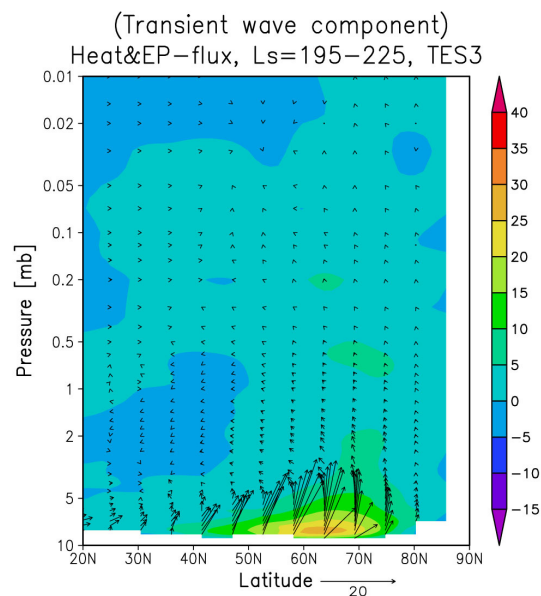


Figure 74: Same as in Figure 68a, except for the 'strong-dust' (TES3) scenario.

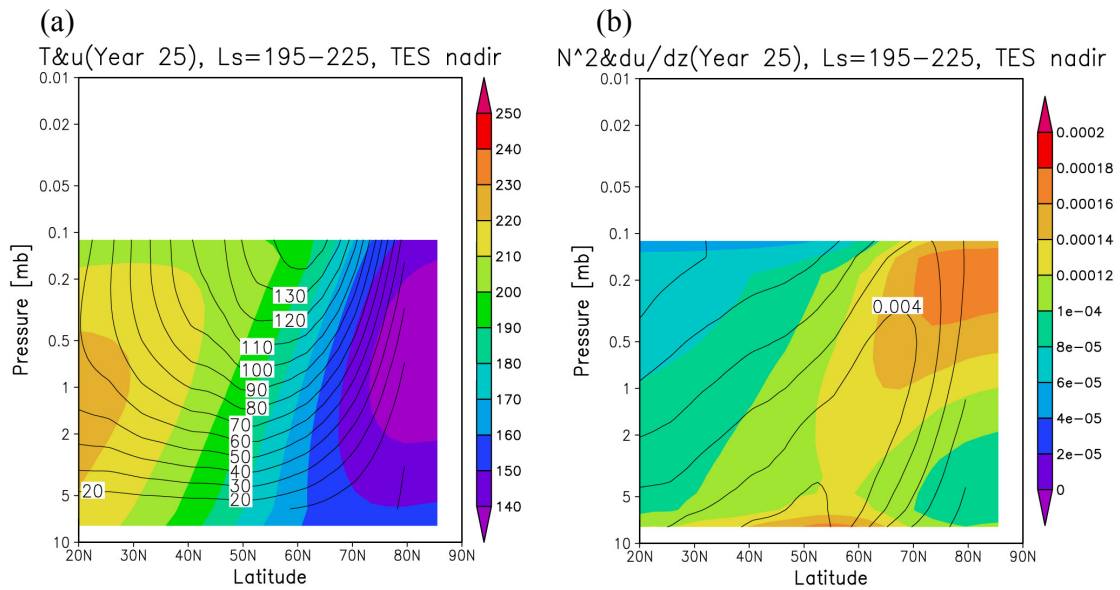


Figure 75: Same as (a) Figure 59a and (b) Figure 60a, except from the MGS-TES observational data in Mars Year 25.

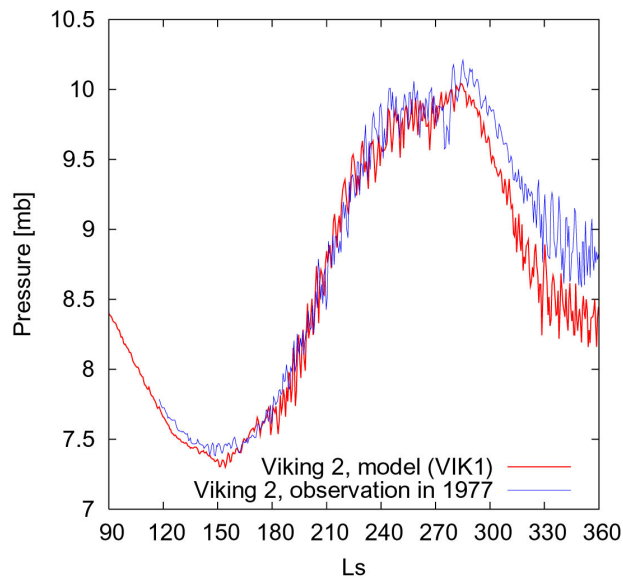


Figure 76: (Red) daily-averaged surface pressure variations at (47° N, 225° W) simulated using the VIK1 dust scenario (including two planet-encircling dust storms around $L_s=210^{\circ}$ - 250° and $L_s=280^{\circ}$ - 310°), and (blue) those observed by Viking Lander 2 in 1977 (same as the former part of Figure 7).

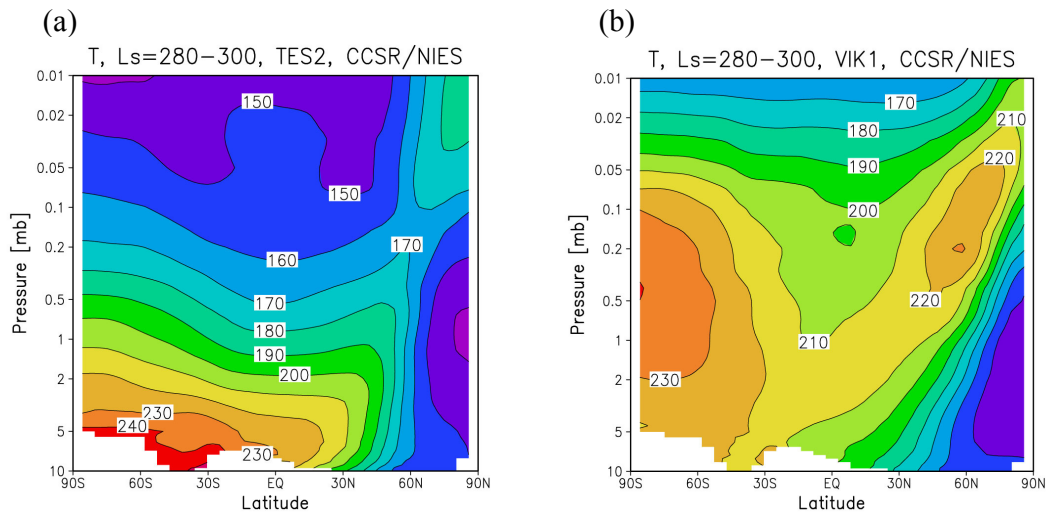


Figure 77: The simulated zonal mean temperature [K] in ‘winter’ ($L_s=280^\circ-300^\circ$), (a) for the ‘weak-dust’ (TES2) scenario, and (b) for the ‘strong dust’ (VIK1) scenario.

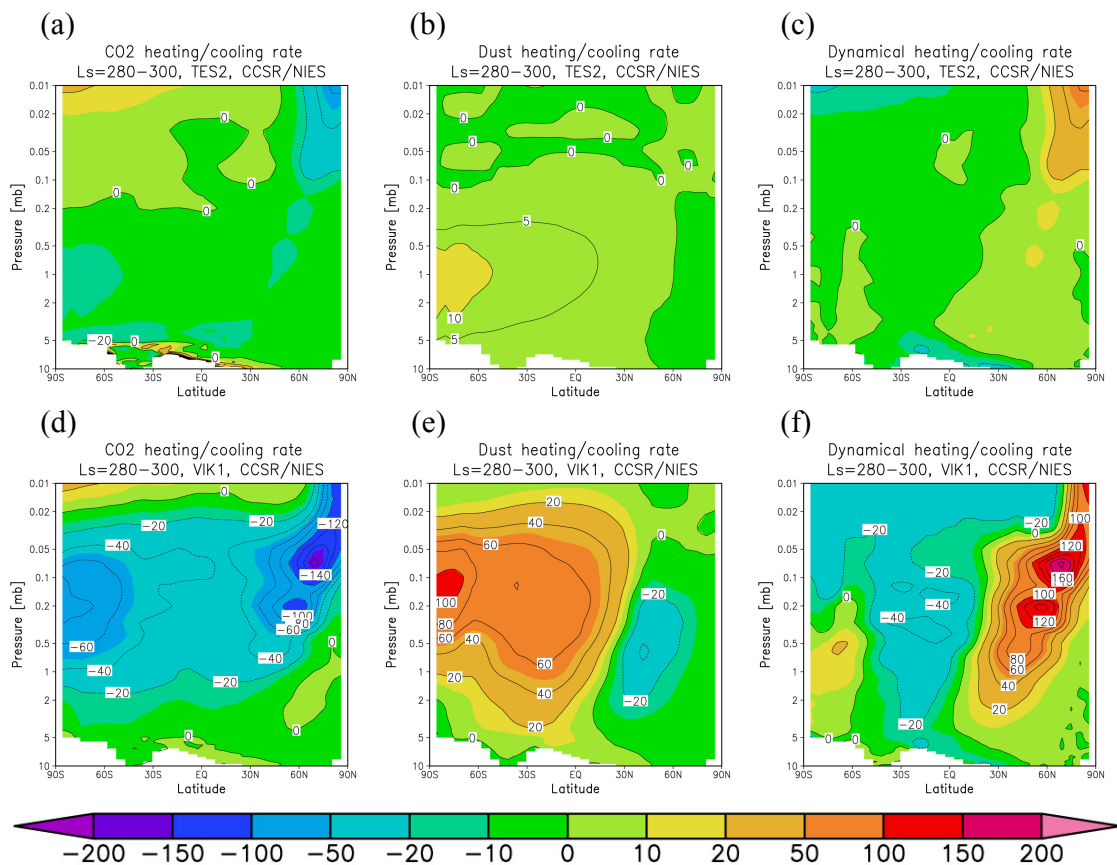


Figure 78: Zonal-mean and daily mean heating/cooling rates [K Sol^{-1}] averaged in ‘winter’ ($L_s=280^\circ-300^\circ$): (a) due to CO_2 , (b) due to dust and (c) due to the dynamical effects for the ‘weak-dust’ (TES2) scenario. (a) and (b) present the total for all (solar + infrared) wavelengths. (d), (e) and (f) are the same as (a), (b) and (c), respectively, except for the ‘strong-dust’ (VIK1) scenario.

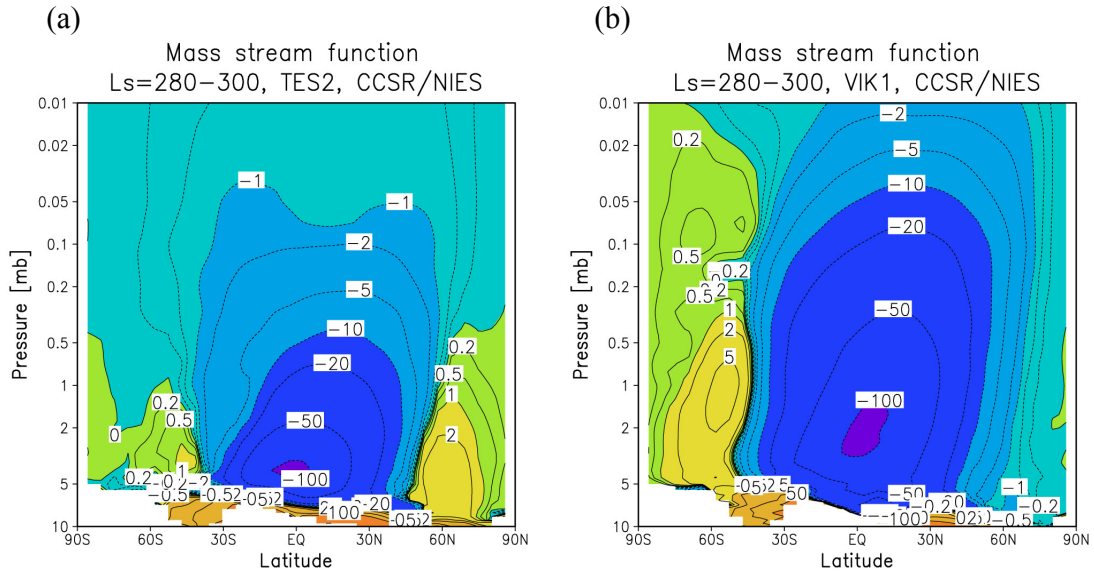


Figure 79: Mass stream function [$\times 10^8 \text{ kg s}^{-1}$] in 'autumn' ($L_s=195^\circ\text{-}225^\circ$), (a) for the 'weak-dust' (TES2) scenario, and (b) for the 'strong dust' (VIK1) scenario.

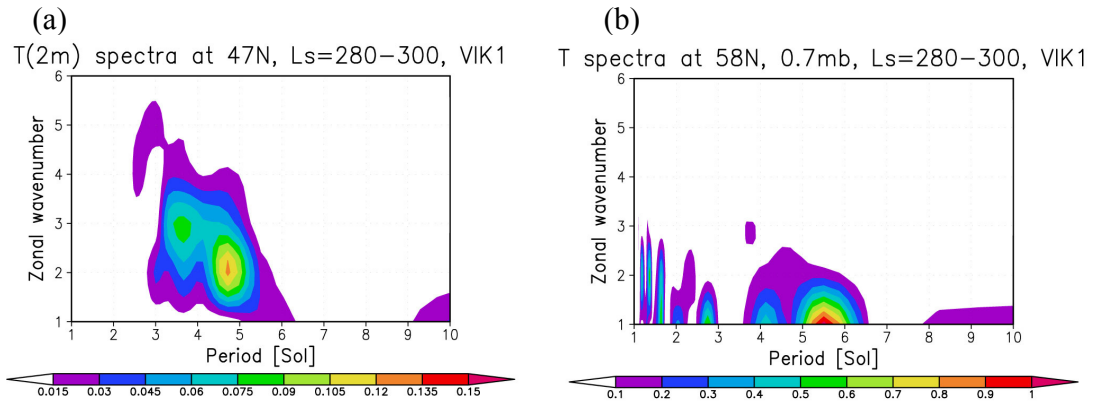


Figure 80: Same as in Figure 54, except in 'winter' ($L_s=280^\circ\text{-}300^\circ$) for the 'strong-dust' (VIK1) scenario.

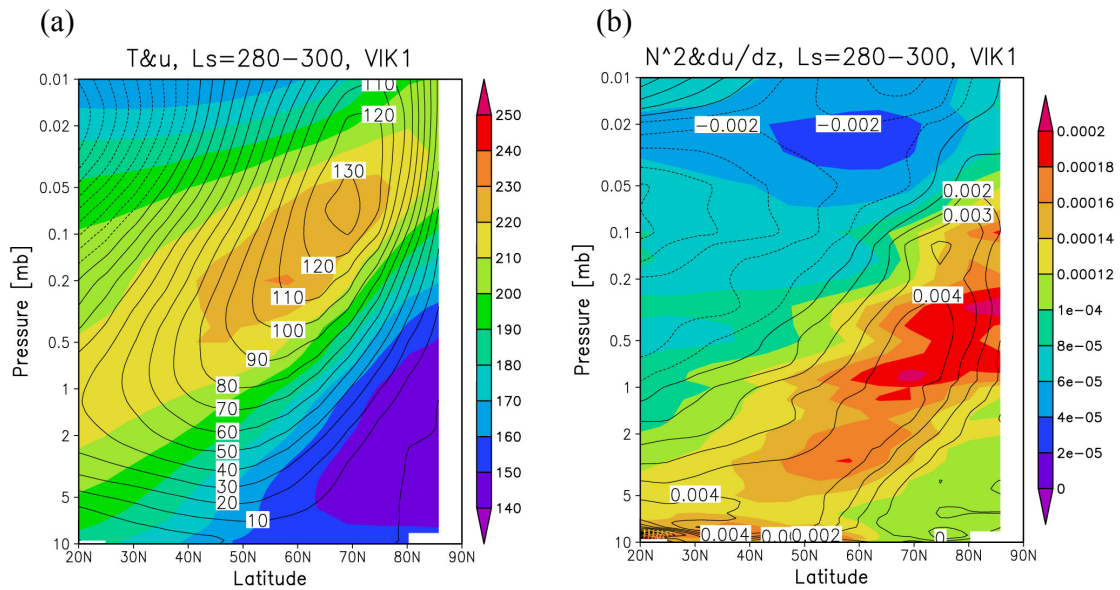


Figure 81: Same as (a) Figure 59b and (b) Figure 60b, except for the ‘strong-dust’ (VIK1) scenario.

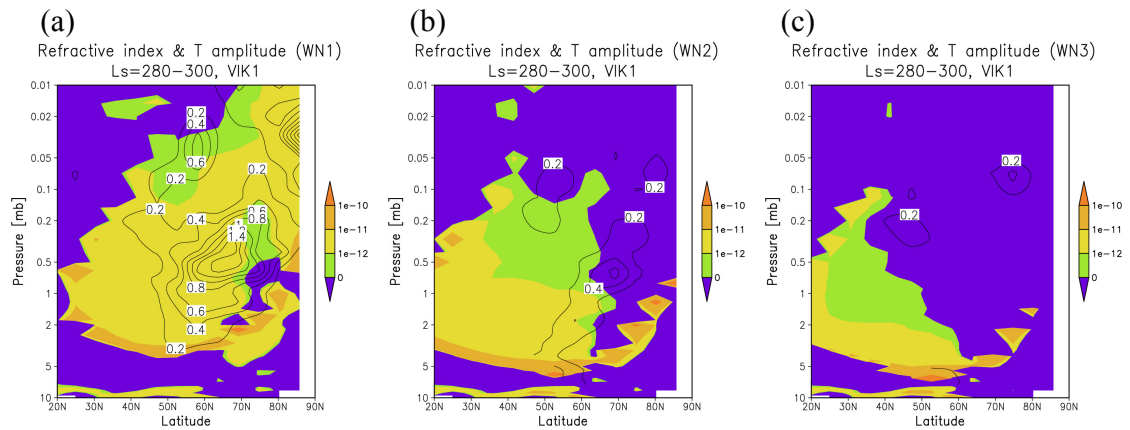


Figure 82: Squared refractive index (shades) and the temperature amplitude (contours) for the (a) {5.5Sols, WN=1}, (b) {4.7 Sols, WN=2} and (c) {3.7 Sols, WN=3} waves, in ‘winter’ ($L_s=280^\circ-300^\circ$) for the ‘strong-dust’ (VIK1) scenario. The contour interval for the temperature amplitude is 0.2 K in all the plots.

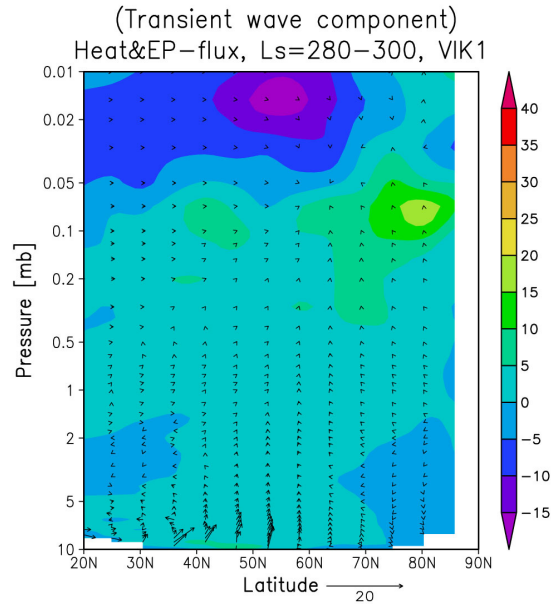


Figure 83: Same as in Figure 68b, except for the ‘strong-dust’ (VIK1) scenario.

Chapter 5

Conclusions

The main purpose of this work was to study the radiative and dynamical effects of dust in the Martian atmosphere. In the course of this doctorate work, a General Circulation Model (GCM) of the Martian atmosphere was developed by converting a terrestrial GCM. This conversion included the introduction of the appropriate for Mars physical parameters as well as the implementation of the physical parameterizations unique for the Martian atmosphere. The main emphasis in this work was on the radiative effects of the CO₂ and dust. I studied the sensitivity of the atmospheric thermal response to the radiative transfer in different CO₂ bands, as well as the sensitivity of the thermal structure to the measured variations of the dust parameters. The developed GCM was applied for studying the baroclinic waves observed in the northern hemisphere of Mars with the purpose of explaining the seasonal changes and the changes associated with the occurrence of planet-encircling dust storms.

Refractive indices in solar wavelengths retrieved by *Ockert-Bell et al.* [1997] are used widely in most Martian GCMs. When simulating with a planet-encircling dust storm, they produce higher than observed daytime temperatures due to larger imaginary values in ultraviolet and visible wavelengths. Another refractive indices profile recently suggested by *Wolff and Clancy* [2003], which is based on the IMP observation by *Tomasko et al.*, [1999] for solar wavelengths as well, produces weaker solar heating, and can modify the simulated daytime temperature by ~10 K during a planet-encircling dust storm.

For the infrared refractive indices, the profile of *Wolff and Clancy* [2003] produces stronger cooling than that of *Toon et al.* [1977] and *Forget* [1998]. As above, the recently

suggested refractive indices profile of *Wolff and Clancy* [2003] gives ~ 15 K colder temperature during a planet-encircling dust storm, compared to the data currently accepted in most Martian GCMs (*Ockert-Bell et al.* [1997], *Toon et al.* [1977] and *Forget* [1998]). It is shown in this study, that the radiative transfer in the CO_2 $4.3 \mu\text{m}$ infrared band affects the thermal structure of the atmosphere insignificantly. Meanwhile, varying the distribution of dust particle sizes strongly influences vertical distributions of heating rates during a planet-encircling dust storm. Thus, the developed GCM can reproduce the observed temperature cross-sections for different dust opacities. Therefore, one can expect that the GCM can realistically simulate the disturbances in the atmosphere as well.

The simulations of the baroclinic waves observed during autumns and winters in the northern hemisphere were performed using the refractive indices profile of *Wolff and Clancy* [2003] and the particle size distribution of *Tomasko et al.* [1999]. Seasonal changes of the waves and their dependence on the dust opacity were investigated. They are fully explained by the changes in the atmospheric thermal structure and the related baroclinic instability. In the weak-dust autumn, the wave with $\text{WN}=2$ and 3.1 Sols period is dominant near the surface, which is consistent with the spectral analysis of the Viking data and the linear instability estimations. The vertical distribution of the amplitudes for $\text{WN}=1$ and $\text{WN}=2$ harmonics are qualitatively consistent with the MGS-TES observations. At higher altitudes, $\text{WN}=1$ component tends to be relatively large, owing to the refractive index distribution.

In the weak-dust winter, the wave with $\text{WN}=1$ and 6.6 Sols period is dominant. The shift of the dominant wavenumber for different seasons can be explained from the seasonal change of the atmospheric fields: the vertical wind shear and stability are stronger in winter than in autumn. These seasonal changes in wave properties and atmospheric fields are qualitatively consistent with the MGS-TES observations. Moreover, the region covered by the negative potential vorticity gradient becomes larger at $\sim 70^\circ$ N in winter, in both the model and the observations. The negative potential vorticity gradient region produces the negative squared refractive index at $\sim 70^\circ$ N. It prevents the waves from propagating northward, and, possibly, helps to generate the waves. As the result, in winter, the amplitude of the $\text{WN}=1$ wave is larger than in autumn, and it less penetrates northward of $\sim 70^\circ$ N, as is consistently seen in both the model and

the observations.

In the strong-dust winter, the wave amplitudes near the surface get significantly smaller, and the waves with $WN=2-4$ become dominant, instead of the $WN=1$ wave in the weak-dust case simulation. This change is qualitatively consistent with the Viking Lander observations, and it was not reproduced in GCM experiments with strong dust opacity before [Barnes *et al.*, 1993]. This success in reproducing the change seems to be because the developed model can reproduce the significant rise of temperature above the north pole consistently with the Viking observations during the winter global dust storm, which Barnes *et al.* [1993] unfortunately failed to do. In our model, the polar warming occurred due to the strong dynamical heating induced by the meridional circulation from the southern hemisphere. It decreases the vertical wind shear and stability near the surface in midlatitudes, and, thus, causes the reduction of baroclinic waves and the increase of the dominant wavenumber. The wave composition (wavenumbers and periods of the dominant waves) is different near the surface and in the upper layers, because it is more difficult for the waves with larger wavenumbers to propagate upward. In the strong-dust autumn, such a reduction of the baroclinic waves does not occur, because the strong dust heating in the south of $\sim 40^\circ$ N and weaker (than in the strong-dust winter) northern polar warming due to the dynamical effects maintain the meridional temperature gradient in the northern midlatitudes.

Appendix A

How to calculate the radiative effects of dust in Martian atmosphere

A.1 Single scattering

The refractive index of a dust particle is defined by the complex number:

$$m = m_r - im_i \quad (\text{A.1})$$

To calculate the Mie scattering means to obtain the solutions of the wave equations for the electric and magnetic fields derived from Maxwell's equations in spherical (r, θ, ϕ) coordinates. Equations for the electric and magnetic field vectors, \mathbf{E} and \mathbf{H} , are as follows:

$$\nabla \times \mathbf{H} = ikm^2 \mathbf{E} \quad (\text{A.2})$$

$$\nabla \times \mathbf{E} = ik\mathbf{H} \quad (\text{A.3})$$

where $k=2\pi/\lambda$ and λ is the wavelength. The three components of the scattered electric and magnetic field vectors, E^s and H^s , at very large distances from the sphere are given by the equations below (see the detailed derivation in [Liou, 2002]).

$$E_r^s = H_r^s \approx 0 \quad (\text{A.4})$$

$$E_\theta^s = H_\phi^s \approx \frac{-i}{kr} e^{-ikr} \cos \phi S_2(\theta) \quad (\text{A.5})$$

$$E_\phi^s = H_\theta^s \approx \frac{i}{kr} e^{-ikr} \sin \phi S_1(\theta) \quad (\text{A.6})$$

where subscripts r , θ and ϕ on E^s and H^s represent the radial, zenithal and azimuthal components of the vectors, respectively. The radial components of the scattered vectors, E_r^s and H_r^s , may be neglected in the far-field zone.

$S_1(\theta)$ and $S_2(\theta)$ in equations (A.5) and (A.6) are the scattering functions defined using the associated Legendre polynomial P_n^1 , as follows.

$$S_1(\theta) = \sum_{n=1}^{\infty} \frac{2n+1}{n(n+1)} \left[a_n \frac{P_n^1(\cos \theta)}{\sin \theta} + b_n \frac{d}{d\theta} P_n^1(\cos \theta) \right] \quad (\text{A.7})$$

$$S_2(\theta) = \sum_{n=1}^{\infty} \frac{2n+1}{n(n+1)} \left[b_n \frac{P_n^1(\cos \theta)}{\sin \theta} + a_n \frac{d}{d\theta} P_n^1(\cos \theta) \right] \quad (\text{A.8})$$

In addition, the coefficients a_n and b_n in equations (A.7) and (A.8) are defined as follows:

$$a_n = \frac{u_n(x)u_n'(y) - mu_n(y)u_n'(x)}{w_n(x)u_n'(y) - mu_n(y)w_n'(x)} \quad (\text{A.9})$$

$$b_n = \frac{mu_n(x)u_n'(y) - u_n(y)u_n'(x)}{mw_n(x)u_n'(y) - u_n(y)w_n'(x)} \quad (\text{A.10})$$

where $x=2\pi a/\lambda$, $y=2\pi ma/\lambda$ with the radius of the particle a , and the functions $u_n(x)$ and $w_n(x)$ are represented using the half-integral-order Bessel function and the Hankel function of the second kind,

$$u_n(x) = \sqrt{\frac{\pi x}{2}} J_{n+\frac{1}{2}}(x) \quad (\text{A.11})$$

$$w_n(x) = \sqrt{\frac{\pi x}{2}} H_{n+\frac{1}{2}}^{(2)}(x) \quad (\text{A.12})$$

and $u_n'(x)$ and $w_n'(x)$ represent $du_n(x)/dx$ and $dw_n(x)/dx$, respectively.

Equations (A.5) and (A.6) represent an outgoing spherical wave where amplitude and the state of polarization are functions of the scattering angle θ . Now we define the perpendicular and parallel components of the electric field as E_r and E_l , respectively. Referring to Figure A1, the scattered perpendicular and parallel electric fields are given as follows.

$$E_r^s = -E_\phi^s \quad (\text{A.13})$$

$$E_l^s = E_\theta^s \quad (\text{A.14})$$

In addition, the normalized incident electric vector, E^i , may be decomposed into perpendicular and parallel components.

$$E_r^i = e^{-ikz} \sin \phi \quad (\text{A.15})$$

$$E_l^i = e^{-ikz} \cos \phi \quad (\text{A.16})$$

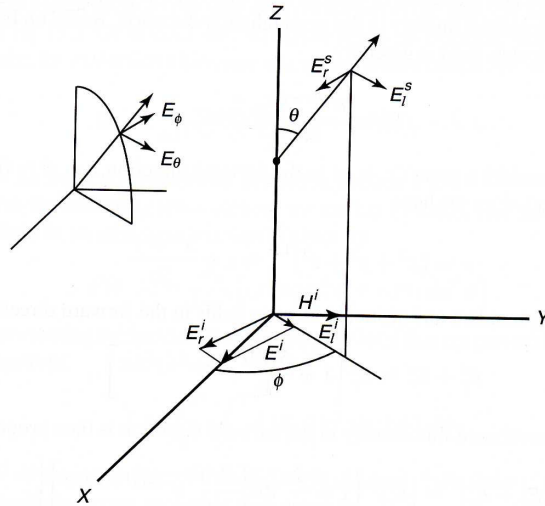


Figure A1: Decomposition of the incident (i) and scattered (s) electric vectors into perpendicular (r) and parallel (l) components in (x,y,z) and (r,θ,ϕ) coordinates [Liou, 2002].

Then equations (A.5) and (A.6) can be expressed as follows.

$$E_l^s = \frac{e^{-ikr+ikz}}{ikr} S_2(\theta) E_l^i \quad (\text{A.17})$$

$$E_r^s = \frac{e^{-ikr+ikz}}{ikr} S_1(\theta) E_r^i \quad (\text{A.18})$$

The extinction cross-section σ_e (unit of m^2) is defined from the far-field combined flux density.

$$\frac{1}{|E_r^i|^2} \iint |E_r^i + E_r^s|^2 dx dy = \pi a^2 + \sigma_e \quad (\text{A.19})$$

In this equation, the first term on the right-hand side represents the cross-section area of the sphere. The physical interpretation of the second term, σ_e , is that the total light received in the forward direction is reduced by the presence of the sphere, and that the amount of this reduction is as if an area equivalent to σ_e is of the object had been covered up. σ_e is calculated using the scattering function in the forward direction $S(0)$ from the optical theorem [e.g. *Shibata*, 1999], as follows:

$$\sigma_e = \frac{4\pi}{k^2} \text{Re}[S(0)] \quad (\text{A.20})$$

where $S(0)$ is given by as follows.

$$S(0) = S_1(0) = S_2(0) = \frac{1}{2} \sum_{n=1}^{\infty} (2n+1)(a_n + b_n) \quad (\text{A.21})$$

The scattered light F in an arbitrary direction (θ, ϕ) is then

$$F(\theta, \phi) = \frac{F_0}{k^2 r^2} \left[|S_1(\theta)|^2 \cos^2 \phi + |S_2(\theta)|^2 \sin^2 \phi \right] \quad (\text{A.22})$$

with F_0 representing the incident flux density. The total flux (or power) of the scattered light f is, therefore,

$$f = \int_0^{2\pi} \int_0^\pi F(\theta, \phi) r^2 \sin \theta d\theta d\phi \quad (\text{A.23})$$

where $\sin \theta d\theta d\phi$ is the differential solid angle $d\Omega$, and $r^2 d\Omega$ denotes the differential area. The scattering cross-section σ_s is then

$$\sigma_s = \frac{f}{F_0} = \frac{\pi}{k^2} \int_0^\pi \left[|S_1(\theta)|^2 + |S_2(\theta)|^2 \right] \sin \theta d\theta, \quad (\text{A.24})$$

And the phase function $P(\theta)$ is represented as follows.

$$P(\theta) = \frac{4\pi}{\sigma_s} \frac{d\sigma_s}{d\Omega} = \frac{2\pi}{k^2 \sigma_s} \left[|S_1(\theta)|^2 + |S_2(\theta)|^2 \right] \quad (\text{A.25})$$

The phase function $P(\theta)$ shows how much energy is scattered to the direction (θ, ϕ) , and the following formula derived from the equation (A.25)

$$\int_0^{2\pi} \int_0^\pi \frac{P(\theta)}{4\pi} \sin \theta d\theta d\phi = 1 \quad (\text{A.26})$$

shows the preservation of energy. This restriction is important for real calculation of the scattering dividing the scattered direction to some areas, which must be satisfied in any cases.

If the refractive index m has the imaginary component, part of the incident wave is absorbed in the scattering body (dust). The absorption cross-section σ_a is the ratio of the absorbed energy and the incident energy, and represented with σ_e and σ_s .

$$\sigma_a = \sigma_e - \sigma_s \quad (\text{A.27})$$

Furthermore, the standardized extinction, scattering and absorption efficiencies without units, Q_e , Q_s and Q_a , respectively, of a sphere with a radius of a are defined as follows.

$$Q_e = \frac{\sigma_e}{\pi a^2} = \frac{2}{x^2} \sum_{n=1}^{\infty} (2n+1) \text{Re}[a_n + b_n] \quad (\text{A.28})$$

$$Q_s = \frac{\sigma_s}{\pi a^2} = \frac{2}{x^2} \sum_{n=1}^{\infty} (2n+1) (|a_n|^2 + |b_n|^2) \quad (\text{A.29})$$

$$Q_a = \frac{\sigma_a}{\pi a^2} = Q_e - Q_s \quad (\text{A.30})$$

Note that the equation (A.29) is evaluated with the orthogonal and recurrence properties of the associated Legendre polynomials.

The single-scattering albedo ω_0 , which shows the degree of scattering, is defined by

$$\omega_0 = \frac{\sigma_s}{\sigma_e} = \frac{Q_s}{Q_e}. \quad (\text{A.31})$$

A.2 Multiple scattering

Now we consider scattering effects in an atmospheric grid which includes multiple particles scattering uniformly. If the mutual distance between particles is more than three times its radius, we can estimate the *independent scattering*, which ignores the scattering effects of neighboring particles and approximates to the simple summary of single scattering effects of each particle [van de Hulst, 1957]. In the case of terrestrial raindrop, cloud particle and aerosols, the mutual distance is large enough to adopt the independent scattering approximation. Therefore, we use it also in the case of dust in Martian atmosphere.

If the distribution of the particle radius per a unit volume [m^{-4}] as $dn(a)/da$, which

means that the number of the particle whose radius is between a and $a+da$ [m] is $dn(a)$ [m^{-3}], the extinction, scattering and absorption coefficients per a unit volume, β_e , β_s and β_a , respectively, are written as follows.

$$\beta_e = \int_0^\infty \sigma_e(a) \frac{dn(a)}{da} da \quad (\text{A.32})$$

$$\beta_s = \int_0^\infty \sigma_s(a) \frac{dn(a)}{da} da \quad (\text{A.33})$$

$$\beta_a = \int_0^\infty \sigma_a(a) \frac{dn(a)}{da} da \quad (\text{A.34})$$

The single-scattering albedo and phase function for multiple scattering are defined as follows.

$$\omega_0 = \frac{\beta_s}{\beta_e} \quad (\text{A.35})$$

$$P(\theta) = \frac{1}{\beta_s} \int_0^\infty \sigma_s(a) P(a, \theta) \frac{dn(a)}{da} da \quad (\text{A.36})$$

The equation (A.36) satisfies the restriction (A.26).

A.3 Evaluation of the optical depth

The optical depth of the atmospheric dust at the height z , $\tau(z)$, is defined via the extinction coefficient per a unit volume:

$$\tau(z) = \int_z^{z_\infty} \beta_e dz \quad (\text{A.37})$$

where z_∞ is the height of the top of atmosphere.

The optical depth can be estimated using the extinction efficiency averaged with the

particle size distribution \bar{Q}_e and the effective radius r_{eff} , which are defined as follows.

$$\bar{Q}_e \equiv \frac{\beta_e}{\int_0^\infty \pi a^2 \frac{dn(a)}{da} da} = \frac{\int_0^\infty Q_e \pi a^2 \frac{dn(a)}{da} da}{\int_0^\infty \pi a^2 \frac{dn(a)}{da} da} \quad (\text{A.38})$$

$$r_{eff} \equiv \frac{\int_0^\infty a^3 \frac{dn(a)}{da} da}{\int_0^\infty a^2 \frac{dn(a)}{da} da} \quad (\text{A.39})$$

Using them, β_e can be expressed as follows.

$$\beta_e = \frac{\bar{Q}_e}{r_{eff}} \int_0^\infty \pi a^3 \frac{dn(a)}{da} da \quad (\text{A.40})$$

Here $\int_0^\infty (4/3)\pi a^3 (dn(a)/da) da$ represents the total volume of dust particles per a unit volume, if the shape of the each particle is assumed to be a sphere. So the equation (A.40) can be rewritten using the density of dust particles ρ_d , density of the atmosphere ρ and the mass mixing ratio of dust in the atmosphere q_d , as follows.

$$\beta_e = \frac{\bar{Q}_e}{r_{eff}} \cdot \frac{3\rho q_d}{4\rho_d} \quad (\text{A.42})$$

From the equation (A.42), the definition of the optical depth (A.37) takes the following form.

$$\tau(z) = \int_z^{z_\infty} \frac{3\bar{Q}_e \rho q_d}{4r_{eff} \rho_d} dz \quad (\text{A.43})$$

Appendix B

History of the Martian GCMs

B.1 Since 1969: Early developments

Studies of the Martian atmosphere using General Circulation Models (GCMs) began with the two-level model of *Leovy and Mintz* [1969]. They successfully adapted the terrestrial GCM of the University of California, Los Angeles (UCLA) to Martian conditions, including only the effects of solar absorption and 15 μ m-band absorption/emission by CO₂ in the radiation scheme, and predicted the atmospheric condensation of CO₂ and the existence of transient baroclinic waves in the winter midlatitudes. After that, *Pollack et al.* [1981] developed a three-layer GCM for the Martian troposphere with a dust-free pure CO₂ atmosphere including the smoothed Martian topography, albedo and CO₂ condensation/sublimation processes, and studied the circulation and atmospheric waves. This model became a framework for the succeeding NASA/Ames Martian GCM, which was used as the simulator for CO₂ polar processes and dynamics in the Martian atmosphere [e.g. *Pollack et al.*, 1990, 1993; *Haberle et al.*, 1993; *Barnes et al.*, 1993, 1996] and for the interpretation of the Mars Pathfinder experiment [*Haberle et al.*, 1999].

Martian GCMs including a dust radiative scheme began with *Moriyama and Iwashima* [1980], and until now, dust radiative schemes as well as the parameterizations of the CO₂ condensation/sublimation became an indispensable part of Martian GCMs.

B.2 In 1990s: Four major Martian GCMs

In 1990s, three Martian GCMs, other than the NASA/Ames, have been developed in

the Laboratory of Dynamic Meteorology in France (LMD), the sub-Department of Atmospheric, Oceanic and Planetary Physics at Oxford University (AOPP) and the in Geophysical Fluid Dynamics Laboratory (GFDL). The LMD Martian GCM was the first to simulate a full Martian year without any forcing other than the insolation and topography [Hourdin *et al.*, 1993, 1995]. It was able to reproduce seasonal and transient pressure variations observed by Viking Landers [Hourdin *et al.*, 1995; Collins *et al.*, 1996]. At almost the same time, another GCM was developed at Oxford University using a spectral solver in conjunction with a simplified set of physical parameterizations. It was originally applied for the investigation of transient baroclinic waves [Collins and James, 1995; Collins *et al.*, 1996] and for the study of the boundary-current nature of the low-level cross-equatorial branch of the Hadley circulation [Joshi *et al.*, 1994]. After the collaboration of LMD and AOPP [Forget *et al.*, 1999; Lewis *et al.*, 1999], they attempted simulations up to 120km. For that, they included a non-LTE CO₂ radiation scheme [Lewis *et al.*, 2001] and validated the results with the past observations including MGS-TES [Forget *et al.*, 2001]. GFDL Martian GCM was used to study the role of thermal tides [Wilson and Hamilton, 1996], to reproduce a winter polar warming [Wilson, 1997] and to re-examine the Viking IRTM temperature observations [Wilson and Richardson, 2000].

B.3 In the 21st century: New attempts and new groups

Since the beginning of the 21st century, new attempts for Martian GCMs have been done. Studies including the Martian water cycle were made with the GFDL [Richardson and Wilson, 2002; Richardson *et al.*, 2002; Mischna *et al.*, 2003] and LMD/AOPP [Montmessin *et al.*, 2004; Böttger *et al.*, 2004, 2005] Martian GCMs. Studies including the parameterization of dust lifting from surface based on the realistic dynamical processes [e.g. Greeley and Iversen, 1985] coupling with the radiatively interactive dust tracer were also performed with the LMD/AOPP [Newman *et al.*, 2002a, 2002b, 2005], NASA/Ames [Haberle *et al.*, 2003; Kahre *et al.*, 2005] and GFDL [Basu *et al.*, 2004] Martian GCMs.

In addition to the three Martian GCMs of 90-ies, new GCMs are being developed.

They include the models from Hokkaido University [*Takahashi et al.*, 2003; 2006], York University (Global Mars Multiscale Model-GM3) [*Moudden and McConnell*, 2005], Center for Climate System Research in University of Tokyo (CCSR/NIES) [*Kuroda et al.*, 2005], and Max-Planck-Institute for Solar System Research (MAOAM-GCM) [*Hartogh et al.*, 2005].

Appendix C

Dust radiation scheme in the GCM

C.1 Radiative transfer equation of the solar radiation

The radiative transfer equation for the solar radiation taking into account the atmospheric emission and scattering is:

$$\begin{aligned} \mu \frac{dI(\tau, \mu, \phi)}{d\tau} = & I(\tau, \mu, \phi) - (1 - \omega)B(\tau) - \frac{\omega}{4\pi} \int_0^{2\pi} \int_{-1}^1 P(\mu, \phi; \mu', \phi') I(\tau, \mu', \phi') d\mu' d\phi' \\ & - \frac{\omega}{4\pi} P(\mu, \phi; -\mu_0, \phi_0) \pi F_0 \exp\left(-\frac{\tau}{\mu_0}\right) \end{aligned} \quad (\text{C.1})$$

where $B(\tau)$ is the Planck function at optical depth τ , ω is the single-scattering albedo, $P(\mu, \phi; \mu', \phi')$ is the phase function for the incident and scattering directions of (μ', ϕ') and (μ, ϕ) (μ is the cosine of the zenith angle and ϕ is the azimuth angle), πF_0 is the solar irradiance, and μ_0 is the cosine of solar zenith angle. At wavelengths of the solar radiation (wavelength $\lambda \leq 4 \mu\text{m}$) the emission from atmosphere is small enough relatively, so the second term of the right side of equation (C.1) can be ignored.

The phase function of the scattering, as the function of the cosine of angle between the incident and scattering directions Θ , can be expanded in the Legendre polynomial series:

$$P(\cos\Theta) = \sum_{n=0}^N (2n+1)g_n P_n(\cos\Theta) = g_0 + 3g_1 \cos\Theta + \frac{5}{2}g_2(3\cos^2\Theta - 1) + \dots \quad (\text{C.2})$$

$$g_n = \frac{1}{2} \int_{-1}^1 P(\cos\Theta) P_n(\cos\Theta) d\cos\Theta \quad (\text{C.3})$$

The value of g_n depends on the phase function. First, $g_0=1$ is given automatically from the restriction described with the equation (A.26), i.e.:

$$\int_0^{2\pi} \int_0^\pi P(\cos \Theta) \sin \Theta d\Theta d\phi = 2\pi \int_{-1}^1 P(\mu) d\mu = 4\pi \quad (C.4)$$

where $\mu=\cos\Theta$.

$\cos\Theta$ is written using spherical trigonometry as follows.

$$\cos \Theta = \mu\mu' + \sqrt{1-\mu^2} \sqrt{1-\mu'^2} \cos(\phi - \phi') \quad (C.5)$$

From equations (C.2) and (C.5) and using addition theorem of Legendre function, $P(\mu, \phi; \mu', \phi')$ has the form:

$$\begin{aligned} P(\mu, \phi; \mu', \phi') &= \sum_{n=0}^N \sum_{m=0}^n (2 - \delta_{0,m}) (2n+1) g_n \frac{(n-m)!}{(n+m)!} P_n^m(\mu) P_n^m(\mu') \cos m(\phi - \phi') \\ &= \sum_{m=0}^N \sum_{n=m}^N (2 - \delta_{0,m}) (2n+1) g_n \frac{(n-m)!}{(n+m)!} P_n^m(\mu) P_n^m(\mu') \cos m(\phi - \phi') \quad (C.6) \end{aligned}$$

where $\delta_{0,m}$ is the Kronecher's delta and $P_n^m(\mu, \phi)$ is the associated Legendre function.

The cosine expansion of the radiance $I(\tau, \mu, \phi)$ in azimuth angles is as follows.

$$I(\tau, \mu, \phi) = \sum_{m=0}^N I^m(\tau, \mu) \cos m(\phi - \phi_0) \quad (C.7)$$

Substituting equations (C.6) and (C.7) for equation (C.1) without the emission term and integrating this for azimuth angle, $(N+1)$ independent equations for radiative transfer ($m=0, 1, \dots, N$) can be obtained.

$$\begin{aligned}
\mu \frac{dI^m(\tau, \mu)}{d\tau} &= I^m(\tau, \mu) \\
&- (1 + \delta_{0,m}) \frac{\omega}{4} \sum_{n=m}^N (2 - \delta_{0,m})(2n+1) g_n \frac{(n-m)!}{(n+m)!} P_n^m(\mu) \int_{-1}^1 P_n^m(\mu') I^m(\tau, \mu') d\mu' \\
&- \frac{\omega}{4\pi} \sum_{n=m}^N (2 - \delta_{0,m})(2n+1) g_n \frac{(n-m)!}{(n+m)!} P_n^m(\mu) P_n^m(-\mu_0) \pi F_0 \exp\left(-\frac{\tau}{\mu_0}\right) \quad (C.8)
\end{aligned}$$

Note that $\int_0^{2\pi} \cos m(\phi - \phi') \cos m(\phi' - \phi_0) d\phi'$ equals 2π if $m=0$, and equals $\pi \cos m(\phi - \phi_0)$ if $m \neq 0$.

The upward and downward fluxes are the sum of radiance which is vertical of the layer, so the fluxes F_{DIF}^\pm are written as follows.

$$F_{DIF}^\pm = \int_0^{2\pi} \int_0^1 I(\tau, \pm\mu, \phi) \mu d\mu d\phi \quad (C.9)$$

Substituting equation (C.7) for equation (C.9) and integrating this for azimuth angle, all the terms with $m \neq 0$ become zero and the result is as follows.

$$F_{DIF}^\pm = \int_0^1 I^0(\tau, \pm\mu) \mu d\mu \quad (C.10)$$

Thus, we can consider only the case of $m=0$ to calculate the heating rates. Then equation (C.8) can be rewritten as follows (writing $I^0(\tau, \mu)$ as $I(\tau, \mu)$).

$$\begin{aligned}
\mu \frac{dI(\tau, \mu)}{d\tau} &= I(\tau, \mu) - \frac{\omega}{2} \sum_{n=m}^N (2n+1) g_n P_n(\mu) \int_{-1}^1 P_n(\mu') I(\tau, \mu') d\mu' \\
&- \frac{\omega}{4\pi} \sum_{n=m}^N (2n+1) g_n P_n(\mu) P_n(-\mu_0) \pi F_0 \exp\left(-\frac{\tau}{\mu_0}\right) \quad (C.11)
\end{aligned}$$

Using equation (C.6) and defining the phase function without depending on azimuth angle $P(\mu, \mu')$

$$P(\mu, \mu') = \frac{1}{2\pi} \int_0^{2\pi} P(\mu, \phi; \mu', \phi') d(\phi - \phi'), \quad (\text{C.12})$$

equation (C.11) yields

$$\mu \frac{dI(\tau, \mu)}{d\tau} = I(\tau, \mu) - \frac{\omega}{2} \int_{-1}^1 P(\mu, \mu') I(\tau, \mu') d\mu' - \frac{\omega}{4\pi} P(\mu, -\mu_0) \pi F_0 \exp\left(-\frac{\tau}{\mu_0}\right). \quad (\text{C.13})$$

This is the radiative transfer equation, which is used to calculate the heating rates due to the solar radiation.

C.2 δ -Eddington approximation of the phase function (Joseph et al., 1976)

To define the phase function of atmospheric dust, the δ -Eddington approximation is used. Here we use the equation (C.2) as $N=2$, and use g_1 as the asymmetry parameter ($=g$) and g_2 as the parameter of the fractional scattering into the forward peak ($=f$).

In the δ -Eddington approximation, the phase function is represented using delta function and f :

$$P(\cos \theta) \approx P_{\delta\text{-Edd}}(\cos \theta) \equiv 2f\delta(1 - \cos \theta) + (1 - f)(1 + 3g'\cos \theta) \quad (\text{C.14})$$

where g' is the asymmetry factor of the truncated phase function. This function satisfies the restriction of equation (C.4).

$$\int_0^{2\pi} \int_0^\pi P_{\delta\text{-Edd}}(\cos \theta) \sin \theta d\theta d\phi = 2\pi \int_{-1}^1 P_{\delta\text{-Edd}}(\mu) d\mu = 2\pi \{2f + 2(1 - f)\} = 4\pi \quad (\text{C.15})$$

We further require $P_{\delta\text{-Edd}}$ to have the same asymmetry factor (g) as the original phase function:

$$g = \frac{1}{2} \int_{-1}^1 \mu P_{\delta-Edd}(\mu) d\mu = f + (1-f)g' \quad (C.16)$$

from which g' is determined as follows.

$$g' = \frac{g-f}{1-f} \quad (C.17)$$

Finally, to determine f which is represented by the second moment of $P_{\delta-Edd}$, i.e.:

$$\frac{1}{2} \int_{-1}^1 P_2(\mu) P_{\delta-Edd}(\mu) d\mu = f. \quad (C.18)$$

We approximate the original phase function by the Henyey-Greenstain phase function, which is used in place of the more realistic function from the Mie theory for flux computations [van de Hulst, 1968; Hansen, 1969]. The Henyey-Greenstain phase function is defined as follows.

$$P(\cos \theta) \approx P_{H-G}(\cos \theta) \equiv \frac{1-g^2}{(1+g^2-2g \cos \theta)^{3/2}} \quad (C.19)$$

The second moment of P_{H-G} is calculated as follows.

$$\frac{1}{2} \int_{-1}^1 P_2(\mu) P_{H-G}(\mu) d\mu = g^2 \quad (C.20)$$

So by identifying equation (C.20) with equation (C.7), we require

$$f = g^2 \quad (C.21)$$

and therefore

$$g' = \frac{g}{1+g} \quad (\text{C.22})$$

from equation (C.17).

Using the approximated phase function $P_{\delta\text{-Edd}}$, the radiative transfer equation (equations (C.12) and (C.13)) is written as follows.

$$\begin{aligned} \mu \frac{dI(\tau, \mu)}{d\tau} &= I(\tau, \mu) - \frac{\omega}{4\pi} \int_{-1}^1 \int_0^{2\pi} P_{\delta\text{-Edd}}(\mu, \phi; \mu', \phi') I(\tau, \mu') d(\phi - \phi') d\mu' \\ &\quad - \frac{\omega}{8\pi^2} \int_0^{2\pi} P_{\delta\text{-Edd}}(\mu, \phi; -\mu_0, \phi_0) d(\phi - \phi_0) \pi F_0 \exp\left(-\frac{\tau}{\mu_0}\right) \end{aligned} \quad (\text{C.23})$$

When Θ is the angle between the incident and scattering directions, (μ', ϕ') and (μ, ϕ) , the following equation about the delta function is formed.

$$\delta(1 - \cos \Theta) = 2\pi \delta(\mu - \mu') \delta(\phi - \phi') \quad (\text{C.24})$$

From equations (C.5) and (C.24), equation (C.23) is rewritten as follows.

$$\begin{aligned} \mu \frac{dI(\tau, \mu)}{d\tau} &= I(\tau, \mu) - \frac{\omega}{2} \int_{-1}^1 \{2f\delta(\mu - \mu') + (1-f)(1+3g'\mu\mu')\} I(\tau, \mu') d\mu' \\ &\quad - \frac{\omega}{4\pi} \{2f\delta(\mu + \mu_0) + (1-f)(1-3g'\mu\mu_0)\} \pi F_0 \exp\left(-\frac{\tau}{\mu_0}\right) \end{aligned} \quad (\text{C.25})$$

$$\begin{aligned} &= (1 - \omega f) I(\tau, \mu) - \frac{(1-f)\omega}{2} \int_{-1}^1 (1+3g'\mu\mu') I(\tau, \mu') d\mu' \\ &\quad - \frac{(1-f)\omega}{4\pi} (1-3g'\mu\mu_0) \pi F_0 \exp\left(-\frac{\tau}{\mu_0}\right) \quad (\mu \neq -\mu_0) \end{aligned} \quad (\text{C.26})$$

Here we define τ' as the transformed optical depth by the δ -Eddington approximation as follows,

$$\tau' = (1 - \omega f)\tau = (1 - \omega g^2)\tau \quad (\text{C.27})$$

and equation (C.26) is rewritten using τ' as follows:

$$\begin{aligned} \mu \frac{dI(\tau', \mu)}{d\tau'} &= I(\tau', \mu) - \frac{\omega'}{2} \int_{-1}^1 (1 + 3g' \mu \mu') I(\tau', \mu') d\mu' \\ &\quad - \frac{\omega'}{4\pi} (1 - 3g' \mu \mu_0) \pi F_0 \exp\left(-\frac{\tau'}{\mu_0}\right) \end{aligned} \quad (\text{C.28})$$

where ω' is defined as follows.

$$\omega' = \frac{(1-f)\omega}{1-\omega f} = \frac{(1-g^2)\omega}{1-\omega g^2} \quad (\text{C.29})$$

Note that in equation (C.28) τ in the third term of the right side (for calculating direct solar flux) is also replaced by τ' .

If we define $P'(\mu, \mu')$ as

$$P'(\mu, \mu') = \frac{1}{2\pi} \int_0^{2\pi} P'(\cos\Theta) d(\phi - \phi') \quad (\text{C.30})$$

$$P'(\cos\Theta) = \sum_{n=0}^1 (2n+1) g_n' P_n(\cos\Theta) \quad (\text{C.31})$$

where $g_0'=1$ and $g_1'=g'$, equation (C.28) can be rewritten as follows, which is the same form as equation (C.13), using τ' , ω' and $P'(\mu, \mu')$.

$$\mu \frac{dI(\tau', \mu)}{d\tau'} = I(\tau', \mu) - \frac{\omega'}{2} \int_{-1}^1 P'(\mu, \mu') I(\tau', \mu') d\mu' - \frac{\omega'}{4\pi} P'(\mu, -\mu_0) \pi F_0 \exp\left(-\frac{\tau'}{\mu_0}\right) \quad (\text{C.32})$$

C.3 Calculation of the reflectivity, transmissivity and radiative source functions of the layer (two-stream DOM method, Nakajima and Tanaka, 1986; Nakajima et al., 2000)

For calculating the fluxes in each band, we define R and T , reflectivity and transmissibility of a homogeneous layer optical thickness of which (transformed by equation (C.27)) is $\Delta\tau'$, using two-stream DOM approximation. The optical thickness of the layer $\Delta\tau$ (before transformation by equation (C.27)) is written from the equation (A.43):

$$\Delta\tau = \frac{3Q_e \rho q_d}{4r_{eff} \rho_d} \Delta z \quad (C.33)$$

where Q_e is the extinction efficiency of dust, ρ is the atmospheric density, q_d is the mass mixing ratio of dust, r_{eff} is the effective radius of dust, ρ_d is the dust density and Δz is the width of the layer. In this scheme we define that $r_{eff}=1.60 \times 10^{-6}$ m except for the special setting in Chapter 3, and $\rho_d=2.65 \times 10^3$ kg m⁻³.

The standardized phase functions of scattering are defined from the second term of the right side of equation (C.32), as follows:

$$\hat{P}^\pm = \frac{\omega'}{2\mu_1} P'(\pm\mu_1, \mu_1) = \frac{\omega'}{2\mu_1} (1 \pm 3g'\mu_1^2) \quad (C.34)$$

where μ_1 is the cosine of direction for two-stream approximation, and $\mu_1=1/\sqrt{3}$ is defined for the solar (short-wave) radiation from the delta two-stream Gaussian approximation [Goody and Yung, 1989].

Here the factors X and Y are defined as follows.

$$X = \frac{1}{\mu_1} - (\hat{P}^+ - \hat{P}^-) = \frac{1 - 3\omega'g'\mu_1^2}{\mu_1} \quad (C.35)$$

$$Y = \frac{1}{\mu_1} - (\hat{P}^+ + \hat{P}^-) = \frac{1 - \omega'}{\mu_1} \quad (\text{C.36})$$

Using X and Y , R and T are written as follows:

$$R = \frac{Z(1 + e^{-\sqrt{XY}\Delta\tau'}) - (1 - e^{-\sqrt{XY}\Delta\tau'})}{Z(1 + e^{-\sqrt{XY}\Delta\tau'}) + (1 - e^{-\sqrt{XY}\Delta\tau'})} + \frac{Z(1 - e^{-\sqrt{XY}\Delta\tau'}) - (1 + e^{-\sqrt{XY}\Delta\tau'})}{Z(1 - e^{-\sqrt{XY}\Delta\tau'}) + (1 + e^{-\sqrt{XY}\Delta\tau'})} \quad (\text{C.37})$$

$$T = \frac{Z(1 + e^{-\sqrt{XY}\Delta\tau'}) - (1 - e^{-\sqrt{XY}\Delta\tau'})}{Z(1 + e^{-\sqrt{XY}\Delta\tau'}) + (1 - e^{-\sqrt{XY}\Delta\tau'})} - \frac{Z(1 - e^{-\sqrt{XY}\Delta\tau'}) - (1 + e^{-\sqrt{XY}\Delta\tau'})}{Z(1 - e^{-\sqrt{XY}\Delta\tau'}) + (1 + e^{-\sqrt{XY}\Delta\tau'})} \quad (\text{C.38})$$

where $Z = \sqrt{\frac{X}{Y}} = \sqrt{\frac{1 - 3\omega'g'\mu_1^2}{1 - \omega'}}$.

The third term in the right-hand side of (C.32) represents the radiative source function derived from the solar insolation. Now we define the upward and downward source functions ε_s^\pm (Note that + means upward and - means downward). The standardized phase functions of scattering for the solar insolation are defined from the second term of the right side of (C.32):

$$\hat{\sigma}_s^\pm = \frac{\omega'}{2\sqrt{\mu_1}} \{P'(-\mu_1, -\mu_0) \mp P'(\mu_1, -\mu_0)\} \quad (\text{C.39})$$

In fact, $\hat{\sigma}_s^+ = \frac{3\omega'g'\mu_1\mu_0}{\sqrt{\mu_1}}$ and $\hat{\sigma}_s^- = \frac{\omega'}{\sqrt{\mu_1}}$. And the factors V_s^\pm are defined as follows.

$$V_s^\pm = \frac{1}{2} \left[\left(1 \pm \frac{1}{X\mu_0} \right) \frac{\hat{\sigma}_s^+ + \hat{\sigma}_s^- X\mu_0}{XY\mu_0 - 1/\mu_0} \pm \frac{\hat{\sigma}_s^+}{X} \right] \quad (\text{C.40})$$

Using V_s^\pm , ε_s^\pm are written as follows:

$$\varepsilon_s^+ = \left[V_s^+ - RV_s^- - TV_s^+ \exp\left(-\frac{\Delta\tau'}{\mu_0}\right) \right] \exp\left(-\frac{\tau^*}{\mu_0}\right) \pi F_0 \quad (\text{C.41})$$

$$\varepsilon_s^- = \left[V_s^- \exp\left(-\frac{\Delta\tau'}{\mu_0}\right) - TV_s^- - RV_s^+ \exp\left(-\frac{\Delta\tau'}{\mu_0}\right) \right] \exp\left(-\frac{\tau^*}{\mu_0}\right) \pi F_0 \quad (\text{C.42})$$

where τ^* is the summary of the transformed optical thickness from the top of atmosphere to the top boundary of the layer. In other words, τ^* is the optical depth at the top boundary of the layer, which is transformed by equation (C.27), and we can also say that $\tau^* + \Delta\tau'$ is the transformed optical depth at the bottom boundary of the layer.

The solar irradiance πF_0 is set as follows:

$$\pi F_0 = I_0 \left(\frac{r_0}{r} \right)^2 \quad (\text{C.43})$$

where I_0 is the averaged solar incidence on the orbit of Mars (589.2 W m^{-2}), r is the Sun-Mars distance, and r_0 is the mean value of r .

C.4 Infrared radiation

At wavelengths of the infrared radiation (wavelength $\lambda \geq 4 \mu\text{m}$), the solar radiation term, the fourth term in the right-hand side of (C.1), can be ignored. Instead, the emission from the atmosphere, the second term in the right-hand side of (C.1), should be considered. Then, the radiative transfer equation for infrared radiation can be written as follows, replacing the third term in the right-hand side of (C.13).

$$\mu \frac{dI(\tau, \mu)}{d\tau} = I(\tau, \mu) - \frac{\omega}{2} \int_{-1}^1 P(\mu, \mu') I(\tau, \mu') d\mu' - (1 - \omega) B(\tau) \quad (\text{C.44})$$

Of course this can be rewritten using τ' , ω' and $P(\mu, \mu')$, defined in equations (C.27), (C.29) and (C.30), as follows.

$$\mu \frac{dI(\tau', \mu)}{d\tau'} = I(\tau', \mu) - \frac{\omega'}{2} \int_{-1}^1 P'(\mu, \mu') I(\tau', \mu') d\mu' - (1 - \omega') B(\tau') \quad (\text{C.45})$$

The fluxes are calculated from this equation using the two-stream DOM approximation and adding method, as already mentioned in Section 3. For the infrared radiation, μ_1 in (C.34) is defined as $\mu_1=1/1.66$ from the diffusive-factor approximation [Goody and Yung, 1989]. The diffusive-factor value of 1.66 was first proposed by Elsasser in 1942. The consensus of many studies is that the errors of thus calculated heating rates do not exceed 2%.

The upward and downward radiative source functions from Planck function, ε_a^\pm , should be calculated from the third term of the right side of equation (C.45). First, Planck function of the layer is expanded in quadratic polynomial of optical depth as follows:

$$B(\tau) = \sum_{n=0}^2 b_n \tau^n = b_0 + b_1 \tau + b_2 \tau^2 \quad (\text{C.46})$$

where the expansion coefficients, b_0 , b_1 and b_2 , are calculated using the following equations:

$$b_0 = B(0) \quad (\text{C.47})$$

$$b_1 = \frac{4B(\Delta\tau/2) - B(\Delta\tau) - 3B(0)}{\Delta\tau'} \quad (\text{C.48})$$

$$b_2 = \frac{2[B(\Delta\tau) + B(0) - 2B(\Delta\tau/2)]}{(\Delta\tau')^2} \quad (\text{C.49})$$

where $B(0)$, $B(\Delta\tau)$ and $B(\Delta\tau/2)$ are the Planck function of top boundary, bottom boundary and middle of the layer, respectively. Because the Planck function is a function of wavelength and temperature, if the Planck function is written as $B_\lambda(T)$ they are calculated as follows:

$$B(0) = B_\lambda \left(\frac{T_l + T_{l+1}}{2} \right) \quad (\text{C.50})$$

$$B(\Delta\tau/2) = B_\lambda(T_l) \quad (\text{C.51})$$

$$B(\Delta\tau) = B_\lambda \left(\frac{T_l + T_{l-1}}{2} \right) \quad (\text{C.52})$$

where T_l is the temperature of the l th layer. $B(0)$ at the top layer and $B(\Delta\tau)$ at the bottom layer are set to be equal to $B(\Delta\tau/2)$ in each layer.

Next, the expansion coefficients of the radiative source functions are calculated as follows.

$$\hat{b}_n = \frac{2\pi(1-\omega')}{\sqrt{\mu_1}} b_n \quad (n=0, 1, 2) \quad (\text{C.53})$$

$$D_0^\pm = \frac{\hat{b}_0}{Y} \pm \frac{\hat{b}_1}{XY} + \frac{2\hat{b}_2}{XY^2} \quad (\text{C.54})$$

$$D_1^\pm = \frac{\hat{b}_1}{Y} \pm \frac{2\hat{b}_2}{XY} \quad (\text{C.55})$$

$$D_2 = \frac{\hat{b}_2}{Y} \quad (\text{C.56})$$

Using these coefficients, emissions at the top and bottom of the layer are calculated as follows.

$$D^\pm(0) = D_0^\pm \quad (\text{C.57})$$

$$D^\pm(\Delta\tau') = D_0^\pm + D_1^\pm \Delta\tau' + D_2(\Delta\tau')^2 \quad (\text{C.58})$$

Finally, radiative source functions from Planck function are written as follows.

$$\varepsilon_a^+ = D^+(0) - RD^-(0) - TD^+(\Delta\tau') \quad (\text{C.59})$$

$$\varepsilon_a^- = D^-(\Delta\tau') - TD^-(0) - RD^+(\Delta\tau') \quad (\text{C.60})$$

The summaries of the radiative source functions (from the solar insolation and the Planck function) are represented using two equations above and ε_s^\pm in equations (C.41) and (C.42), and these functions are used to calculate the fluxes in next section (Usually, only either ε_s^\pm or ε_a^\pm has the value in each band).

$$\varepsilon^\pm = \varepsilon_s^\pm + \varepsilon_a^\pm \quad (\text{C.61})$$

C.5 Calculation of fluxes (adding method)

From the reflectivity, transmissivity and radiative source functions calculated above, we can calculate the radiative fluxes and also the heating rates by the fluxes.

In the inhomogeneous layer, the values of the reflectivity and transmissibility of downward insolation, R^- and T^- , are different from those of upward insolation, R^+ and T^+ . In the case that these values of l th layer, R_l^\pm and T_l^\pm , and those of the upper adjacent layer ($(l+1)$ th layer), R_{l+1}^\pm and T_{l+1}^\pm , are known from equations (C.37) and (C.38), those of the combination of these two layers, $R_{l,l+1}^\pm$ and $T_{l,l+1}^\pm$, are calculated using adding method as follows.

$$\begin{aligned} R_{l,l+1}^+ &= R_l^+ + T_l^+ R_{l+1}^+ T_l^- + T_l^+ R_{l+1}^+ R_l^- R_{l+1}^+ T_l^- + \dots \\ &= R_l^+ + T_l^+ R_{l+1}^+ (1 + R_l^- R_{l+1}^+ + R_l^{-2} R_{l+1}^{+2} + \dots) T_l^- = R_l^+ + \frac{T_l^+ R_{l+1}^+ T_l^-}{1 - R_l^- R_{l+1}^+} \end{aligned} \quad (\text{C.62})$$

$$\begin{aligned} T_{l,l+1}^+ &= T_l^+ T_{l+1}^+ + T_l^+ R_{l+1}^+ R_l^- T_{l+1}^+ + T_l^+ R_{l+1}^+ R_l^- R_{l+1}^+ R_l^- T_{l+1}^+ + \dots \\ &= T_l^+ (1 + R_l^- R_{l+1}^+ + R_l^{-2} R_{l+1}^{+2} + \dots) T_{l+1}^+ = \frac{T_l^+ T_{l+1}^+}{1 - R_l^- R_{l+1}^+} \end{aligned} \quad (\text{C.63})$$

$$\begin{aligned} R_{l,l+1}^- &= R_{l+1}^- + T_{l+1}^- R_l^- T_{l+1}^+ + T_{l+1}^- R_l^- R_{l+1}^+ R_l^- T_{l+1}^+ + \dots \\ &= R_{l+1}^- + T_{l+1}^- (1 + R_l^- R_{l+1}^+ + R_l^{-2} R_{l+1}^{+2} + \dots) R_l^- T_{l+1}^+ = R_{l+1}^- + \frac{T_{l+1}^- R_l^- T_{l+1}^+}{1 - R_l^- R_{l+1}^+} \end{aligned} \quad (\text{C.64})$$

$$\begin{aligned}
T_{l,l+1}^- &= T_{l+1}^- T_l^- + T_{l+1}^- R_l^- R_{l+1}^+ T_l^- + T_{l+1}^- R_l^- R_{l+1}^+ R_l^- R_{l+1}^+ T_l^- + \dots \\
&= T_{l+1}^- (1 + R_l^- R_{l+1}^+ + R_l^{-2} R_{l+1}^{+2} + \dots) T_l^- = \frac{T_{l+1}^- T_l^-}{1 - R_l^- R_{l+1}^+} \quad (C.65)
\end{aligned}$$

Radiative source functions of the combination of l th and $(l+1)$ th layers, $\varepsilon_{l,l+1}^\pm$, are also calculated from source functions of these two layers, ε_l^\pm and ε_{l+1}^\pm , using adding methods as follows.

$$\begin{aligned}
\varepsilon_{l,l+1}^+ &= \varepsilon_{l+1}^+ + (1 + R_l^- R_{l+1}^+ + R_l^{-2} R_{l+1}^{+2} + \dots) T_{l+1}^+ \varepsilon_l^+ + R_l^- (1 + R_l^- R_{l+1}^+ + R_l^{-2} R_{l+1}^{+2} + \dots) T_{l+1}^+ \varepsilon_{l+1}^- \\
&= \varepsilon_{l+1}^+ + \frac{T_{l+1}^+ (\varepsilon_l^+ + R_l^- \varepsilon_{l+1}^-)}{1 - R_l^- R_{l+1}^+} \quad (C.66)
\end{aligned}$$

$$\begin{aligned}
\varepsilon_{l,l+1}^- &= \varepsilon_l^- + (1 + R_l^- R_{l+1}^+ + R_l^{-2} R_{l+1}^{+2} + \dots) T_l^- \varepsilon_{l+1}^- + R_{l+1}^+ (1 + R_l^- R_{l+1}^+ + R_l^{-2} R_{l+1}^{+2} + \dots) T_l^- \varepsilon_l^+ \\
&= \varepsilon_l^- + \frac{T_l^- (\varepsilon_{l+1}^- + R_{l+1}^+ \varepsilon_l^+)}{1 - R_l^- R_{l+1}^+} \quad (C.67)
\end{aligned}$$

When the number of layers in the GCM is N , the fluxes at the n th boundary ($0 \leq n \leq N$, $n=0$ at the surface and $n=N$ at the top of the atmosphere), F_n^{\uparrow} and F_n^{\downarrow} , are written as follows, if $0 \leq n \leq N-1$:

$$\begin{aligned}
F_n^{\uparrow} &= (1 + R_{0,n}^- R_{n+1,N}^+ + R_{0,n}^{-2} R_{n+1,N}^{+2} + \dots) \varepsilon_{0,n}^+ + R_{0,n}^- (1 + R_{0,n}^- R_{n+1,N}^+ + R_{0,n}^{-2} R_{n+1,N}^{+2} + \dots) \varepsilon_{n+1,N}^- \\
&= \frac{\varepsilon_{0,n}^+ + R_{0,n}^- \varepsilon_{n+1,N}^-}{1 - R_{0,n}^- R_{n+1,N}^+} \quad (C.68)
\end{aligned}$$

$$\begin{aligned}
F_n^{\downarrow} &= (1 + R_{0,n}^- R_{n+1,N}^+ + R_{0,n}^{-2} R_{n+1,N}^{+2} + \dots) \varepsilon_{n+1,N}^- + R_{n+1,N}^+ (1 + R_{0,n}^- R_{n+1,N}^+ + R_{0,n}^{-2} R_{n+1,N}^{+2} + \dots) \varepsilon_{0,n}^+ \\
&= \frac{\varepsilon_{n+1,N}^- + R_{n+1,N}^+ \varepsilon_{0,n}^+}{1 - R_{0,n}^- R_{n+1,N}^+} \quad (C.69)
\end{aligned}$$

where

$$R_{n+1,N}^+ = R_{n+1}^+ + T_{n+1}^+ R_{n+2,N}^+ (1 + R_{n+1}^- R_{n+2,N}^+ + R_{n+1}^{-2} R_{n+2,N}^{+2} + \dots) T_{n+1}^- = R_{n+1}^+ + \frac{T_{n+1}^+ R_{n+2,N}^+ T_{n+1}^-}{1 - R_{n+1}^- R_{n+2,N}^+} \quad (\text{C.70})$$

$$R_{0,n}^- = R_n^- + T_n^- (1 + R_{0,n-1}^- R_n^+ + R_{0,n-1}^{-2} R_n^{+2} + \dots) R_{0,n-1}^- T_n^+ = R_n^- + \frac{T_n^- R_{0,n-1}^- T_n^+}{1 - R_{0,n-1}^- R_n^+} \quad (\text{C.71})$$

$$\varepsilon_{0,n}^+ = \varepsilon_n^+ + \frac{T_n^+ (\varepsilon_{0,n-1}^+ + R_{0,n-1}^- \varepsilon_n^-)}{1 - R_{0,n-1}^- R_n^+} \quad (\text{C.72})$$

$$\varepsilon_{n+1,N}^- = \varepsilon_{n+1}^- + \frac{T_{n+1}^- (\varepsilon_{n+2,N}^- + R_{n+2,N}^+ \varepsilon_{n+1}^+)}{1 - R_{n+1}^- R_{n+2,N}^+} \quad (\text{C.73})$$

with boundary conditions at the surface:

$$R_{0,0}^- = 2\mu_1 A \quad (\text{C.74})$$

$$\varepsilon_{0,0}^+ = \sqrt{\mu_1} \left[2A\mu_0 \pi F_0 \exp\left(-\frac{\tau_{0,N}^*}{\mu_0}\right) + 2\pi(1-A)B_\lambda(T_{sfc}) \right] \quad (\text{C.75})$$

where $\tau_{n,N}^*$ is the summary of the transformed optical depth from the n th layer ($0 \leq n \leq N-1$, $n=0$ represents the bottom layer and $n=N-1$ the top layer) to the top layer, i.e. $\tau_{0,N}^*$ is the transformed optical depth at the surface and $\tau_{N,N}^*$ equals zero, $B_\lambda(T_{sfc})$ is the Planck function at the surface and A is the surface albedo.

F_N^{\uparrow} and F_N^{\downarrow} (fluxes at the top of atmosphere) are defined as follows.

$$F_N^{\uparrow} = \varepsilon_{0,N}^+ \quad (\text{C.76})$$

$$F_N^{\downarrow} = 0 \quad (\text{C.77})$$

Because F_n^{\uparrow} and F_n^{\downarrow} are the scaled flux, we re-scale the fluxes, and finally add the direct solar insolation to the downward flux as follows.

$$F_n^\uparrow = \sqrt{\mu_1} F_n^{\prime\uparrow} \quad (\text{C.78})$$

$$F_n^\downarrow = \sqrt{\mu_1} F_n^{\prime\downarrow} + \mu_0 \pi F_0 \exp\left(-\frac{\tau_{n,N}^*}{\mu_0}\right) \quad (\text{C.79})$$

C.6 Calculation of the heating/cooling rates of atmosphere

The heating/cooling rate of atmosphere in the n th layer, $(dT/dt)_n$, is calculated using the summary of F^\uparrow and F^\downarrow in equations (C.78) and (C.79) in each band, as follows:

$$\left(\frac{dT}{dt}\right)_{n,} = \frac{1}{\rho c_p \Delta z} \left[\sum_{\Delta\nu} (F_{n+1}^\downarrow - F_n^\downarrow + F_n^\uparrow - F_{n+1}^\uparrow) \right] \quad (\text{C.80})$$

where $\Delta\nu$ represents the each band and c_p is the atmospheric specific heat at constant pressure.

Appendix D

Why the experiment without CO₂ 15 μ m radiation shows higher temperature?

One might think that, if the CO₂ infrared radiation was turned off, the simulated atmospheric temperature would be colder than in simulations with this radiation included, because of the absence of the daytime ‘greenhouse’ effect. However, in our experiment, the higher temperature was obtained when this radiation had been turned off. The explanation for this is given below.

For this, additional diagnostics of the model output were done to analyze the temperature balance. Using the saved restart file with the initial conditions at $L_s=210^\circ$ after the run for the plots in Figures 20-23, the model was run for 1 day and the snapshots were analyzed. In the first experiment, all the CO₂ infrared radiation was turned on as in the standard simulations (hereafter 15ON). In the second experiment, all the CO₂ infrared radiative effects including the 15 μ m band were turned off (15OFF). As described in Subsection 3.1.3, the effects of the CO₂ 4.3 μ m and 10 μ m bands are very small. Therefore, this sensitivity test may be regarded as the sensitivity to the CO₂ 15 μ m band only. All other conditions are essentially the same as in the runs for the ‘weak-dust’ (TES2 dust scenario) case, ‘Refractive A’ and ‘PSD 1’. The zonal-mean (averaged at the day and night local times) heating/cooling rates due to various effects for both experiments are plotted in Figures D1 and D2. Note that the vertical axis is σ -level, as well as all the figures to follow in this appendix.

In the 15ON experiment (Figure D1), the strong heating near the surface in Figure D1a manifests the daytime ‘greenhouse’ effect. As described in Subsection 3.1.1, this strong heating is compensated by the vertical diffusion (mostly in the lowest part of the

atmosphere) and by dry convective adjustment somewhat higher (see Figure D1b), and the diffusion and convection transport the excessive heat upward. The dynamical contribution (advection and adiabatic heating/cooling) is small compared to the above mentioned mechanisms, as seen in Figure D1c. The total temperature tendency is shown in Figure D1d.

Meanwhile, the CO₂ 15μm band contributes to the cooling of the atmosphere. Figure D3 shows the longitude (i.e. local time) variance of the diabatic heating/cooling rate at the equator in 15ON and 15OFF experiments. As seen in the comparison, the heating due to the ‘greenhouse’ effect is limited below $\sigma \sim 0.8$ and the local time between ~ 0800 and ~ 1600 . This causes that the cooling effect exceeds the daytime ‘greenhouse’ effect when averaged over all local times, except immediately above the surface, as seen in Figure D1a. In the 15OFF experiment, the net radiative effect is a moderate heating (due to the absorption of the solar radiation by CO₂ and dust), as seen in Figures D2a and D3b. Moreover, the diffusion and convection compensate for the most of the excessive heat produced by the ‘greenhouse’ effect. They transport the excessive heat up to $\sigma \sim 0.7$ with the maximum daily mean heating rate of 10-20 K Sol⁻¹, as seen in the difference between Figures D1b and D2b. The dynamical contribution is almost the same in the 15ON and 15OFF experiments (see Figures D1c and D2c).

Synthetically, the CO₂ 15μm band tends to cool the atmosphere, as seen in the difference between Figures D1d and D2d. As a result, the temperature in 15OFF experiment becomes higher than in 15ON experiment (Figure D4).

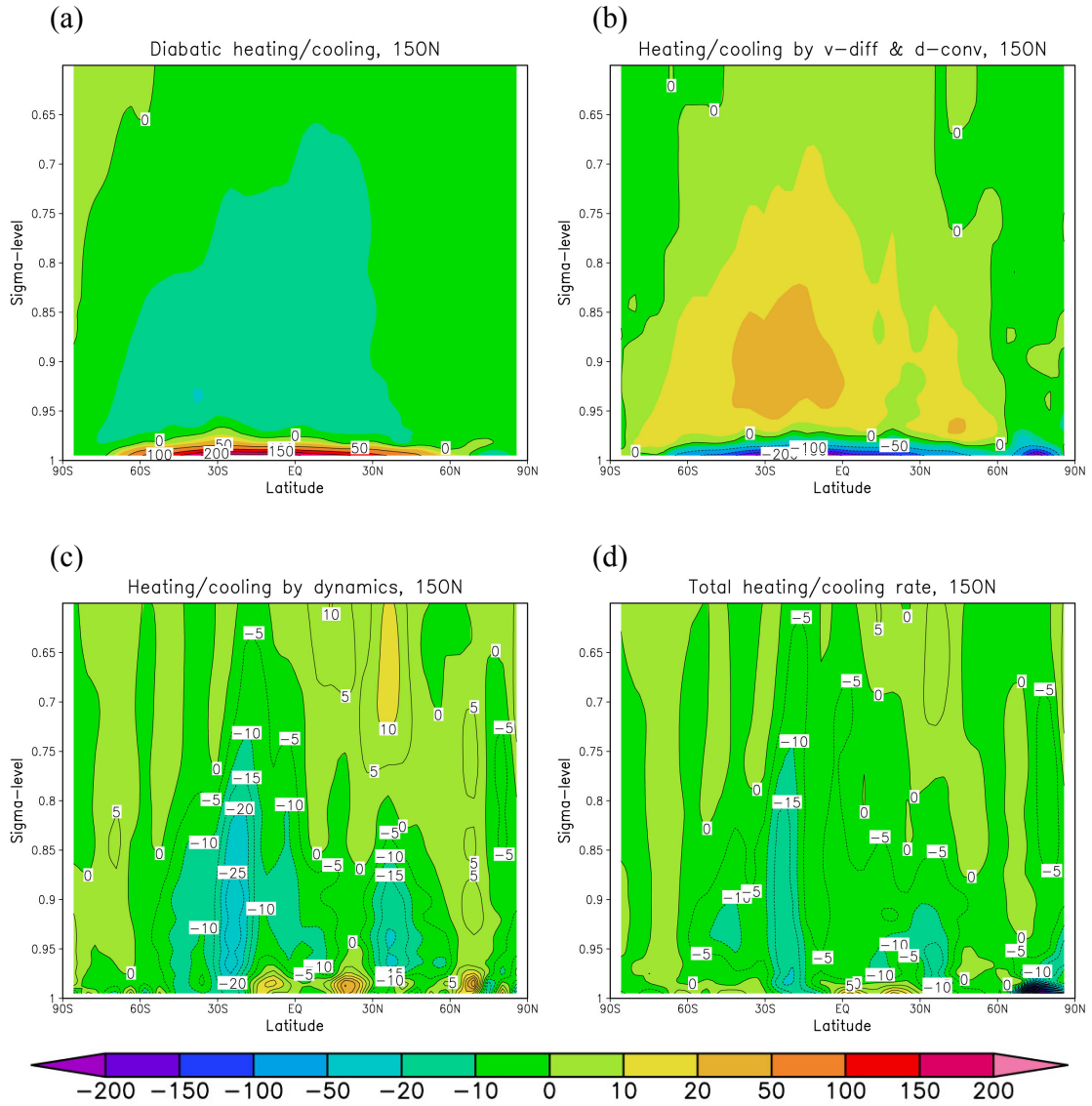


Figure D1. Zonal-mean heating/cooling rates [K Sol^{-1}] in the 15ON experiment: (a) due to the diabatic effects (sum of radiative effects by dust and CO_2 in all wavelengths), (b) due to the sum of the vertical diffusion and dry convective adjustment, (c) due to the dynamical effects (sum of the advection and adiabatic effects), and (d) the sum of (a)-(c).

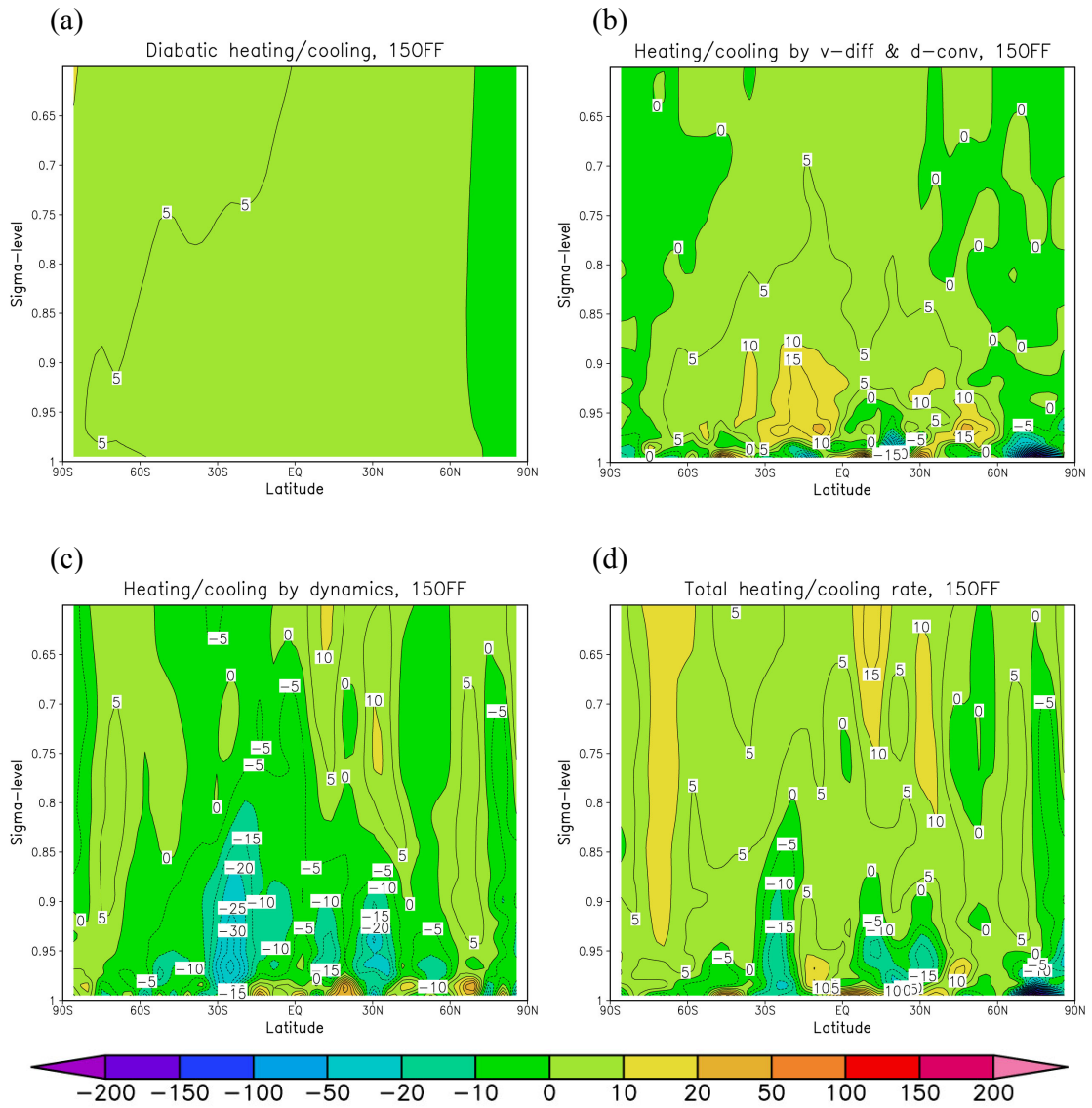


Figure D2: Same as in Figure D1, except for the 15OFF experiment.

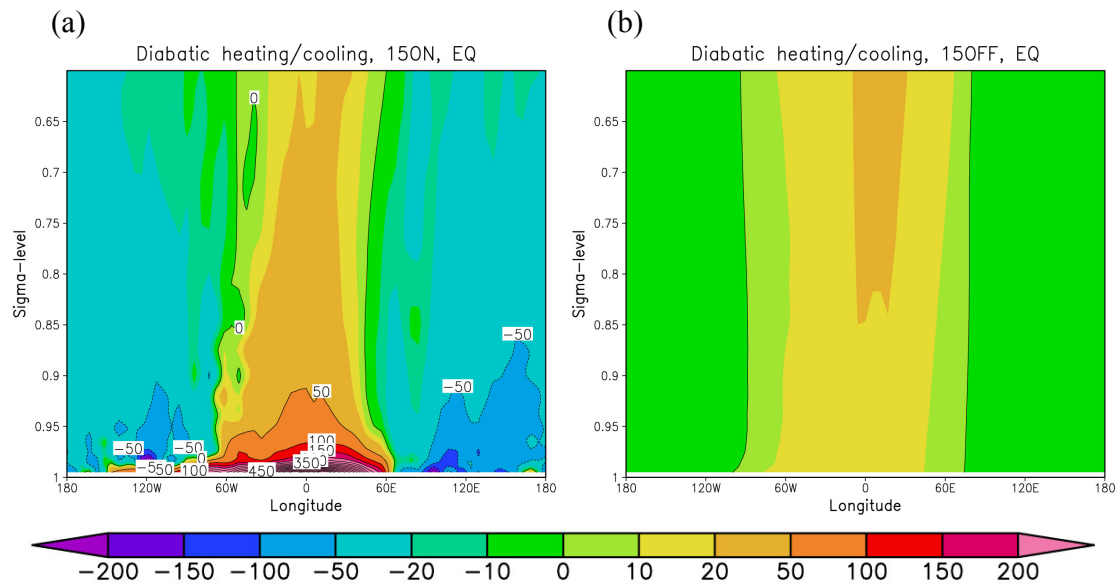


Figure D3: Snapshots of the diabatic heating/cooling rate $[K Sol^{-1}]$ at the equator, in the (a) 15ON and (b) 15OFF experiments. Note that the local time at the longitude 0° is noon.

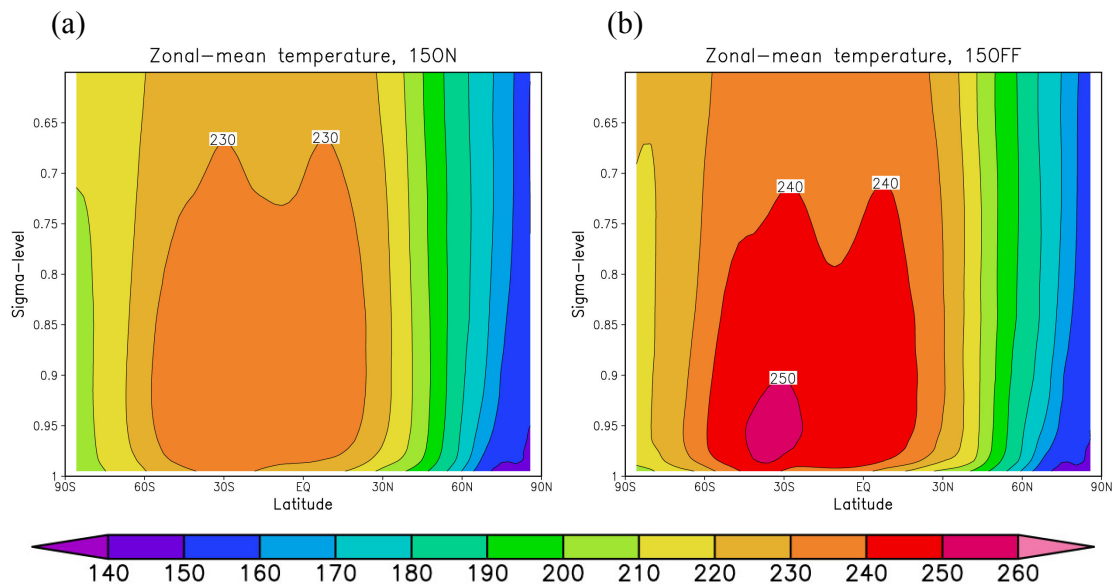


Figure D4: Zonal-mean temperature in the (a) 15ON and (b) 15OFF experiments.

Appendix E

Simulated zonal-mean circulation near the surface

In Figure 69, the values of the mass stream function near the surface become positive in both dust cases. This requires some explanations, which follows here.

As with all stream functions, the absolute value of Ψ_M has no physical significance, while their gradients do. Figure E1 shows the vertical velocity and streamlines for the lowest part of the domain that corresponds to Figure 69a. It is seen that the southward wind near the surface represents the return portion of the larger clockwise cell (between 30° S and 30° N in Figure E1). The low altitude portion of the counterclockwise cell is seen to the north of $\sim 45^\circ$ N. Figure E1 also shows that the southward flow follows the zonal-mean topography with the South-North slope. Therefore, the mean upward wind exists in this area of the return flow. These modeling results look plausible and apparently unrelated to thermal effects at the surface, as the similar flow is produced in the experiment with the CO_2 infrared radiation (see Subsection 3.1.3 and Appendix D) turned off (Figure E2). In the latter case, the surface temperature is 5-10 K lower compared to the experiment with the CO_2 infrared radiation included (Figure E3).

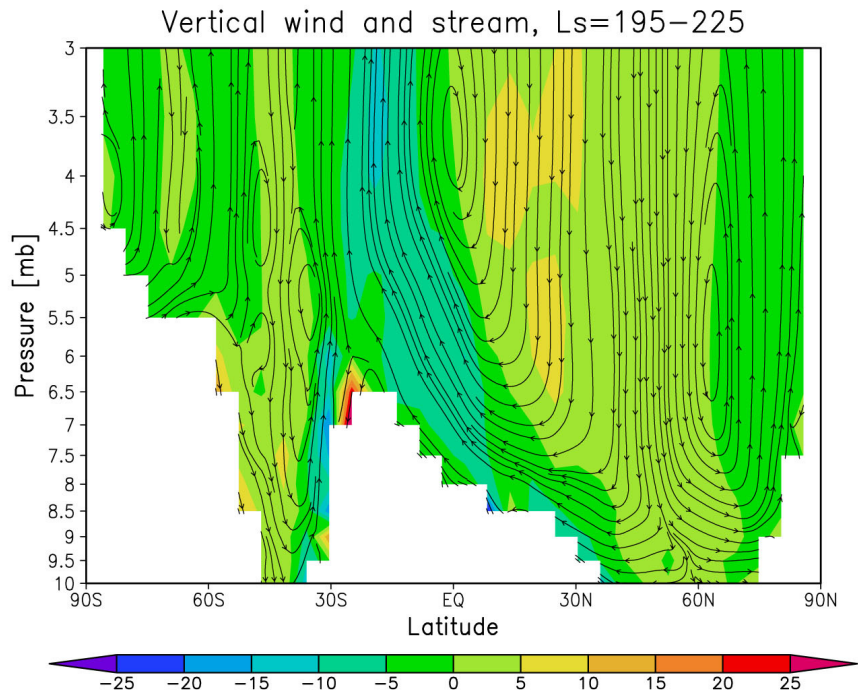


Figure E1: The zonal-mean vertical velocity [$\times 10^{-4} \text{ Pa s}^{-1}$] (shaded) and the streamlines of the zonal-mean meridional circulation below 3 mb, in ‘autumn’ ($L_s=195^\circ-225^\circ$) for the ‘weak-dust’ (TES2) scenario.

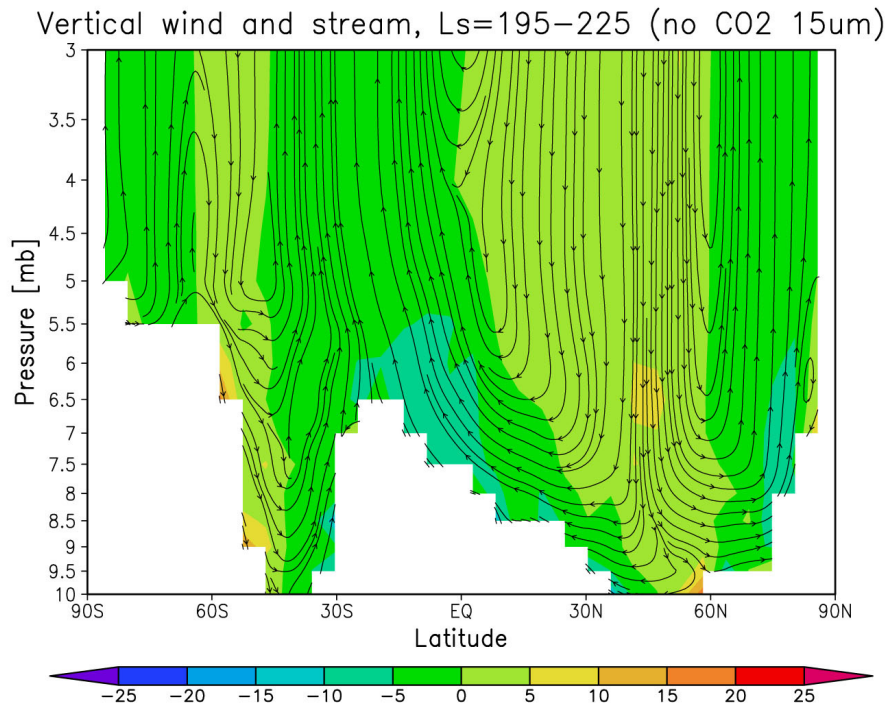


Figure E2: Same as in Figure E1, but in the experiment with the CO_2 infrared radiation turned off.

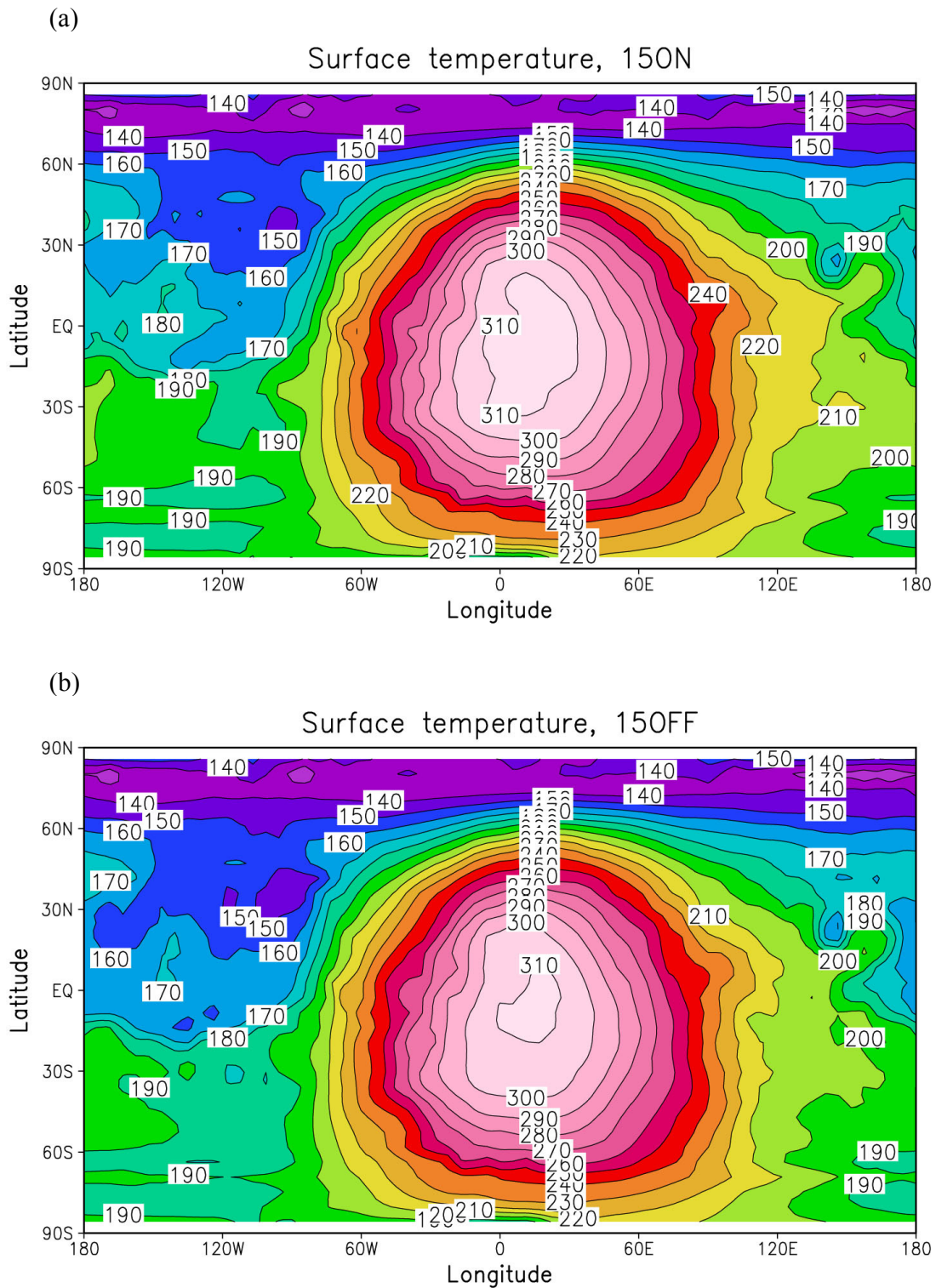


Figure E3: Snapshots of the surface temperature [K], in the (a) 15ON and (b) 15OFF experiments. See Appendix D about the 15ON and 15OFF experiments and note that the local time at the longitude 0° is noon.

References

- Anderson, E. and C. Leovy, 1978: Mariner 9 television limb observation of dust and ice hazes on Mars, *J. Atmos. Sci.* **35**, 723-734.
- Andrews, D. G., J. R. Holton and C. B. Leovy, 1987: Middle Atmosphere Dynamics, *International Geophysics Series* Vol. 40, edited by R. Dmowska and J. R. Holton, Academic Press, 489 pp.
- Banfield, D., B. J. Conrath, P. J. Gierasch, R. J. Wilson and M. D. Smith, 2004: Traveling waves in the Martian atmosphere from MGS TES nadir data, *Icarus* **170**, 365-403.
- Barnes, J. R., 1980: Time spectral analysis of midlatitude disturbances in the Martian atmosphere, *J. Atmos. Sci.* **37**, 2002-2015.
- Barnes, J. R., 1981: Midlatitude disturbances in the Martian atmosphere: A second Mars year, *J. Atmos. Sci.* **38**, 225-234.
- Barnes, J. R., 1984: Linear baroclinic instability in the Martian atmosphere, *J. Atmos. Sci.* **41**, 1536-1550.
- Barnes, J. R., J. B. Pollack, R. M. Haberle, R. W. Zurek, C. B. Leovy, H. Lee and J. Schaeffer, 1993: Mars atmospheric dynamics as simulated by the NASA/Ames general circulation model, 2, Transient baroclinic eddies. *J. Geophys. Res.* **98**, 3125-3148.
- Barnes, J. R., R. M. Haberle, J. B. Pollack, H. Lee and J. Schaeffer, 1996: Mars atmospheric dynamics as simulated by the NASA/Ames general circulation model, 2, winter quasi-stationary eddies. *J. Geophys. Res.* **101**, 12753-12776.
- Basu, S., M. I. Richardson and R. J. Wilson, 2004: Simulation of the Martian dust cycle with the GFDL Mars GCM, *J. Geophys. Res.* **109**, E11006, doi10.1029/2004JE002243.
- Bell, J. F., III, T. B. McCord and P. D. Owensby, 1990: Observational evidence of crystalline iron oxides on Mars, *J. Geophys. Res.* **95**, 14447-14461.
- Bibring, J.-P., M. Combes, Y. Langevin, A. Soufflot, C. Cara, P. Drossart, Th. Encrenaz, S.

- Erard, O. Forni, B. Gondet, L. Ksanfomality, E. Lellouch, Ph. Masson, V. Moroz, F. Rocard, J. Rosenqvist and C. Sotin, 1989: Results from the ISM experiment, *Nature* **341**,591-593.
- Böttger, H. M., S. R. Lewis, P. L. Read and F. Forget, 2004: The effect of a global dust storm on simulations of the Martian water cycle, *Geophys. Res. Lett.* **31**, L22702, doi:10.1029/2004GL021137.
- Böttger, H. M., S. R. Lewis, P. L. Read and F. Forget, 2005: The effects of the Martian regolith on GCM water cycle simulations, *Icarus* **177**, 174-189.
- Branscome, L. E., 1983: The Charney baroclinic stability problem: Approximate solutions and model structures, *J. Atmos. Sci.* **40**, 1393-1409.
- Clancy, R. T., S. W. Lee, G. R. Gladstone, W. W. McMillan and T. Rousch, 1995: A new model for Mars atmospheric dust based upon analysis of ultraviolet through infrared observations from Mariner 9, Viking, and Phobos, *J. Geophys. Res.* **100**, 5251– 5263.
- Collins, M. and I. N. James, 1995: Regular baroclinic transient waves in a simplified global circulation model of the Martian atmosphere, *J. Geophys. Res.* **100**, 14421-14432.
- Collins, M., S. R. Lewis, P.L. Read and F. Hourdin, 1996: Baroclinic wave transitions in the Martian atmosphere. *Icarus* **120**, 344-357.
- Conrath, B. J., 1975: Thermal structure of the Martian atmosphere during the dissipation of the dust storm of 1971, *Icarus* **24**, 36-46.
- Conrath, B. J., J. C. Pearl, M. D. Smith, W. C. Maguire, P. R. Christensen, S. Dason and M. S. Kaelberer, 2000: Mars Global Surveyor Thermal Emission Spectrometer (TES) observations: Atmospheric temperatures during aerobraking and science phasing, *J. Geophys. Res.* **105**, 9509-9519.
- Drossart, P., J. Rosenqvist, S. Erard, Y. Langevin, J. P. Bibring and M. Combes, 1991: Martian aerosol properties from the Phobos/ISM experiment, *Ann. Geophys.* **9**, 754-760.
- Forget, F., G. B. Hansen and J. B. Pollack, 1995: Low brightness temperatures of Martian polar caps: CO₂ cloud or low surface emissivity?, *J. Geophys. Res.* **100**, 21219-21234.

- Forget, F., 1998: Improved optical properties of the Martian atmospheric dust for radiative transfer calculations in the infrared, *Geophys. Res. Lett.* **25**, 1105-1108.
- Forget, F., F. Hourdin and O. Talagrand, 1998: CO₂ Snowfall on Mars: Simulation with a General Circulation Model, *Icarus* **131**, 302-316.
- Forget, F., F. Hourdin, R. Fournier, C. Hourdin and O. Talagrand, 1999: Improved general circulation models of the Martian atmosphere from the surface to above 80 km, *J. Geophys. Res.* **104**, 24155-24175.
- Forget, F., Y. Wanherdrick and S.R. Lewis, 2001: Validation of the Mars General Circulation Model and Climate Database with new spacecraft observations, European Space Agency Technical Report, 22 pp.
- Forget, F., M. Angelates I Coll, Y. Wanherdrick, F. Hourden, S. Lewis, P. Read, F. Taylor, M. Lopez-Valverde and M. Lopez-Puertas, 2003: Modeling of the general circulation with the LMD-AOPP-IAA GCM: Update on model design and comparison with observations, Abstract of “*Mars atmosphere modeling and observations*”, Granada, Spain, 6 pp.
- Gierasch, P. J. and R. M. Goody, 1972: The effect of dust on the temperature of the Martian atmosphere, *J. Atmos. Sci.* **29**, 400-401.
- Goody, R. M. and Y. L. Yung, 1989: Atmospheric Radiation Theoretical Basis, Second Edition, Oxford University Press, 519 pp.
- Greeley, R., and J. D. Iversen, 1985: Wind as a Geological Process on Earth, Mars, Venus and Titan, Cambridge Univ. Press, 333 pp.
- Gurwell, M. A., E. A. Bergin, G. J. Melnick and V. Tolls, 2005: Mars surface and atmospheric temperature during the 2001 global dust storm, *Icarus* **175**, 23-31.
- Haberle, R. M., J. B. Pollack, J. R. Barnes, R. W. Zurek, C. B. Leovy, J. R. Murphy, H. Lee and J. Schaeffer, 1993: Mars atmospheric dynamics as simulated by the NASA/Ames general circulation model, 1, The zonal-mean circulation, *J. Geophys. Res.* **98**, 3093-3124.
- Haberle, R. M., M. M. Joshi, J. R. Murphy, J. R. Barnes, J. T. Schofield, G. Wilson, M. Lopez-Valverde, J. L. Hollingsworth, A. F. C. Bridge and J. Schaeffer, 1999: General circulation model simulations of the Mars Pathfinder atmospheric structure investigation/meteorology data, *J. Geophys. Res.* **104**, 8957-8974.

- Haberle, R. M., J. R. Murphy and J. Schaeffer, 2003: Orbital change experiments with a Mars general circulation model, *Icarus* **161**, 66-89.
- Hansen, J. E., 1969: Exact and approximate solutions for multiple scattering by cloudy and hazy planetary atmospheres, *J. Atmos. Sci.* **26**, 478-487.
- Hapke, B., 1981: Bidirectional reflectance spectroscopy, 1, Theory, *J. Geophys. Res.* **86**, 3039-3054.
- Hapke, B., 1986: Bidirectional reflectance spectroscopy, 4, The extinction coefficient and the opposition effect, *Icarus* **67**, 264-280.
- Hartogh, P., A. S. Medvedev, T. Kuroda, R. Saito, G. Villanueva, A. G. Feofilov, A. A. Kutepov and U. Berger, 2005: Description and climatology of a new general circulation model of the Martian atmosphere, *J. Geophys. Res.* **110**, E11008, doi:10.1029/2005JE002498.
- Hourdin, F., P. Le Van, F. Forget and O. Talagrand, 1993: Meteorological variability and the annual surface pressure cycle on Mars, *J. Atmos. Sci.* **50**, 3625-3640.
- Hourdin, F., F. Forget and O. Talagrand, 1995: The sensitivity of the Martian surface pressure to various parameters: A comparison between numerical simulations and Viking observations, *J. Geophys. Res.* **100**, 5501-5523.
- James, P. B., H. H. Kieffer and D. A. Paige, 1992: The seasonal cycle of carbon dioxide on Mars, in *Mars*, edited by H. H. Kieffer et al., Univ. of Ariz. Press, 934-968 pp.
- Jaquin F., P. Gierasch and R. Kahn, 1986: The vertical structure of limb hazes in the Martian atmosphere, *Icarus* **68**, 442-461.
- Joseph, J. H., W. J. Wiscombe and J. A. Weinman, 1976: The delta-Eddington approximation for radiative flux transfer, *J. Atmos. Sci.* **33**, 2452-2459.
- Joshi, M. M., S. R. Lewis, P. L. Read and D. C. Catling, 1994: Western boundary currents in the atmosphere of Mars, *Nature* **367**, 548-551.
- Kahre, M. A., J. R. Murphy, R. M. Haberle, F. Montmessin and J. Schaeffer, 2005: Simulating the Martian dust cycle with a finite surface dust reservoir, *Geophys. Res. Lett.* **32**, L20204, doi:10.1029/2005GL023495.
- Korablev, O. I., V. A. Kranopolsky, A. V. Rodin and E. Chassefiere, 1993: Vertical structure of Martian dust measured by solar infrared occultations from the Phobos spacecraft, *Icarus* **102**, 76-87.

- Kuroda, T., N. Hashimoto, D. Sakai and M. Takahashi, 2005: Simulation of the Martian atmosphere using a CCSR/NIES AGCM, *J. Meteorol. Soc. Japan* **83**, 1-19.
- Lee, S. W., 1995: "Viking Lander meteorology and atmospheric opacity data set", NASA Planetary Data System, http://atmos.nmsu.edu/PDS/data/vl_1001/.
- Leovy, C. B., 1969: Mars: Theoretical aspects of meteorology, *Appl. Opt.* **8**, 1279-1286.
- Leovy, C. B. and Y. Mintz, 1969: Numerical simulation of the atmospheric circulation and climate of Mars, *J. Atmos. Sci.* **26**, 1167-1190.
- Leovy, C. B., G. A. Briggs, A. T. Young, B. A. Smith, J. B. Pollack, E. N. Shipley and R. L. Wildey, 1972: The Martian atmosphere: Mariner 9 television experiment progress report, *Icarus* **17**, 373-393.
- Leovy, C. B., 1979: Martian meteorology, *Ann. Rev. Astron. Astrophys.* **17**, 387-413.
- Lewis S. R., M. Collins, P. L. Read, F. Forget, F. Hourdin, R. Fournier, C Hourdin, O. Talagrand and J.-P. Huot, 1999: A climate database for Mars. *J. Geophys. Res.* **104**, 24177-24194.
- Lewis S. R., M. Collins and F. Forget, 2001: Mars Climate Database v3.0 Detailed Design Document, European Space Agency Technical Report, 29 pp.
- Liou, K. N., 2002: An Introduction to Atmospheric Radiation: Second Edition, Academic Press, 577 pp.
- Liu, J., M. I. Richardson and R. J. Wilson, 2003: An assessment of the global, seasonal, and interannual spacecraft record of Martian climate in the Thermal infrared. *J. Geophys. Res.* **108**(E8), doi:10.1029/2002JE001921.
- Lopez-Puertas M. and M. A. Lopez-Valverde, 1995: Radiative energy balance of CO₂ non-LTE infrared emissions in the Martian atmosphere, *Icarus* **114**, 113-129.
- Lopez-Valverde M. A., D. P. Edwards, M. Lopez-Puertas and C. Roldan 1998: Non-local thermodynamic equilibrium in general circulation models of the Martian atmosphere 1. Effects of the local thermodynamic equilibrium approximation on thermal cooling and solar heating, *J. Geophys. Res.* **103**, 16799-16811.
- Markiewicz, W. J., R. M. Sablotny, H. U. Keller, N. Thomas, D. Titov and P. H. Smith, 1999: Optical properties of the Martian aerosols as derived from Imager for Mars Pathfinder midday sky brightness data, *J. Geophys. Res.* **104**, 9009-9017.
- Martin, T. Z. and H. H. Kieffer, 1979: Thermal infrared properties of the Martian

- atmosphere, 2, The 15-mm band measurements, *J. Geophys. Res.* **84**, 2843-2852.
- Martin, T. Z., 1986: Thermal infrared opacity of the Mars atmosphere. *Icarus* **66**, 2-21.
- Martin, T. Z. and M. I. Richardson, 1993: New dust opacity mapping from Viking infrared thermal mapping data, *J. Geophys. Res.* **98**, 10941-10949.
- Meador, W. E. and W. R. Weaver, 1980: Two-stream approximations to radiative transfer in planetary atmospheres: A unified description of existing methods and a new improvement, *J. Atmos. Sci.* **37**, 630-643.
- Mellon, M. T., 2001: Thermal inertia and rock abundance, Abstract of “*Exploring Mars with TES: A Data User's Workshop*”, Tempe, Arizona, 6 pp.
- Mischna, M. A., M. I. Richardson, R. J. Wilson and D. J. McCleese, 2003: On the orbital forcing of Martian water and CO₂ cycles: A general circulation model study with simplified volatile schemes, *J. Geophys. Res.* **108**(E6), doi:10.1029/2003JE002051.
- Montmessin, F., F. Forget, P. Rannou, M. Cabane and R. M. Haberle, 2004: Origin and role of water ice clouds in the Martian water cycle as inferred from a general circulation model, *J. Geophys. Res.* **109**, E10004, doi:10.1029/2004JE002284.
- Moriyama, S., 1974: Effects of dust on radiation transfer in the martian atmosphere (I) — On infrared radiative cooling—, *J. Meteor. Soc. Japan* **52**, 457-462.
- Moriyama, S., 1975: Effects of dust on radiation transfer in the martian atmosphere (II) —Heating due to absorption of the visible solar radiation and importance of radiative effects of dust on the Martian meteorological phenomena—, *J. Meteor. Soc. Japan* **53**, 214-221.
- Moriyama, S. and T. Iwashima, 1980: A spectral model of the atmospheric general circulation of Mars: A numerical experiment including the effects of the suspended dust and the topography, *J. Geophys. Res.* **85**, 2847-2860.
- Moudden, Y., and J. C. McConnell, 2005: A new model for multiscale modeling of the Martian atmosphere, GM3, *J. Geophys. Res.* **110**, E04001, doi:10.1029/2004JE002354.
- Mustard, J. F., S. Erard, J.-P. Bibring, J. W. Head, S. Hurez, Y. Langevin, C. M. Pieters and C. J. Sotin, 1993: The surface of Syrtis Major: Composition of the volcanic substrate and mixing with altered dust and soil, *J. Geophys. Res.* **98**, 3387-3400.

- Mustard, J. F. and J. F. Bell III, 1994: New composite reflectance spectra of Mars from 0.4 to 3.14 μm , *Geophys. Res. Lett.* **21**, 353-356.
- Nakajima, T. and M. Tanaka, 1986: Matrix formulations for the transfer of solar radiation in a plane-parallel scattering atmosphere. *J. Quant. Spectrosc. Radiat. Transfer* **35**, 13-21.
- Nakajima, T., M. Tsukamoto, Y. Tsushima, A. Numaguti and T. Kimura, 2000: Modeling of the radiative process in an atmospheric general circulation model, *Applied Optics* **39**, 4869-4878.
- Newman, C. E., S. R. Lewis, P. I. Read and F. Forget, 2002a: Modeling the Martian dust cycle 1. Representations of dust transport processes, *J. Geophys. Res.* **107**(E12), doi:10.1029/2002JE001910.
- Newman, C. E., S. R. Lewis, P. I. Read and F. Forget, 2002b: Modeling the Martian dust cycle 2. Multiannual radiatively active dust transport simulations, *J. Geophys. Res.* **107**(E12), doi:10.1029/2002JE001920.
- Newman, C. E., S. R. Lewis and P. L. Read, 2005: The atmospheric circulation and dust activity in different orbital epochs on Mars, *Icarus* **174**, 135-160.
- Numaguti, A., S. Sugata, M. Takahashi, T. Nakajima and A. Sumi, 1997: Study on the Climate System and Mass Transport by a Climate Model, CGER's supercomputer monograph report vol.3, Center for Global Environmental Research/National Institute for Environmental Studies in Environment Agency of Japan, 91 pp.
- Ockert-Bell, M. E., J. F. Bell III, J. B. Pollack, C. P. McKay and F. Forget, 1997: Absorption and scattering properties of the Martian dust in the solar wavelengths, *J. Geophys. Res.* **102**, 9039-9050.
- Owen, T. and C. Sagan, 1972: Minor constituents in planetary atmospheres: Ultraviolet spectroscopy from the Orbiting Astronomical Observatory, *Icarus* **16**, 557-568.
- Pollack, J. B., R. Kahn, J. Hunter, W. Van Camp, C. E. Carlson and D. C. Pidek, 1977: Properties of aerosols in the Martian atmosphere, as inferred from Viking Lander imaging data, *J. Geophys. Res.* **82**, 4479-4496.
- Pollack, J. B., D. S. Colburn, F. S. Flasar, R. Kahn, C. E. Carlson and D. C. Pidek, 1979: Properties and effects of dust suspended in the Martian atmosphere, *J. Geophys. Res.* **84**, 2929-2945.

- Pollack, J. B., C. B. Leovy, P. W. Greiman and Y. Mintz, 1981: A Martian general circulation experiment with large topography, *J. Atmos. Sci.* **38**, 3-29.
- Pollack, J. B., R. M. Haberle, J. Schaeffer and H. Lee, 1990: Simulations of the general circulation of the Martian atmosphere, 1, Polar processes, *J. Geophys. Res.* **95**, 1447-1473.
- Pollack, J. B., R. M. Haberle, J. R. Murphy, J. Schaeffer and H. Lee, 1993: Simulation of the general circulation of the Martian atmosphere 2, Seasonal pressure variations, *J. Geophys. Res.* **98**, 3149-3181.
- Pollack, J. B., M. E. Oelkert-Bell and M. K. Shepard, 1995: Viking Lander image analysis of Martian atmospheric dust, *J. Geophys. Res.* **100**, 5235-5250.
- Richardson, M. I. and R. J. Wilson, 2002: Investigation of the nature and stability of the Martian seasonal water cycle with a general circulation model, *J. Geophys. Res.* **107**(E5), doi:10.1029/2001JE001536.
- Richardson, M. I., R. J. Wilson and A. V. Rodin, 2002: Water ice clouds in the Martian atmosphere: General circulation model experiments with a simple cloud scheme, *J. Geophys. Res.* **107**(E9), doi:10.1029/2001JE001804.
- Roush, T., J. Pollack and J. Orenberg, 1991: Derivation of midinfrared (5-25 μm) optical constants of some silicates and palagonite, *Icarus* **94**, 191-208.
- Roush, T. L., E. A. Roush, R. B. Singer and P. G. Lucey, 1992: Estimates of absolute flux and radiance factor of localized regions on Mars in the 2-4 μm wavelength region, *Icarus* **99**, 42-50.
- Schofield, J. T., J. R. Barnes, D. Crisp, R. M. Haberle, S. Larsen, J. A. Magalhães, J. R. Murphy, A. Seiff, G. Wilson, 1997: The Mars Pathfinder Atmospheric Structure Investigation/Meteorology (ASI/MET) Experiment, *Science* **278**, 1752-1758.
- Sekiguchi, M., 2004: A study on evaluation of the radiative flux and its computational optimization in the gaseous absorbing atmosphere. Science Doctoral Dissertation, University of Tokyo, Japan, 121 pp (in Japanese).
- Shibata, K., 1999: Meteorology of the light, *Series of the applied meteorology* 1, edited by R. Kimura, Asakura Shoten Co., 182 pp (in Japanese).
- Smith, D. E., M. T. Zuber, S. C. Solomon, R. J. Phillips, J. W. Head, J. B. Garvin, W. B.

- Banerdt, D. O. Muhleman, G. H. Pettengill, G. A. Neumann, F. G. Lemoide, J. B. Abshire, O. Aharonson, C. D. Brown, S. A. Hauck, A. B. Ivanov, P. J. McGovern, H. J. Zwally and T. C. Duxbury, 1999: The global topography of Mars and implications for surface evolution. *Science* **284**, 1495-1503.
- Smith, M. D., J. C. Pearl, B. J. Conrath, and P. R. Christensen, 2001: Thermal Emission Spectrometer results: Mars atmospheric thermal structure and aerosol distribution, *J. Geophys. Res.* **106**, 23929-23945.
- Smith, M. D., B. J. Conrath, J. C. Pearl and P. R. Christensen, 2002: NOTE Thermal Emission Spectrometer observations of Martian planet-encircling dust storm 2001A, *Icarus* **157**, 259-263.
- Smith, M. D., 2004: Interannual variability in TES atmospheric observations of Mars during 1999-2003, *Icarus* **167**, 148-165.
- Takahashi, Y. O., H. Fujiwara, H. Fukunishi, M. Odaka, Y.-Y. Hayashi and S. Watanabe, 2003: Topographically induced north-south asymmetry of the meridional circulation in the Martian atmosphere. *J. Geophys. Res.* **108**(E3), doi:10.1029/2001JE001638.
- Takahashi, Y. O., H. Fujiwara and H. Fukunishi, 2006: Vertical and latitudinal structure of the migrating diurnal tide in the Martian atmosphere: Numerical investigations, *J. Geophys. Res.* **111**, E01003, doi:10.1029/2005JE002543.
- Tanaka, H. L. and M. Arai, 1999: Linear baroclinic instability in the Martian atmosphere: Primitive equation calculations, *Earth Planets Space* **51**, 225-232.
- Tomasko, M. G., L. R. Doose, M. Lemmon, P. H. Smith and E. Wegryn, 1999: Properties of dust in the Martian atmosphere from the imager on Mars Pathfinder, *J. Geophys. Res.* **104**, 8987-9007.
- Toon, O. B., J. B. Pollack and C. Sagan, 1977: Physical properties of the particles composing the Martian dust storm of 1971-1972, *Icarus* **30**, 663-696.
- Toon, O. B., C. P. McKay, T. P. Ackerman and K. Santhanam, 1989: Rapid calculation of radiative heating rates and photodissociation rates in inhomogeneous multiple scattering atmospheres, *J. Geophys. Res.* **94**, 16287-16301.
- van de Hulst, H. C., 1957: Light scattering by small particles, John Wiley & Sons, Inc., 470 pp.

- van de Hulst, H. C., 1968: Asymptotic fitting, a method for solving anisotropic transfer problems in thick layers, *J. Comput. Phys.* **3**, 291-306.
- Wallace, L., J. J. Caldwell and B. D. Savage, 1972: Ultraviolet photometry from the Orbiting Astronomical Observatory, III, Observations of Venus, Mars, Jupiter and Saturn longward of 2000 Å, *Astrophys. J.* **172**, 755-769.
- Willebrand, J., 1978: Temporal and spatial scales of the wind field over the North Pacific and North Atlantic, *J. Phys. Oceanogr.* **8**, 1080-1094.
- Wilson, R. J., and K. Hamilton, 1996: Comprehensive model simulation of thermal tides in the Martian atmosphere, *J. Atmos. Sci.* **53**, 1290-1326.
- Wilson, J. R., 1997: A general circulation model simulation of the Martian polar warming, *Geophys. Res. Lett.* **24**, 123-126.
- Wilson, R. J. and M. I. Richardson, 2000: The Martian atmosphere during the Viking Mission, I: Infrared measurements of atmospheric temperatures revisited, *Icarus* **145**, 555-579.
- Wilson, R. J., D. Banfield, B. J. Conrath and M. D. Smith, 2002: Traveling waves in the northern hemisphere of Mars, *Geophys. Res. Lett.* **29**, doi:10.1029/2002GL014866.
- Wolff, M. J. and R. T. Clancy, 2003: Constraints on the size of Martian aerosols from Thermal Emission Spectrometer observations, *J. Geophys. Res.* **108**(E9), doi:10.1029/2003JE002057.
- Zurek, R. W., 1978: Solar heating of the Martian dusty atmosphere, *Icarus* **35**, 196-208.

Acknowledgements

This study was done under the supervision of Prof. Masaaki Takahashi (CCSR) since October 1998. He gave me many good suggestions for my study, and patiently taught me many things about the attitude of a professional scientist. I am very much grateful to him.

Prof. Teruyuki Nakajima (CCSR), the chief examiner for my thesis, gave me kind advices about the radiative transfer scheme. Professors Yoshihisa Matsuda (Tokyo Gakugei University), Yutaka Abe (University of Tokyo) and Takeshi Imamura (Institute of Space and Astronautical Science / Japan Aerospace Exploration Agency, ISAS/JAXA), the second readers, also gave me many instructive advices for my thesis.

Drs. Masayuki Takigawa (Frontier Research Center for Global Change), Tatsuya Nagashima (NIES) and Kengo Sudo (Nagoya University) instructed me on the basic skills for developing and using the CCSR/NIES AGCM. Messrs. Naohisa Hashimoto (NEC Corporation) and Daisuke Sakai (Daiichi Jitsugyo Co., ltd) participated in the development of our Martian GCM, and had many discussions with me about the modeling. They became the co-authors of my first paper. I am grateful to all students, postdocs, and secretaries at Takahashi Lab. for many advices in the group seminars, administrations of the computers, and so on.

Dr. Toshihiko Takemura (Kyushu University) taught me details of the aerosol radiation scheme in the CCSR/NIES AGCM. Dr. Miho Sekiguchi (Tokyo University of Marine Science and Technology) gave me the information about MSTRN-X. Drs. Masatsugu Odaka and Yoshiyuki Takahashi (Hokkaido University) gave me several comments and advices about the Martian atmosphere and its modeling. Dr. Michael D. Smith (NASA) provided me with the TES climatology tables. Dr. Michael J. Wolff (Space Science Institute) provided me with the data set of refractive indices profiles for the Martian dust. The GCM simulations were performed using mainly SX-6 of the NEC Corporation in NIES.

I was very lucky that I had a chance to study at Max-Planck-Institute for Solar System Research (MPS) in Katlenburg-Lindau, Germany, from April 2004 up to now. I am very grateful to Dr. Paul Hartogh for accepting me at the MAOAM project, in addition to Prof. Masato Nakamura (ISAS/JAXA) and Dr. Ai Inada (California Institute of Technology)

who helped me to establish relations with MPS. In MPS, Dr. Alexander S. Medvedev gave me many useful suggestions, and had many discussions with me that proved to be helpful for my research. Drs. Geronimo Villanueva (NASA) and Ryu Saito (NIES) also discussed the Martian modeling with me. I am grateful to all colleagues and secretaries in MPS, and the International Max Planck Research School, for aiding me in Lindau.

Finally, I am grateful to my parents and sister who strongly supported and encouraged me during all this time.